A Process for the Design and Manufacture of Propellers for Small Unmanned Aerial Vehicles

by

Brian David Rutkay

A thesis submitted to the Faculty of Graduate and Postdoctoral Affairs in partial fulfillment of the requirements for the degree of

Master of Applied Science

in

Aerospace Engineering

Carleton University
Ottawa, Ontario

Abstract

The objective of this research was to develop a process for the design and manufacture of mission- and aircraft-specific propellers for small unmanned aerial vehicles. This objective was met by creating a computer program to design a propeller that meets user-defined aircraft performance requirements within the limitations of the motor, material, and manufacturing methods. The use of additive manufacturing (3D printing) in making flightworthy propellers was explored through material testing and by manufacturing trials. By testing the propellers in simulated flight conditions, it was found that the propellers generated nearly the expected design thrust, but a series of manufacturing and instrumentation issues prevented a complete evaluation of their performance. Testing was sufficient to demonstrate the feasibility of flightworthy propellers produced through additive manufacturing. Future work for the further development of the design program was also outlined.

Acknowledgements

This work was completed over the course of three years but probably would have taken twice as long had it not been for the help of many individuals. I'd like to thank the department of Mechanical and Aerospace Engineering lab staff – Steve Truttmann, Stephan Bilijan and David Raude – for their assistance during material and wind tunnel testing. I'd also like to thank Nagui Mikhail for his advice and for allowing me access to the Department of Electronics' resources throughout the development of the instrumentation. Throughout my undergrad and graduate studies I've been grateful for Alex Proctor, Kevin Sangster and Ian Lloy for allowing me to work in the department machine shop and patiently helping me produce what I've designed. My experiences in the machine shop influenced everything I designed for my thesis and am grateful for the opportunities I had to learn from you.

I'd like to thank all of my friends for their support throughout the course of this project. There are a few people I'd like to recognize in particular for their help on key aspects of this work. Hristo Valtchanov's advice on layout of my thesis led to a drastically better final product than I could have hoped for had I done it my way. I'd like to thank John Polansky for his advice and support but in particular helping me polish my defense presentation and selecting the appropriate firearms and ammunition for the ballistic pendulum test. I'm grateful for Ryan Anderson for showing me some of the sheet metal fabrication practices he learned while working in the aviation industry and for the great discussions on aircraft and mechanical design we had, especially back in undergrad when I was starting to develop my mechanical design skills. I'd like to thank Jonathan Wiebe for his help on manufacturing the test rig - luckily for me even after he'd

spent a full day work on his own research work he was willing to help me assemble and troubleshoot problems with the test rig - and for his advice while I was writing the design program. I also need to thank Aaron Parton for the numerous shawarma-and-beer discussions during development and for "Jarome" which was used during the ballistic pendulum tests.

I definitely need to thank my mom, dad and brother for putting up with me while I was working on my thesis, for the late-night rides home, and for helping me edit and format my thesis. I owe a huge amount of thanks to my dad for spending long days with me in the wind tunnel rather than the golf course over his summer vacation. As rough as testing went, I really enjoyed the opportunity to work with you in the lab and I think it's safe to say it'd have been even more hellish – and possibly never completed - had it not been for your help.

Most of all, I'm incredibly grateful for the unwavering and seemingly limitless patience, encouragement and support of my supervisor, Dr. Jeremy Laliberté. This project took much longer than planned and grew significantly in scope, and few would have been able to maintain your high level of enthusiasm throughout the course of the project despite all of the difficulties I encountered. Between getting me into the master's program to spending late nights looking over my thesis, thank you so very much for the amazing opportunities and help you've provided over the last few years.

Table of Contents

List of Tables

List of Illustrations

List of Appendices

Nomenclature

A	area
AR	aspect ratio
a	lift curve slope
B	number of blades
B	mechanical friction (within a motor)
b	chord of propeller-blade element
b	wing span
c_d	section drag coefficient
C_D	drag coefficient
c_l	section lift coefficient
C_L	lift coefficient
C_P	power coefficient
C_s	power-speed coefficient
C_T	thrust coefficient
CF	centrifugal force
c/R	non-dimensional chord length (chord divided by radius)
D	diameter
D	drag
E	elastic modulus
e	Oswald's efficiency
G	shear modulus
h	height

I	current
I	second moment of inertia
J	advance ratio
K(x)	circulation function
L	lift
M	Mach number
M	bending moment
m	mass
N	rotational speed [RPM]
n	rotational speed [rev/s]
P	pressure
P	power
Q	torque
Q	volume
R	radius
r	radius to blade station/element
S	planform area
T	thrust
t	thickness
t/c	thickness to chord ratio
V	velocity
V	voltage
w	induced velocity

$\bar{w}$	non-dimensional induced velocity
W	resultant velocity
x	non-dimensional radial location (r/R)
y	distance from neutral axis
α	angle of attack
β	blade angle
Δ	increment or width
ω	rotational speed [rad/s]
ρ	density
η	efficiency
φ	angle of resultant velocity
σ	solidity of the blade
γ	resultant angle of the drag and lift forces
λ	ratio of forward to tip speed
ζ	arbitrary constant used for the calculus of variations method
ϕ	pitch angle of the wake
ϕ_o	pitch angle of the wake excluding induced velocity
σ	stress
δ	element width
3DP	3D printed/3D printing
ADC	analog to digital converter
CAD	computer aided design
CAM	computer aided manufacturing

IAS	indicated airspeed
NM	nautical miles
RC	radio controlled
SUAV	small unmanned aerial vehicle
UAV	unmanned aerial vehicle

1 Chapter: Introduction

1.1 Motivation

Nearly every aspect of a propeller-driven aircraft's performance - such as its take-off distance, maximum payload, and endurance - is directly influenced by the efficiency and performance of its propeller. Currently most small unmanned aerial vehicles (UAVs) use inexpensive and readily-available off-the-shelf fixed-pitch propellers originally designed for radio controlled (RC) hobby aircraft. Selecting the best off-the-shelf propeller for a UAV or particular mission can become a time-consuming and expensive trial-and-error process due to the complexities of maximizing the efficiency of an electric propulsion system and meeting the performance requirements of the aircraft. This approach may still result in the use of a propeller that does not allow for the UAV to safely or efficiently perform the desired mission, denying the operator the full capabilities of the aircraft.

1.2 Objectives

Designing a propeller specific to the UAV's propulsion system and the aircraft's performance requirements will best overcome this problem. The objective of this work is to create a process for the design and manufacture of propellers for small UAVs to best meet mission and performance requirements.

1.3 Methods

Key to the fulfilling the objective of this work was an integrated software tool developed to design a fixed-pitch propeller customized to a particular UAV and set of mission requirements. This tool includes modules to analyze the aerodynamic, structural, and manufacturing aspects of the propeller based on established methods for designing

propellers for certified manned aircraft. To create a propeller, the user provides the design program with the details of the aircraft's desired mission and specifies the relative importance of efficient propeller performance in each mission segment. From this, the program first determines the best combination of propeller diameter, number of blades and blade pitch for the mission, and then designs the blades for efficient performance in the key mission segments while considering structural strength and manufacturing limitations. Once a propeller that will allow the user-defined mission to be safely flown has been created, the program produces a report detailing the propeller's operating characteristics and geometry files ready to be imported into a Computer Aided Design (CAD) program for manufacturing.

One new manufacturing technology well-suited to creating small propellers is digital additive manufacturing or 3D printing (3DP). A material testing program was undertaken to investigate the suitability of 3DP for manufacturing flightworthy propellers. This test program subjected two candidate materials to tensile and stress rupture testing for confirmation of their as-manufactured properties and to verify their ability to withstand stresses higher than would be seen in service.

The feasibility of this process was proven by making sample propellers and subjecting them to tests similar to those required for certifying propellers for manned aircraft. Testing required the design, development and manufacturing of a purpose-built test rig consisting of an instrumented test stand to measure propeller thrust and torque and a protective shroud to contain a burst propeller. The material for the panels of the shroud was selected through both drop tower and ballistic pendulum testing. The performance of

the propeller in simulated flight conditions was measured through the use of a low-speed 4’ x 6’ wind tunnel.

1.4 Scope

This work considers only the design of fixed-pitch propellers for electrically-powered fixed-wing unmanned aerial vehicles with a maximum take-off weight no greater than 35kg. While performance analysis methods for the aircraft and brushless direct-current electric motors are provided and are adequate for the purposes of the research work presented they do not take the place of more advanced methods. Due to the typical missions intended to be flown by small UAVs it is assumed that the aircraft operates in a near-constant altitude and at low subsonic speeds. A thorough consideration of compressible flow effects was neglected as it is assumed that the propeller will never be operated in conditions where it is warranted. It is also assumed that the propeller will be installed such that blockage effects are insignificant and an assessment of the flow around the propellers is not considered.

2 Chapter: Literature Review

2.1 Overview

The purpose of this section is to review the work completed in topics related to the design of propellers for small UAVs and identify the methods that will be used in this work.

2.2 Small Unmanned Aerial Vehicles

Small UAVs (SUAV) are defined by Transport Canada as uninhabited aircraft with a take-off weight less than 25 kg [1]. Small UAVs typically have a wingspan less than 4 m [2] and are powered by either an internal-combustion engine or electric motor driving a fixed pitch propeller.

SUAVs are intended for airborne data collection. Potential civil UAV missions were identified in [3] and some of these missions are well-suited to SUAVs, which include:

- forestry and mineral surveys
- agriculture monitoring and crop spraying
- transportation and energy infrastructure monitoring
- poaching and game surveys

Small UAVs offer a major advantage over manned aircraft as they can potentially perform this type of mission much more efficiently. With the exception of purpose-built reconnaissance aircraft such as the Lockheed Martin U-2 and SR-71, most aircraft used for aerial data collection are modified general aviation aircraft. Examples include the

Cessna 208 or Diamond DA-42 Twin Star and helicopters such as the Airbus Helicopter AS350 [3] [4]. These aircraft were not designed for this type of mission and as result fly with considerably more equipment than is needed to record data and complete the primary mission. Much of this excess equipment – such as furnishings, windows, environmental controls - is related to the need to carry the pilot and any passengers or cargo safely and comfortably. If the aircraft can be operated uninhabited, the size and weight of the aircraft decreases dramatically which is very beneficial to the aircraft's performance. For example, the Brican TD-100 is a 22 kg UAV capable of carrying a 9 kg payload for 40 hours or up to 2,000 nautical miles (NM) [5]. By comparison, a DA-42 L360 4-seat general aviation aircraft weighs 1780 kg and has a maximum zero-reserve range of over 800 NM [6].

While civil UAV operators are not as concerned about the flight capabilities of their aircraft as are military operators or UAV designers [7] , it would be impossible to perform any of the listed missions unless the aircraft has adequate range or endurance. Achieving a SUAV's optimal performance is complicated by several factors, including poor methods of analyzing the aircraft's performance at low-Reynold's numbers and the lack of combined battery-motor-propeller analysis methods [8]. While all three components need to work together efficiently, the propeller offers the most potential to maximize the propulsion system's efficiency and performance.

The purpose of the propeller is to convert the mechanical energy from the motor (and in the case of an electric propulsion system, the chemical energy stored inside the battery) into thrust. Therefore the propeller directly influences on the aircraft's performance and drives the design of the propulsion system. Ideally the propeller will be

designed such that the required thrust is always produced while being driven by the motor and battery when both are operating at their peak efficiencies, though (as will be discussed) due to the nature of fixed-pitch propellers this is not always possible.

While off-the-shelf propellers intended for radio-control (RC) aircraft are widely used, selecting one is complicated by the lack of real-world test data [9] . Predicted performance is available from propeller manufacturers [10] but there are significant differences between it and the propeller's actual performance (see 5.2.6.1). Designing a custom propeller tailored to the aircraft's mission and propulsion system is a viable solution to this problem. The simple fixed-pitch nature of propellers enables them to be manufactured easier than custom electric motors and batteries that are significantly more complex.

Closely integrating the propeller with the aircraft's airframe and propulsion system is done with many manned aircraft to produce tangible performance benefits [11]. One recent example is the Daher-Socata TBM 900, a new version of the TBM 850 (a 6-passenger single-engine turboprop-powered aircraft) that featured a redesigned engine cowling, intake, exhausts and new propeller [12]. Daher-Socata provided its CFD analysis of the changes to the propeller's manufacturer, Hartzell, who used the information to design a propeller which closely integrates with the new intake and produces more thrust and less noise [12] [13]. The changes made to the propulsion system increased the available power by 80hp [12] which reduced take-off distance by 460-600ft and increased the cruise speed by 10 kts true airspeed (TAS) [12] [14].

2.3 Propeller Design

2.3.1 Propeller Operation

Propellers have been used since the earliest attempts at flight to drive powered aircraft and will be the primary alternative to turbofans for the foreseeable future [15]. Their operation can be explained by the classical momentum theory which is described in many books on aircraft propulsion and propeller design including [15] [16] [17] [18]. A summary of this theory is explained here based on the explanation and equations provided in [15] but for a detailed explanation the reader is referred to any of these sources.

Classical momentum theory assumes that thrust is produced due to a difference in the static pressure across an infinitely thin actuator disc. It is further assumed that:

- The velocity and pressure over the disc are constant and uniform;
- The air flows straight through the disc without rotation;
- The flow through the propeller is constrained to a well-defined stream tube; and
- The flow is incompressible

Based on the control volume drawn in Figure 1, at planes 1 and 4 the static pressure is constant and equal to the free-stream static pressure and planes 2 and 3 are immediately upstream and downstream of the propeller respectively. The difference at plane 4 between the flow passing out of the streamline and the flow leaving the remainder of the control volume is [15, p. 294]:

$$\Delta Q = A_3 V_3 + (S - A_3)V_0 - SV_0 = A_3(V_3 - V_0) \quad \textbf{Eq. 1}$$

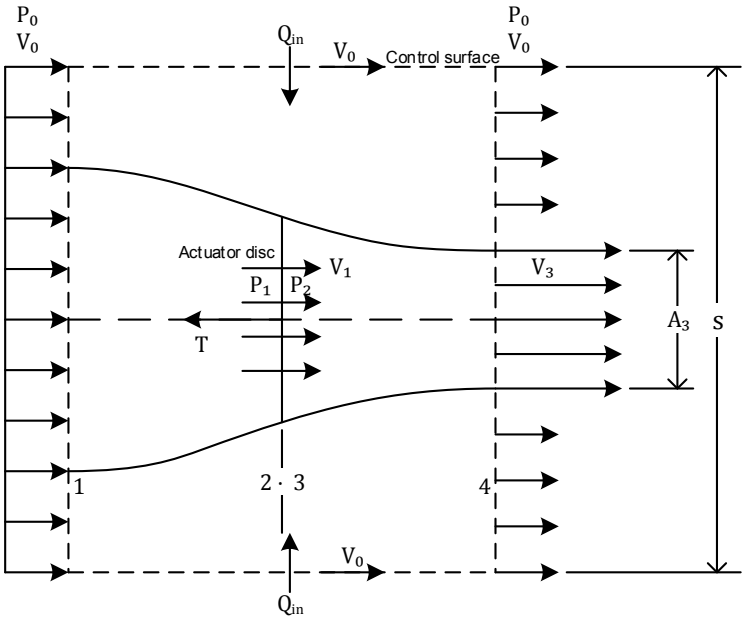

Figure 1 Classic Momentum Theory of Propellers (From [15, p. 294])

Applying the momentum theorem, the thrust, *T* generated by the disc is equal to [15, p. 294]:

$$T = \rho[A_3 V_3^2 + (S - A_3)V^2] - \rho S V_0^2 - \rho \Delta Q V_0 = \rho V_3 A_3 \quad \textbf{Eq. 2}$$

As the momentum model assumed that the pressure across the disc increased, the thrust generated by the propeller can be also expressed as [15, p. 294]:

$$T = A(p_2 - p_1) \quad \textbf{Eq. 3}$$

Based on Bernoulli's equation, the pressure difference also can be expressed as [15, p. 295]:

$$p_2 - p_1 = \frac{1}{2}\rho(V_3^2 - V_0^2) \quad \textbf{Eq. 4}$$

From the previous three equations the velocity of the air passing through the propeller is [15, p. 295]:

$$V_1 = \frac{(V_3 + V_0)}{2} \quad \textbf{Eq. 5}$$

$$V_3 = V_0 + 2wV_3 = V_0 + 2w \quad \textbf{Eq. 6}$$

$$V_1 = V_0 + wV_1 = V_0 + w \quad \textbf{Eq. 7}$$

Where *w* is the propeller-induced velocity. The thrust generated by the propeller is therefore [15, p. 295]:

$$T = 2\rho Aw(V_0 + w)T = 2\rho Aw(V_0 + w) \quad \textbf{Eq. 8}$$

This result means that the thrust generated by the propeller is due to increasing the flow through the propeller disc. The ideal induced velocity necessary to obtain a given amount of thrust is [15, p. 295]:

$$w = \frac{1}{2}\left[-V_o + \sqrt{{V_o}^2 + \left(\frac{2T}{\rho A}\right)}\right] \quad \textbf{Eq. 9}$$

The power consumed by propeller to create a given amount of thrust is [15, p. 295]:

$$P = \frac{1}{2}\rho A(V + w)[(V_0 + 2w)^2 - V^2] = 2\rho Aw(V_0 + w)^2 \quad \textbf{Eq. 10}$$

$$P = T(V_0 + w) \quad \textbf{Eq. 11}$$

The power required for the propeller can also be seen as the sum of the power that the propeller delivers to the aircraft for propulsion ($P = TV_0$) and the power that is needed due to the induced velocity ($P = Tw$) referred to as the induced power.

The ideal efficiency of the propeller in forward flight is equal to [15, p. 296]:

$$\eta = \frac{TV}{T(V+w)} = \frac{1}{1+(w/V)} \qquad \textbf{Eq. 12}$$

Figure 2 shows the velocity components acting on the blade. In practical terms, a propeller is a twisted wing that is spun on a plane to the forward direction of the aircraft. Throughout the UAV's flight, both the forward and induced velocity will change, affecting the angle of attack of the blade station. This has the effect of increasing or decreasing the thrust or torque acting on the blades. Thrust can be most efficiently produced at any forward speed with a variable-pitch propeller that allows for the blades to be rotated around their longitudinal axis [18, p. 12]. Rotating the blades changes the blade angle, β which changes the angle of attack (α) of the blade's airfoils.

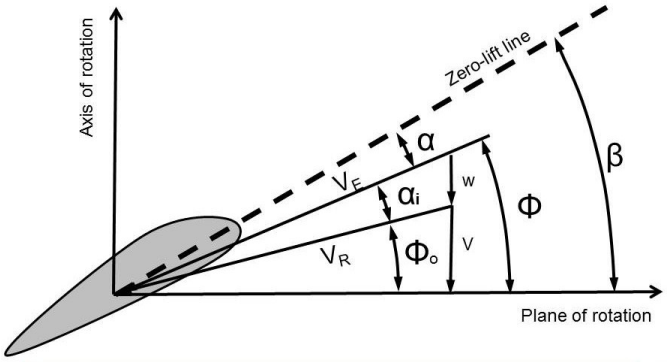

Figure 2 Angles and velocity components related to the performance of a propeller blade [15, p. 298]

Varying the blade angle in flight allows for:

- The maximum thrust-to-power ratio to be achieved for any rotational or forward flight speed. This is possible by making the angle of attack (α) for most of the

propeller blade's span the angle of attack at which the blade's airfoils reach their maximum lift-to-drag ratio.

- The propeller and engine to turn at a constant rotational speed by changing the angle of the blades to increase/decrease the torque needed from the engine. This so-called "constant-speed" operation is advantageous as it allows the engine to be operated at its most efficient speed [19, pp. 6-6].
- The blades to be feathered or rotated to be parallel with the direction of travel of the aircraft to reduce drag in the event of an engine or propeller failure [20]
- A reduction in ground roll distances following landing and greater descent rates by rotating the blades to produce negative thrust [20]

While variable-pitch propellers have been designed for larger UAVs [21] their weight and complexity would likely negate any performance benefit if used on a small UAV. SUAVs are equipped with fixed-pitch propellers directly driven by an electric motor or gas engine. Thrust is controlled by increasing or decreasing the power from the gasoline engine (with the propeller rotating at whatever speed is required to absorb the power from the engine) or the speed of its electric motor (as the torque required to turn the propeller can be obtained by controlling the current provided to the motor). As changing the rotational speed of the propeller will also change the angle between the relative wind and the blade (φ), the angle of attack needed for most of the blade to operate at or near its maximum efficiency will occur only over a small range of advance ratios (the ratio of the forward speed to rotational speed).

2.3.2 Design Methods

2.3.2.1 Early Propeller Design Approaches

Early propellers, or those designed before the end of the Second World War, were designed using an empirical approach. Propellers, which were found to have good performance characteristics during wind tunnel and flight testing, were scaled and modified as required to suit a specific aircraft and its engine [22]. One such example of this approach is documented in National Advisory Committee on Aeronautics (NACA) Technical Note (TN) 212 [22], which allows for a propeller to be designed for a light aircraft by calculating two coefficients.

The first coefficient, *J,* is the advance ratio of a propeller and is defined as:

$$J = \frac{V}{nD} \qquad \textbf{Eq. 13}$$

Where:

V = aircraft speed

n = revolutions per second

D = propeller diameter.

The second coefficient is defined as:

$$\sqrt{\frac{\rho V^5}{Pn^2}} \qquad \textbf{Eq. 14}$$

Where:

P = power

ρ = air density

This coefficient is unnamed in TN 212 but is known now as the speed power coefficient. Beginning *circa* 1930 [16] c_s was redefined as:

$$c_s = \sqrt[5]{\frac{\rho V^5}{P n^2}} \qquad \textbf{Eq. 15}$$

The pitch of the propeller, or the theoretical ratio of its forward motion per revolution, was constant for the entire blade, theoretically resulting in a constant angle of attack for each section of the propeller blade.

The speed-power coefficient and advance ratio are still used for the preliminary design of propellers for aircraft if the propeller is to be based on an existing design. This approach was widely used through the Second World War when pre-war propeller blade designs were scaled and used on a variety of wartime aircraft [17]. Blade design charts were a staple of many NACA reports on propeller performance published in the 1930s, and some of these designs were modified and produced by propeller manufacturer Hamilton Standard [23] [24]. A given blade design was not specific to a certain model or type of aircraft as the Boeing B-17, Douglas C-47, Lockheed Ventura, Consolidated B-24, and North American B-25 all used the Hamilton Standard 6477 blade [25]. It should be noted all four aircraft had wing-mounted radial engines and shared the same constant-speed hub, so with the exception of the difference between each aircraft's cruise speed and engine there was very little difference in the aerodynamics of the installation of the propeller. However with improvements to aircraft performance throughout the war came

the need for higher performance propellers which could not be achieved by scaling existing propellers. Most fighter aircraft were tested and operationally flown with several different propeller blades throughout the course of the conflict in an ongoing effort to improve their performance. One notable example was the Supermarine Spitfire that was originally designed with a 2-bladed fixed-pitch wood propeller and ended the conflict with 5-bladed constant speed propeller [26].

2.3.2.2 Traditional Methods of Design

Theories existed pre-war for the design of optimum propellers, beginning with Betz's theory in 1919. Betz's theory showed that the most efficient propeller will minimize induced power losses by having both a constant induced velocity and a constant wake pitch in the propeller's slipstream [15, p. 302]. Goldstein created a theory in 1920 to design propellers that would meet Betz's condition. The pitch angle of the wake, ϕ, was defined as [17, p. 38]:

$$\phi = \tan^{-1}\left(\frac{V}{\pi n D}\right) \qquad \textbf{Eq. 16}$$

The induced velocity could be calculated based on a circulation function, which was provided in charts for two and four bladed propellers [17, p. 38].

Goldstein's theory, but in particular his definition of the pitch wake angle, is acceptable for lightly loaded propellers where the induced velocity is much less than the forward speed of the aircraft [17, p. 40]. Under conditions when this is not true, such as when the propeller is operating at low forward speeds or high power settings, the accuracy of Goldstein's methods was found to diminish [17, p. 40]

Theodorsen modified Goldstein's methods with the major difference being that the wake pitch angle was modified to become [17, p. 40] :

$$\phi = \tan^{-1}\left(\frac{V + w}{\pi n D}\right) \qquad \textbf{Eq. 17}$$

The circulation function charts created by Goldstein relied on the radial position of the blade station and the advance ratio of the propeller. Similar charts were used by Theodorsen but considered $V+w$ rather than just V in the definition of advance ratio [17, p. 41]

Theordorsen's revisions also helped significantly in the design of propeller blades; when using Goldstein's theory a small error in the calculation of w can lead to serious errors in obtaining proper blade geometry [17, p. 41]. The application of Theordorsen's theory to propeller design was published in 1949 as NACA TR 924 [27] and formed the basis for the design of propellers as presented by Borst in the widely-used *A Summary of Propeller Design Procedures and Data* [17].

Borst notes that, while highly-efficient propeller blades are produced using the Betz approach, the actual maximum efficiency of a blade occurs when the power needed to overcome the blade's induced and profile drag is minimized for a given power input [17, p. 166]. This can be accomplished with the calculus of variation method as described and presented in [17].

If the solidity (or chord distribution and number of blades) and loading of the blade are allowed to vary, the induced velocity at any station of the blade is [17, p. 170] :

$$\bar{w} = V\left(-\zeta - \frac{\tan\gamma}{J/\pi x}\left[\zeta + 1 + \left(\frac{J}{\pi x}\right)^2\right]\right) \quad \textbf{Eq. 18}$$

Where:

$\gamma = tan^{-1}\left(\frac{C_D}{C_L}\right)$, where $\frac{C_D}{C_L}$ is the inverse of the airfoil's maximum lift to drag ratio

x = radial position of the blade station, or the distance of the station from the axis of rotation divided by the radius of the propeller

ζ = an arbitrary constant chosen to obtain the desired power or thrust coefficient.

Borst suggests the use of the calculus of variations method but notes that, in many cases, the difference in blade performance between using the calculus of variations method and Betz method is minimal.

Two other noteworthy methods of propeller design have also been commonly used. In 1926 Glauert published a work on the analysis of propellers using blade element momentum theory, but did not extend his work to cover the design of propellers [28]. The primary difference between a blade-element momentum theory (BEMT) and the vortex theories previously introduced are that BEMT approximates induced flow effects (through small angle approximations) and does not compensate for rotating flow or decreased thrust at the tip of the blade [15, p. 301]. Regardless, this approach is much simpler to use for analysis than vortex theory. A design method using BEMT was completed by Larrabee in 1970 [29] which, by meeting Betz's condition, allowed for the simple design of optimum propellers [28]. A revision of Larrabee's method, without the small angle approximations and simplifications, was created by Adkins and Liebeck in the mid-1980s for the McDonnell Douglas Company [24]. It should be noted that, with

the exception of BEMT being used for the approximate design of propellers, none of these theories are used in this work and are presented here for information only.

With the development and use of design methods not based on scaling existing propellers came the need for improved structural analysis methods. For scaled propeller designs, stress analysis was incredibly simplistic – for example in TN 212 the product of the diameter (in inches) and rotational speed (in RPM) is used to determine the type of wood the propeller is to be made from, and if the product was over 240,000 then the propeller should not be built [22]. Early structural analysis methods were a simplistic combination of the bending stress in the blade due to the blade's thrust and the axial stress from the centrifugal forces [16]. More advanced methods of structural analysis were provided in *ANC-9 Aircraft Propeller Handbook* [18]. The ANC-9 Handbook considered many of the forces that could not be considered with earlier analysis methods such as unequal blade loading and vibrations [16, p. 245]. The most complete approach to the structural analysis of propeller blades was presented in the second volume of Borst's handbook on propeller blades [30]. Borst's analysis methods were suitable for metal, wood and composite propeller blades and are still widely used [31] [32].

2.3.2.3 UAV Propeller Design

There has been some previous work performed on the design of propellers for UAVs. Borst authored a report in 1978 [33] focused on the design of UAV propellers between 24"-36" in diameter and powered by internal combustion engines. Borst showed that the methods used for analyzing the blades of full-scale propellers could be applied to

the design of propellers for UAVs as long as the aerodynamic data of the airfoils is available at the correct Reynold's number for the UAV flight regime.

A thesis prepared by Lorenz in 1988 detailed the design and wind-tunnel testing of propellers for the Stationary High Altitude Relay Platform (SHARP) aircraft [34]. It was found that it was possible to produce efficient propellers that functioned as designed; however no structural analysis was included in the design program.

While not specific to UAVs, Gur and Rosen present a multidisciplinary design optimization (MDO) approach to propeller design [32], which they note could be used to overcome the poor overall efficiency of UAV propulsion systems noted in [8]. Their approach considers aircraft and power plant performance, as well as the aerodynamic, structural and acoustic constraints of the blade. Theoretical analysis of a propeller designed using this method for an ultralight aircraft showed improved performance at the primary design point at the expense of performance in off-design conditions [32, p. 105] .

A thesis by Wall in 2012 looked at the design of optimized propellers for electrically-powered UAVs [35]. Wall's approach optimized not only the propeller blade to suit the performance of the motor but also included airfoil optimization. Based on simulations, the optimized propellers performed better than the baseline propeller and it was concluded that there were distinct differences in blade planform between climb and cruise propellers [35, p. ii]. This approach did not consider structural strength or propeller performance in other phases of flight.

While the benefits of optimized propeller performance in the intended phase of flight are undeniable, this optimization may not be the best approach for the overall

performance of the aircraft. Given the noted differences in blade planform [35] and poor off-design performance [32], it is very possible a highly-optimized propeller would be overall worse than an unoptimized propeller (or even be unusable) due to the poor performance throughout the rest of the aircraft's flight envelope. As a result it may be preferable to have less-than optimum performance in the primary flight condition such that the propeller is better suited to the aircraft's overall mission. Another shortcoming of the previous works reviewed on UAV propeller design was that there was the lack of information on structural analysis, manufacturing and testing of the propellers. While time consuming, if the design cannot be manufactured and safely flown its theoretical efficiency is irrelevant.

2.3.3 Airfoils for Propellers

2.3.3.1 Propeller Airfoil Series

A number of airfoils and airfoil series have been used for propeller blades with a few representative airfoils is shown in Figure 3. Most propellers designed before World War Two used airfoils with a flat lower surface such as the Clark Y airfoil and, to a lesser extent, the RAF 6 [23] [24]. One major reason for their use is that the flat lower surface allowed for accurate blade angle measurements to be made during manufacturing and maintenance [36]. Both airfoils do have favourable aerodynamic traits such as a high-maximum lift coefficient and benign stall characteristics. However, testing by NACA showed that the Clark Y did not perform well in compressible flow [36] which lead to the use of what became the two "classic" propeller airfoil families - the NACA 16- series and the NACA 65- series. It should be noted that the use of the Clark Y did not end with the introduction of these airfoil families as modern propellers are still designed using them

[36] [37]. Both the NACA 16- and 65- airfoil families were created in the mid-late 1930s - early 1940s and offer less drag in compressible flow regimes. The 65-series airfoils have the advantage of a drag bucket, or a reduced drag over a narrow range of lift coefficients due to laminar flow around the airfoil. This is beneficial, especially for a fixed-pitch propeller, as it increases the range of advance ratios the propeller can perform near its peak efficiency.

By the mid-late 1970s, advances in aerodynamics prompted British propeller manufacturer Dowty Rotol to seek a new family of propeller airfoils [38]. Their search led to the development of the ARA-D series, which was created by the Aircraft Research Association. ARA-D airfoils offered a higher lift coefficient for better take-off performance and have a thicker shape designed for a stiffer, easier-to-manufacture blade [38]. These airfoils were used for the composite propeller blades flown on a variety of transport aircraft propellers such as the Bombardier Q400 [39], Saab 2000, and Lockheed Martin C-130J.

From examining propellers flown on SUAVs and reviewing the information available on their manufacturer's websites [40], it was found most typically used flat- or near- flat- bottomed airfoils (such as the NACA 4412) in modified form.

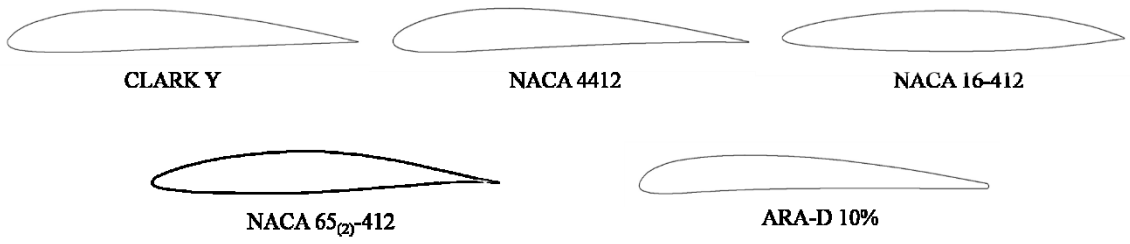

Figure 3 Airfoils commonly used for propeller blades

While it is possible to use a single airfoil for most of the propeller blade, usually several discrete airfoils are needed for aerodynamic and structural reasons. Typically an airfoil with a low thickness-to-chord ratio (t/c) is used near the tip of the propeller blade to obtain a thin cross-section and for its higher critical Mach number, both which are needed to reduce the drag created by high-speed compressible air flowing over the blade tip. The thickness of the blade then increases with the span as is necessary for adequate structural strength and stiffness, until the root where the blade becomes very thick. For a fixed-pitch propeller the increase in thickness is needed to smoothly blend the blade into the hub to avoid stress concentrations. If the blade is part of a variable pitch propeller the thickness increase near the root is either as a result of changing the cross-sectional shape from an airfoil into a shaft (for forged or machined propeller blades) or to accommodate a shaft being installed in the root of the blade for composite blades.

Studies by the National Advisory Committee on Aeronautics (NACA) in the early 1930s [41] showed that if the camber and camber position of an airfoil are held constant, the lift-curve slope, profile drag and zero-lift angle of attack changes proportionally to the thickness-chord ratio. This trait allows for a blade to be designed by scaling the co-ordinates of a single airfoil to achieve the necessary thickness, and the scaled airfoil's aerodynamic properties can be estimated based on its thickness-chord ratio. Equations for the aerodynamic properties of two airfoils commonly used for propellers, the Clark Y and RAF 6, are available in [15] [42] and can be used for estimating the performance of most propellers, especially those for general aviation aircraft which often use these airfoils. However, these approximate relationships do not exist for all airfoil families and may not accurately reflect the true aerodynamic properties of a given airfoil. To avoid

scaling, the propeller design program was written with the intent of using a family of airfoils – airfoils with the same camber and camber position but varying thicknesses – so that the true aerodynamic properties of any of the propeller's airfoils is known.

2.3.3.2 Airfoil Data

For the code's development the NACA 44xx airfoils were used due to their use in existing props, their high maximum lift coefficient, and fairly benign stall characteristics. The aerodynamic characteristics of the NACA 44xx series, as well as other propeller airfoils such as NACA for the 16- and 65- series , are widely available [43] [44] [45]. However all of this data was collected at Reynold's numbers of 3×10^6 and higher, well out of the range of Reynold's numbers seen for SUAV propellers (typically <300,000 [33]). Some aerodynamic data at low Reynold's numbers is available for the NACA 44xx series in NACA TR 586 *Airfoil Section Characteristics as Affected by Variations of the Reynolds Number* [46], however due to tunnel effects serious doubt about the accuracy of the data is raised by the authors.

Three separate methods of obtaining sufficient airfoil data at low Reynold's numbers for design purposes were examined as discussed below.

2.3.3.2.1 Correction Factors

In the early 1970s there was very little low Reynold's number airfoil data available for propeller design [33, p. 23] . As a result correction factors were developed based on trends noted by Jacobs and Sherman in [46] allowing for aerodynamic data obtained at a higher Reynold's number to be scaled down for lower Reynold's numbers.

The primary aerodynamic characteristic that needed scaling was the drag coefficient which, for any given lift coefficient, rises as the Reynold's number decreases. NACA TR 586 also shows that the stall angle of attack (AOA) and stall lift coefficient, C_l will change with increasing angle of attack while the lift curve slope of an airfoil will generally remain unchanged.

To compare the accuracy of these correction factors to wind tunnel data, the characteristics of the NACA 4412 at Rn $3x10^6$ were scaled down to a range of lower RNs and compared to data for this airfoil available in [33] at Reynold's number 50,000 – 250,000. It was assumed that at Reynold's numbers greater than 500,000 the scale factors were not required, as the trends in TR 586 that showed that there was little variation in stall lift coefficient and drag coefficient above 500,000. Based also on this same data, a trend for maximum lift coefficient obtainable at any Reynold's number was developed. Borst [33] comments that the airfoil data published is not particularly accurate and suggests it be used for general trends only. The scaled drag coefficient correlated to wind tunnel test data (Figure 4 and Figure 5) but the drag was significantly lower than test data, especially in the region of lift co-efficient used for propeller design (typically 0.4 – 0.7).

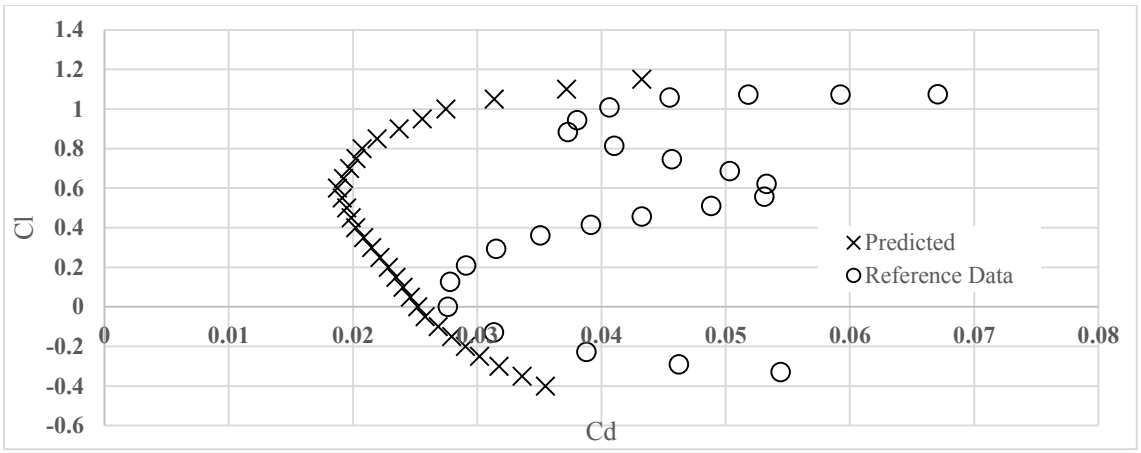

Figure 4 Drag polar for a NACA 4412 airfoil at Rn 60,000 predicted using drag characteristics at Rn = 3 × 10^6 and correction factors noted in [33] . Reference data is wind tunnel data from the same source

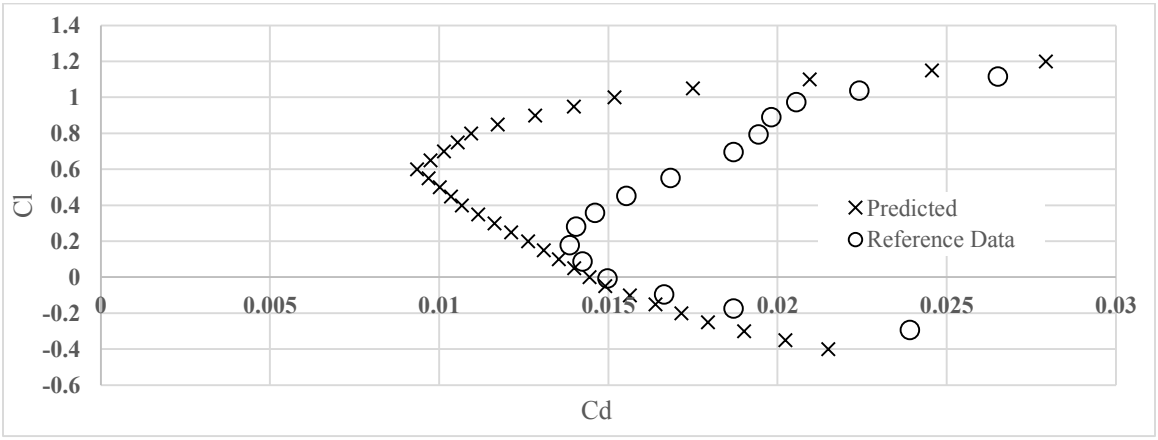

Figure 5 Drag polar for a NACA 4412 airfoil at Rn 250,000 predicted using drag characteristics at Rn = 3 × 10^6 and correction factors noted in [33] . Reference data is wind tunnel data from the same source

Scale factors are simple to apply and can allow for nearly any airfoil data to be used for propeller design. However as an incorrect estimate of the airfoil's drag would eliminate the likelihood of being able to predict propeller performance accurately other methods were considered.

2.3.3.2.2 Use of XFOIL for Predicting the Lift and Drag Characteristics of Airfoils at Low-Reynolds Numbers

One of the most widely used tools for analyzing airfoils, especially at low Reynold's numbers, is XFOIL. XFOIL is a computational fluids dynamic (CFD) program using panel-methods. It was created specifically for low Reynolds number airfoil data in the early 1980s [47] for the MIT Daedalus human powered aircraft. Since its creation it has continually been upgraded [48] and validated [49] [50] making it a very mature and widely used analysis tool.

While it is possible to interface XFOIL with MATLAB as demonstrated in [49], it would be inefficient to use an XFOIL lookup for all calculations needing airfoil data due to the time it would take to run and find properties at each point. Data was collected from XFOIL for several airfoils and a MATLAB function was written to interpolate the tabulated data for an airfoil within the range of thicknesses and Reynold's numbers. For example, if the properties of a NACA 4414 airfoil at a Reynold's number of 198,300 are desired, they would be determined by interpolating from the properties of the NACA 4412 and NACA 4415 airfoils at a Reynold numbers of 75,000 and 300,000. This method works reasonably well with tabulated drag predictions being close to those predicted by XFOIL of the actual drag polar of the airfoil (Figure 6).

XFOIL struggles to converge when predicting the properties of airfoils with a viscous solution at Reynold's numbers of less than 100,000 and as the thickness – chord ratio of the airfoil increases. As a result, tabulated data is available only for Reynold's numbers above 75,000.

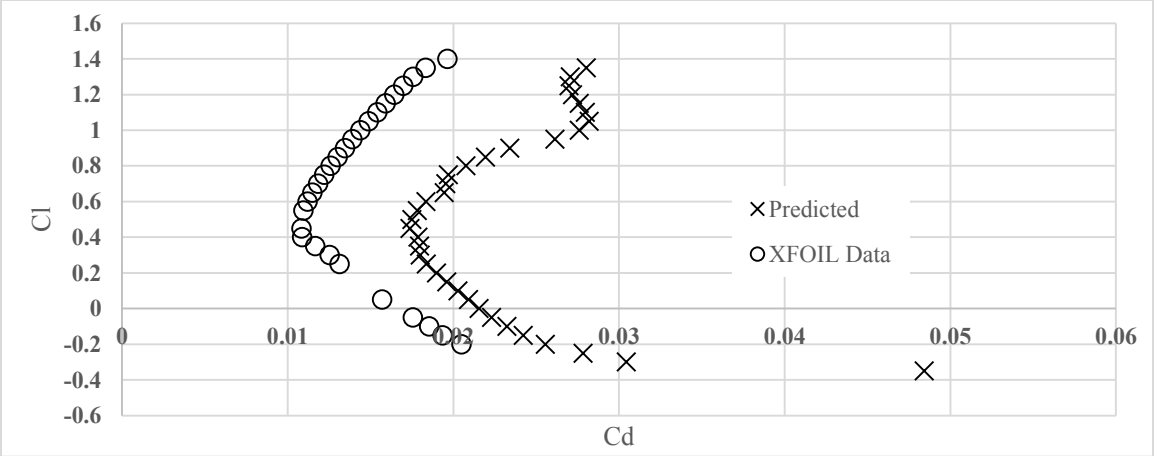

Figure 6 Drag polar of a NACA 4414 airfoil at Rn 198,300 as predicted through interpolated data and by XFOIL

2.3.3.2.3 Hybrid Approach for Predicting the Lift and Drag Characteristics of Airfoils at Low-Reynolds Numbers

It would be problematic to assume that the properties of the airfoil at Reynold's numbers less than 75,000 would not change further. This is because below a critical Reynold's number (generally between 10^4 and 10^6) the flow will remain laminar and the drag will increase due to viscosity, and above this critical Reynold's number the drag will decrease as the flow becomes turbulent. To compensate for this shortcoming of XFOIL, a correction factor method based on the one presented in [33] was used.

The correction factors in [33] were meant to correct data from a Reynold's number of 9 x 10^6 to a Reynold's number of 50,000-300,000. The original factors did not work well and so instead new ones were created using the same technique described in [33] and using the data for the NACA 4409, 4412, and 4418 airfoils. As shown in Figure 7 and Figure 8, this method provided corrected drag coefficients similar to those from test data.

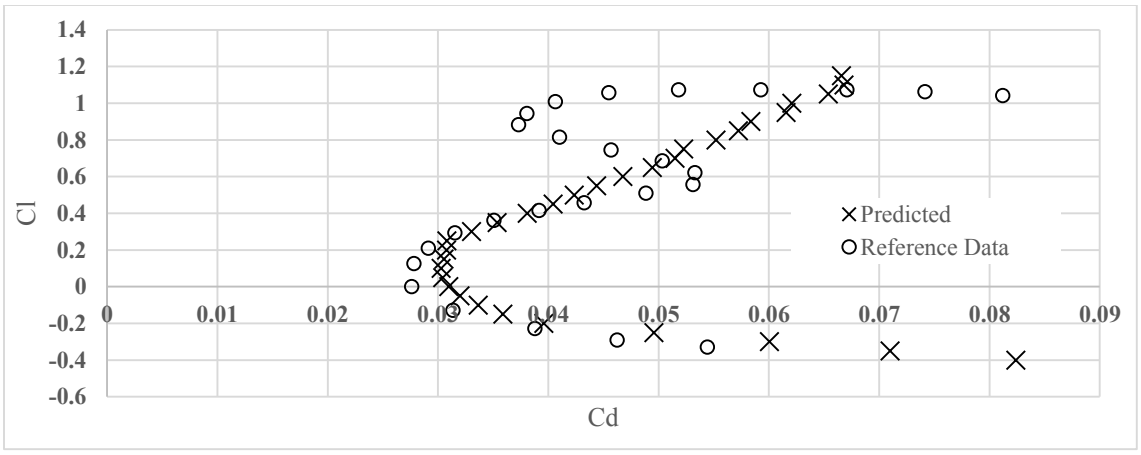

Figure 7 Drag polar for a NACA 4412 airfoil @ Rn 60000 as predicted using correction factors and XFOIL data at Rn 75000 Wind tunnel test data was obtained from [33]

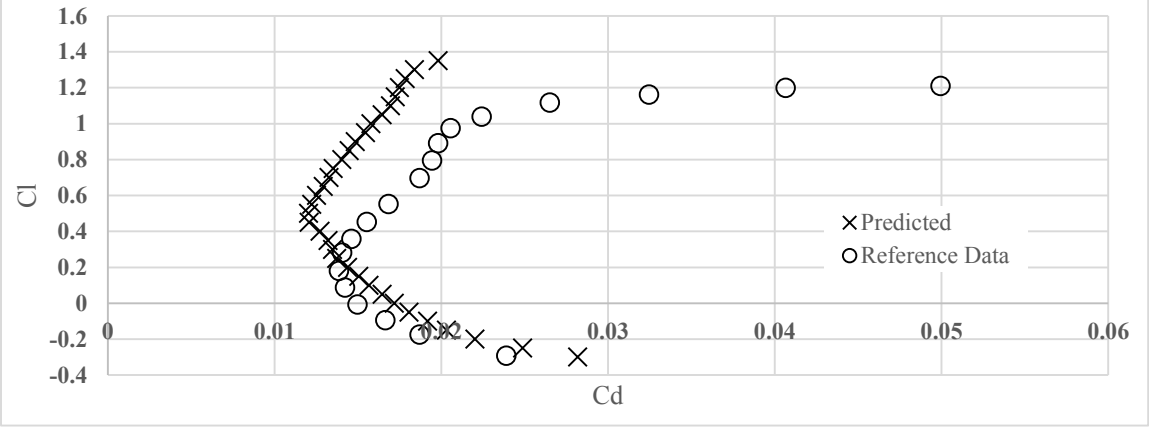

Figure 8 Drag polar for a NACA 4412 airfoil @ Rn 250,000 based on interpolated XFOIL data. (between Rn 75,000 and Rm 300,000) Wind tunnel test data was obtained from [33]

2.4 Design and Testing Requirements for UAV Propellers

2.4.1 Certification Requirements

A major influence in the design of any aeronautical product (such as a propeller, aircraft, instrument, etc.) is the need to conform to the applicable airworthiness standards so that a type certificate can be issued by the civil aviation authority (CAA) such as the European Aviation Safety Authority or Transport Canada.

In Canada, UAVs are currently not type certified or integrated into the national airspace system like manned aircraft, complicating the operation of UAVs in civil airspace. Approval to operate a UAV is granted by the Minister of Transport (Transport Canada) on a case-by-case basis through the issuing of a special flight operations certificate (SFOC). An SFOC is usually very restrictive, typically granting the holder permission for a finite duration to operate a given UAV within a geographical area during daylight hours, within the line of sight of the operator and a spotter, and in compliance with other conditions (i.e. not over occupied buildings or people not associated with the UAV operations or requiring the monitoring local air traffic control radio frequencies) [1]. A few companies that have demonstrated sufficient experience with UAV operations have been offered blanket SFOCs to allow for operating a UAV within a certain geographical area for a longer duration without the need to apply for a new SFOC for each UAV operations. As (at the time of writing) over 1,000 SFOCs had been issued for UAS operations in Canada.

Transport Canada formed a working committee (the Canadian Aviation Regulation Advisory Committee (CARAC) UAV System Program Design Working Group) to recommend changes and additions to the Canadian Aviation Regulations (CARs) necessary to integrate small UAVs (<25 kg)[1] that are operated within visual line of sight UAV operations into the national airspace system [1, p. 3]. This committee prepared recommendations on the organizational structure, pilot qualifications and design standards for UAV which were accepted by Transport Canada and will eventually become part of the

[1] It should be noted that the weight definition of small UAVs has seemingly changed from 20-35 kg (as of 2011) to less than 25 kg (December 2013).

CARs. Until they are included in the CARs the recommendations are being used as best-practices guidance for UAV operators applying to obtain SFOCs [1, p. 3]. By complying with the best practices, UAV operators may become eligible to receive SFOCs for larger geographical areas and longer durations [1, p. 3] .

Complying with these best practices requires that the operator provide Transport Canada with manuals for the UAV's operation, maintenance and training and statements of compliance from the manufacturer stating the aircraft's type design meets the best practices and that a particular airframe conforms to the type design. Transport Canada does not anticipate that small UAVs will be issued type certificates, so this process will remain after UAVs are introduced into the national airspace system [1, p. 2]. Proof that the aircraft's type design complies with the best practices needs to be substantiated through documented analysis and testing (both on the ground and in flight) which showed the UAV had acceptable and safe performance [1, p. 12]. Demonstrating compliance with some best practices is fairly straightforward (for example as the use of locking devices on crucial fasteners), but for other best practices it becomes a little more difficult due to the lack of explicit guidance. For example, Section 3.4.5 requires the UAV's structure to be designed for all expected operating conditions (including gusts) and there be a safety factor of 1.5 under representative limit load cases system [1, p. 14]; however, unlike for CAR 523 and 525 no gust speeds or equations are provided. Therefore, manufacturers wishing to comply with the best practices may need to consult airworthiness regulations for larger aircraft guidance on the analysis and testing to demonstrate compliance.

Section 3.4.7 of the best practices is devoted to best practices for the design of the aircraft's propulsion system. Two requirements directly pertain to the design of propellers for small UAV:

5XX.7.1 If a single failure within the propulsion system could result in the loss of control of the UAV trajectory:

> *5XX.7.1.1 the probability of such a failure under all expected operating conditions shall be extremely remote, or*
>
> *5XX.7.1.2 there shall be a means of initiating flight-termination in the event of such a failure.*

5XX.7.3 Any propellers or rotors shall have sufficient strength to ensure safe operation throughout the flight envelope.

Also included in the best practices (as in section 3.4.9, from 5xx.9) are requirements to state, in the operating and maintenance manuals, a maximum operating speed for the motor/engine and propeller, as well as drawings and instructions for the installation and assembly of the propeller [1, pp. 20-22].

The requirements of 3.4.7 of the best practices could be met through structural analysis of the blade and completing a series of flight and ground tests to show the propeller can operate throughout the full flight envelope at the maximum obtainable rotational speed of the motor or engine. Given UAVs typically use commercially-available propellers for radio controlled (RC) aircraft, most operators would buy a high-quality propeller and fly it on the aircraft assuming it has been sufficiently analyzed and tested by the propeller's manufacturer. Manufacturers of RC aircraft propellers tend to detail their design methodology and provide maximum safe speeds [40], making further analysis unnecessary. However, if the operator/UAV manufacturer is also becoming the propeller's manufacturer, flying a propeller without analysis or suitable ground testing

presents a much higher risk of propeller failure which could result possibly in the loss of the aircraft. No explicit instruction is given in the best practices on what constitutes sufficient strength and how to perform adequate testing - should the design include some margin of safety in a worst-case scenario or does the propeller need to survive only up to the limits of what would need to be seen in flight? The conditions and duration necessary for ground and flight testing of a propeller for a UAV are also not provided.

To establish criteria for the design and testing of the UAV propellers, two regulations used for certifying propellers for manned aircraft, FAR 35 and ASTM F2506-13, were reviewed.

2.4.1.1 Federal Aviation Regulations - Part 35 (FAR 35)

The chapter of the CARs relevant to propeller design (CAR 535) [51]is a version of the airworthiness standard for propellers adopted from the equivalent section of the United States, FAR 35 [52], with only some minor wording changes to account for regional differences. As FAR 35 is supported by several advisory circulars to better describe the criteria for meeting various requirements and is the basis of CAR 535 [51], it was reviewed instead.

FAR 35 details the design standards applicable to both fixed and variable pitch propellers that can be used on any certified aircraft. Unsurprisingly, due to its broad scope a large number of sections of FAR 35 are not directly applicable to fixed pitch propellers, either as stated in the regulations or due to the absence of a given feature (such as electronic controls). Neglecting the requirements for non-existent features, designing a propeller to meet some other certification requirements would be impractical

due to the small size of the UAV and propeller. For example, it would be irrelevant if the propeller were to survive a lightning or bird strike as both would impart such a significant amount of energy, either electrical or mechanical, into the UAV that the resulting damage would make continued flight impossible because of the damage to the airframe and avionics.

The key applicable requirements relevant to the design and testing are summarized below:

Design:

1. The propeller may not have features or characteristics that would make it unsafe for the uses in normal operating conditions. (§35.7)
2. The suitability and durability of materials used in the propeller must be established on the basis of experience, tests, or both and account for environmental conditions expected in service. The design values of properties of materials must be suitably related to the most adverse properties stated in the material specification for applicable conditions expected in service. (§35.17)
3. The maximum stresses developed in the propeller may not exceed values acceptable to the Administrator considering the particular form of construction and the most severe operating conditions. (§35.24).

Testing:

1. The hub and root of the blade must be tested for an hour at a load equivalent to twice the maximum centrifugal load to which the propeller would be subjected during operation at the maximum rated rotational speed without evidence of

failure, malfunction, or permanent deformation that would result in a major or hazardous propeller effect. Components used with or attached to the propeller (for example, spinners, de-icing equipment, and blade erosion shields) must be subjected to a load equivalent to 159 percent of the maximum centrifugal load to which the component would be subjected during operation at the maximum rated rotational speed by either testing at the required load for a period of 30 minutes or analysis based on test. (§35.35)

2. Fatigue limits must be established by tests, or analysis based on tests, for the propeller taking into account all known and reasonably foreseeable vibration and cyclic load patterns that are expected in service and expected service deterioration, variations in material properties, manufacturing variations, and environmental effects. A fatigue evaluation of the propeller must be conducted to show that hazardous propeller effects due to fatigue will be avoided throughout the intended operational life of the propeller on either the intended airplane or a typical airplane. (§35.37)

3. Endurance tests of a propeller system must be made on a representative engine without evidence of failure or malfunction. Fixed-pitch and ground adjustable-pitch propellers must be subjected to one of the following tests:

    (1) A 50-hour flight test in level flight or in climb. The propeller must be operated at takeoff power and rated rotational speed during at least five hours of this flight test, and at not less than 90 percent of the rated rotational speed for the remainder of the 50 hours.

(2) A 50-hour ground test at takeoff power and rated rotational speed. (§35.39)

It should be noted that centrifugal load testing does not apply to fixed-pitch wood or metal propellers, and that fatigue testing also does not apply to fixed-pitch wood propellers of conventional design [52].

While some of the key design criteria of FAR 35 are reasonable to use for the design of UAV propellers, testing to meet the "letter of the law" of FAR 35 would be a very lengthy process and would not allow new propellers to be fielded in a timely manner.

Endurance testing a UAV propeller for at least 50 hours is excessive given that the lifespan of small UAVs is known to be significantly shorter than manned aircraft. The Office of the Secretary of Defense (OSD) [53] reviewed the reliability of UAS systems used by the US Department of Defense and suggests that the mishap[2] rate of a UAV increases as the Reynold's number of the wing when the aircraft is in cruise decreases. One of the factors that contributes to this trend is that there historically has been more research on the aerodynamics and control of larger and faster aircraft (with higher Reynold's numbers) while there has been less work on aircraft stability and control at low Reynold's numbers [53, p. 38]. Extrapolating from the trend between the cruise Rn and the aircraft's mishap rate, UAVs with a cruise Rn between 100,000 and 1,000,000 could expect to see ~350 – 10,000 mishaps per 100,000 fleet flight hours. Therefore, an individual airframe may fly anywhere between 10 and 250 hours before it is involved in a

[2] Class A mishaps are defined as aircraft accidents resulting in loss of the aircraft, human life, or causing over $1,000,000 in damage [51, p. 23]

mishap and written-off, making a 50-hour test period for the propeller excessive. In addition, some small UAVs (such as the Aerosonde) lack landing gear and belly land or strike a net, occasionally destroying the propeller. In this case it would be truly irrelevant if the propeller could last more than a single flight.

Vibrations, environmental degradation, and fatigue are difficult to analyze for a plastic 3DP propeller installed on a UAV, however it is probable that all three under normal circumstances, can or need to be neglected for a few reasons. While UAVs can be damaged by rain and UV radiation, the low-cost nature of most of their components and short lifespan makes them "throw-away aircraft'. Electric motors do not produce vibrations of the magnitude associated with gas engines and so, assuming the blade has been well-balanced, there should be no major vibrations. In addition, while proven methods exist for the fatigue and vibration analysis of propeller blades [18] [30] [54], the fatigue characteristics most 3DP materials have not been well-studied [55] making it difficult to establish the lifespan of blades.

2.4.1.2 ASTM F2506 *Standard Specification for Design and Testing of Light Sport Aircraft Propellers*

F2506 *Standard Specification for Design and Testing of Light Sport Aircraft Propellers* covers the design standards for propellers made specifically for Light Sport Aircraft (LSA) in the United States [56]. Light sport aircraft are a class of light aircraft intended for recreational flying, with a maximum take-off weight of 1320 lb, capacity of 2 persons (including the pilot), a 120 kts indicated air speed (IAS) maximum level flight speed, a 45 kts maximum clean stall speed, and a single engine equipped with a fixed or

ground-adjustable propeller [57]. The smaller, slower, and simpler nature of LSA aircraft make the standards written for these aircraft much more applicable to UAVs than standards for larger transport aircraft. The process for certifying LSAs (or components for them) is very similar to that expected for UAVs, as the manufacturer designs and tests the aircraft to meet a design standard (ASTM F2245 [57]). The applicant then declares that they meet the requirement and the FAA reviews test data and inspects the aircraft, but will not award a type certificate.

ASTM F2506 has much of the same content as FAR 35 with regards to the design of a propeller but has different requirements for testing propellers. Under FAR 35, many tests are not applicable to fixed-pitch wood propellers and fatigue and vibration analysis is needed for all propellers except for those made of wood. The F2506 standard instead requires all propellers, regardless of what material they are constructed of, to undergo a centrifugal load test and an endurance test. Fatigue and vibration analysis is required only for metal propellers and is considered optional for those manufactured from wood or composite materials. If vibration and fatigue testing has been completed the propeller needs to undergo a 50-hour endurance test (the same as detailed in FAR 35.35) but if one has not been done, a 100-hour endurance test instead needs to be completed. The 100-hour test requires running the propeller at various percentages of the maximum rated power, and is to be done in order of increasing power settings. The power schedule includes [56, p. 7]

- 15 hrs @ Idle
- 15 hrs @ 25% Maximum Declared Cruise Power (MDCP)
- 20 hrs @ 50%, 75% and 100% MDCP

- 10 hrs @ Maximum Declared Take-off Power (MDTP) & Maximum Declared Take-off RPM (MDTR)

These requirements were written for LSA aircraft, and presumably durations that the propeller is run at each power setting reflect the relative frequency that the setting is used in flight.

Given the current lack of suitable fatigue data of 3D printed polymers, the more experimental approach to fatigue testing presented in F2506 seems appropriate to ensure that there are no fatigue or vibration issues. The power schedule provided is also similar to that which will be used for propeller performance testing in the low-speed wind tunnel. A 100-hour endurance test is even more excessive than the 50-hour test suggested in FAR 35 but it could be scaled down in duration to a more reasonable duration.

Two of the power settings suggested for the test could also be eliminated as they are inappropriate for an aircraft driven by an electric motor:

- Idle speed is the rotational speed that an engine will run at when not under any load. As electric motors can be started and stopped as required they do not have an idle speed. As running the propeller at just over no-load speed of the motor would likely not develop any usable thrust it is very unlikely that the prop would be run at this setting in service for any appreciable duration.
- There is no need to test the motor at a setting beyond MDCP, which for an electric motor is maximum speed possible at the maximum continuous allowable current draw. Most electric motors can draw current from above their maximum continuous ratings for only a few seconds at a time before the motor is damaged.

This is different than gas engines where take-off power (the engine at its maximum safe operating limits) is permissible for a few minutes. Dedicating 10% of the total test time to operating a motor at a setting that would likely destroy the motor is risky and very little is to be gained by testing the propeller in an unlikely operating condition.

Given the short lifespan of a UAV a 10 hour test duration could be appropriate, as testing the propeller for this duration could be accomplished within a few days of testing. Based on roughly 10 hours of test time, and the distribution of test hours for each power setting:

- As Required @ <25% for checking vibrations
- 1 hr @ 25% operating throttle range
- 3 hrs @ 50%, 75%, 100% of operating throttle range

The operating throttle range is considered to be the range of throttle settings between the lowest setting needed to turn the propeller and the highest throttle setting that the motor can be continuously operated at.

2.4.2 Other Design Requirements[3]

Aside from meeting regulatory requirements, propellers need to be able to function in their operation environment for their intended lifespan. Borst [30] provides a

[3] This section contains material originally published and presented as "A Process for the Design and Manufacture of Propellers for Small Unmanned Aerial Vehicles" as part of the Canadian Aeronautics and Space Institute AERO 2013 conference.

list of basic blade design criteria pertaining to the aerodynamics, manufacturing, material selection, structural design, and maintenance of propeller blades. This list is intended as a starting point for the design of propeller blades for manned aircraft, and is not entirely applicable for those intended for use on UAVs due to the single-piece fixed-pitch design or due to the consequences of the event on the overall UAV (for example, it would be impossible for a small propeller to cut through a 1 ½" – 3" hardwood tree branch or survive being hit by a .50 bullet).

One key difference between manned and unmanned aircraft is that the propeller may be a single-use item. If a non-folding propeller and engine are mounted on the front of a UAV that belly lands, or if a net is used to catch the aircraft, the propeller is usually destroyed [53, p. 33].

From the list provided in [30] a few relevant design criteria were identified:

Reliability & Survivability:

- Minor impact damage from the ground, stones, and other debris should not affect the continued safe flight for at least that mission [30, p. 217].
- The maximum allowable stresses should be chosen considering service damage and manufacturing defects. [30, pp. 215, 217]
- While propeller blades typically have long operating lives [30, p. 215], the propeller will need to have an operating life of at least 10 hours (but preferably longer).
- The blades need to be able to operate in temperatures between -53^{O}C and 74^{O}C and cannot be degraded from exposure to ultraviolet light [30, p. 217]

Producibility

- Automation, especially for critical or time-consuming operations, should be maximized. This reduces touch time and allows for a more reproducible blade [30, p. 218] [30, p. 218]
- A single piece propeller is preferable [30, p. 218]

Inspectability and Maintainability

- The pre-flight inspection of the blade should consist of nothing more than cleaning the propeller and inspecting for signs of damage [30, p. 219]
- The propeller should be easy to replace in the field [30, p. 220]

Material

- Materials which have been fully qualified through coupon testing [30, p. 220] and are currently used in either the aerospace or automotive industries are preferred for use.

Meeting the reliability and survivability criteria requires the application of damage tolerant design principles, which would allow for the operation of propellers with a flaw or crack below a given size. However it is accepted practice among RC aircraft pilots that a propeller with any damage be discarded [58], and so operators will be encouraged not to use propellers with any visible damage. Given the failure of the propeller would likely result in the loss of the UAV, and as the cost of propeller is a small portion of the overall cost of the aircraft, not replacing a damaged propeller significantly and needlessly increases the risk of catastrophic failure.

2.5 Materials and Manufacturing

2.5.1 Overview of Materials for Propellers

Propellers were originally made of wood but have been made from steel and aluminum since the 1920s and from advanced composite materials since the 1970s. While the latest composite materials have excellent mechanical properties, wood and metal propellers still continue to be widely designed and produced. Propellers for RC aircraft are often manufactured from wood and composites as with manned aircraft, but also from reinforced plastics due to their low cost and weight and high strength.

2.5.1.1 Wood

Wood has some characteristics that make it a favoured material for propellers but also some significant drawbacks [16, p. 213]. Wood offers a high strength-to-weight ratio and its ultimate strength is not significantly affected by fatigue [16, p. 213] . The wood's resistance to fatigue is due to its high internal friction, or hysteresis, which is so effective at dampening vibrations that fixed-pitch wood propellers do not need to complete many of the tests required for certification [16, p. 213] [FAR 35.35, 35.36, 35.37, 35.38]. However, wood is prone to warping due to temperature and humidity and is easily damaged, or eroded, when impacted by pebbles, rain, or water spray [16, p. 213] Milling propellers from laminations, or thin strips of wood (typically ¾" thick) glued together, rather than a single large block of wood reduced warping, and incorporating brass erosion guards on the tips of the blade improved erosion resistance [16, p. 213] . However, by the

early 1930's metals were being used instead of wood for propellers operating in harsh environments for greater durability [16].

Fixed-pitch wood propellers continue to be designed and produced for general aviation, ultralight, homebuilt and unmanned/RC aircraft in a variety of sizes. Fabric-reinforced wood blades have evolved into the wood-composite blades which use the wood as a core for a carbon fibre, Kevlar or fibreglass skin (these will be described in the section on composite propeller blades). Wood is a well-proven easily-obtainable material and CNC milling machines can readily produce a propeller from a CAD part.

However, there are several drawbacks to using wood for custom propellers. While a CNC milling machine can quickly produce a propeller, the blades be manually sanded and balanced for the propeller to have the best possible performance [59]. This is counter to the typical preference to eliminate as much "touch time" and human interaction in the manufacturing process as possible to reduce the cost and improve the repeatability of the blade. Blade erosion has been shown to be a major issue on some UAVs [53], with rainstorms shredding a propeller in minutes. Wood propellers typically have a greater minimum thickness than ones made from composites or plastics for sufficient strength which limits the thickness of airfoils, especially on the outer sections of the blades.

Wood could be used to manufacture propellers for this process. If propellers were being produced for internal combustion engines rather than brushless DC motors, would likely be used as its excellent dampening characteristics would eliminate some of the risk of a structural failure due to resonance from the vibrations due to the motor. However, due to its draw backs other materials were investigated.

2.5.1.2 Metal

Metal propellers were developed starting in the 1920's as an alternative to wood propellers [16, p. 218]. Metal propellers are usually made from forged and machined aluminum slabs or from extruded and welded steel tubes. Metal propellers however are not used for RC aircraft or small UAVs. This is due to the relatively high weight of the blades (as compared to wood and composite propellers) which adds to the aircraft's empty weight and reduces the response of the motor to commanded speed changes. Another reason that they are not used is because RC aircraft have a significantly higher crash rate than manned aircraft and are typically flown much closer to both the operator and spectators. If the propeller failed during a crash, a metal blade's greater kinetic energy and its knife-like geometry may kill rather than injure if it were to strike a person.

2.5.1.3 Composites and Plastics

While composite materials are typically seen as a recent advancement in aviation, the first composite propellers, made of a material known as micarta, were produced in the early 1920s [60]. Micarta (cotton duck-fabric impregnated with resin and cured) was an excellent material for propellers, however they were expensive and so were not as widely used as wood and metal propellers [16, p. 216]. Interest in composite propellers was revived in the 1960s and 1970s during the development of Vertical Take-Off and Landing (VTOL) aircraft, which required propellers that were capable of producing high amounts of thrust and were strong enough to cope with the high harmonic forces that the blades would experience when the propellers were transitioning from a vertical to a horizontal orientation [30, p. 254]. Composite propellers are not only used on VTOL

aircraft but on a large number of general aviation, business and transport aircraft, either as original equipment or as a retrofit propeller. Modern composite blades are typically either a covered-spar or monocoque design [30, p. 254].

Covered-spar blades use a steel or aluminum spar to carry most of the loads acting on the blade and a foam and composite shell as a fairing [30, p. 253]. This design does not use the composite shell as much more than a fairing and is only slightly lighter than a solid metal blade [30, p. 253] . More recent blades have used monocoque structures that use the composite skin to carry the blade loads. Monocoque propeller blades for an adjustable-pitch propeller are molded and then filled with a pour-in low-density foam, with a steel shank located at the blade's root [30, p. 254]. For fixed-pitch composite blades, composite pre-preg tape (strips of carbon fibre or fibreglass fabric impregnated with resin) is laid over wood or foam cores. The propeller is then placed in a mould and then cured in an autoclave.

Composite blades eliminate the shape constraints imposed by wood or metal, resulting in thinner and more efficient propellers and allow greater aerodynamic performance [61]. Custom composite propellers are available from a number of manufacturers for both manned and unmanned aircraft. While wood cores can be quickly manufactured using a CNC machine, laying the pre-preg tapes in the correct orientation on the cores would need to be completed manually. This process requires a significant amount of skill and time [62] and in production environments is now being performed by automatic tape placement (ATP) machines which are very expensive to procure.

Manufacturing composite components can also be a trial-and-error exercise, with an airworthy component not always being produced on the first attempt.

2.5.1.4 Reinforced Plastics

One of the largest manufacturers of propellers for SUAV and RC aircraft is APC Propellers, which produces injection-molded propellers made from a fiberglass-reinforced nylon [63]. While short chopped fibres are often added to polymers for improved mechanical properties [64, p. 242],APC instead uses relatively long fiberglass strands that remain orientated along the span of the blade during the molding process [63]. This provides a better load path to the hub, resulting in a stiffer propeller blade more capable of withstanding vibrations caused by the motor or engine or due to aeroelastic effects [63]

Reinforced plastics offer a high strength-to-weight ratio [64, p. 242] which is a very desirable quality for a material used for a propeller blade. However molding is not well-suited to producing small batches of custom propellers as each new design would require a mold to be manufactured. While small batches of molded propellers were successfully manufactured by Lorenz [34] and inexpensive molds can be produced using rapid prototyping [65], it would be preferable to produce a final component instead of a manufacturing tool.

2.5.2 Additive Manufacturing

2.5.2.1 Overview of Additive Manufacturing

Additive manufacturing is any rapid-prototyping process which creates a part through adding material incrementally [66, p. 581]. It is now synonymous with 3D

printing (3DP) [67], despite that 3D printing was originally considered an additive manufacturing technology [66, p. 583]. In this work, the term “3D printing” will be used when referring to any aspect of selective laser sintering (SLS) or fused-deposition modelling (FDM) manufacturing processes, and the term “additive manufacturing” will be used when referring to all additive manufacturing technologies.

Regardless of the name or process-specific details all additive manufacturing processes follow the same basic method, starting with spliting a three-dimensional model of the part into thin layers [66, p. 583]. For each layer, the rapid prototyping machine is provided with a path to follow while affixing a thin layer of material to the previous deposited layer [66, p. 583]. This process is repeated until the part is formed, after which it may be subjected to post-processing such as sanding or painting [66, p. 583].

Additive manufacturing offers a significant number of benefits, such as the ability to reduce the quantity of raw material required [67], the ability to produce usable parts from a CAD file in a matter of hours, and the ability to produce complex parts without the need for tooling. While in some cases the time savings may be small, additive manufacturing will reduce the touch time and labour costs associated with producing a part due to automation. It was found that producing a component at NASA in one of their machine shops took 81 hours and, had a FDM printer been used, it would have been completed in under 64 hours [68]. While this decrease in time is notable, the printed part

would have actually only needed 45 minutes of labour which would have resulted in a labour cost savings of over $3000 [68].

Additive manufacturing has a few drawbacks – it is ill suited to manufacturing large batches of a single part due to time needed for each part and high material costs, and the long-term performance of the parts produced is inferior to those made using conventional techniques [66, p. 594] . However, recent advances in terms of material and printer costs have made 3DP become a viable means for the low-volume production of a variety of components. Various 3DP processes have been used to successfully manufacture a wide range of parts, ranging from small consumer products (such as cellphone covers), medical devices (such as the Invisalign orthodontic aligners [66, p. 595]), tooling and molds, and large-scale prototypes and movie props (such as a 1/3-scale model of an Aston Martin DB5 for the James Bond film *Skyfall* [69])

2.5.2.2 Additive Manufacturing of Aerospace Components

Additive manufacturing is well-suited to the needs of the aerospace industry for several key reasons:

- Complex single components can be produced rather than a multiple parts which need to be assembled. In the case of a rocket injector nozzle designed and tested by NASA this resulted in a part reduction from 115 to 2 [70]
- Low-volume production of specialized components can be completed quickly and without expensive tooling [71]
- Wind tunnel models can be printed and assembled with comparable performance to the traditional metal ones in less time [72]

- One-off tooling can be quickly and economically manufactured, which is useful for aircraft restorations [71]

3DP has been used for SUAVs, with complete flying UAVs being produced [71] [73], and with some companies offering their services in 3DP UAV components [74]. The two 3DP methods often used to produce UAV components are Fusion Deposition Modelling (FDM) and Selective Laser Sintering (SLS) [71] [73] [74].

FDM printing uses a movable heated head extrude a thermoplastic filament, which is then applied as a 0.01" – 0.02" bead to the previous layer of the part [66, pp. 585-586]. The part is built up by the printer bed being slowly moved down as additional layers are added [66, p. 585]. Before printing the initial layer of the part or if the geometry of the part would require layers of material to be laid where there was none (i.e. a cone) the printer will print support material as well as the part. Support material is printed to be weaker and can be manually or chemically removed after printing [66, p. 585], either by breaking it off or dissolving it [75]. FDM printers are among the most inexpensive to the extent that the plans and software for one model, the RepRap printer, are open-source and available for free [76]. Commercial FDM printers are available (circa 2006) for between $30,000 and $150,000 [66, p. 586]. FDM printers typically use Acrylonitrile Butadiene Styrene (ABS) or Polylactic Acid (PLA) [77] and for aerospace applications, Ultem 9085 is widely used as it meets FAA flame regulations [71]. With regards to SUAVs, FDM is recommended for enclosures and lightly loaded components, such as winglets and ducting [74].

SLS printers use a guided laser beam to trace the shape of the part onto a thin layer of powder, causing the powder to become sintered together into a solid mass [66, p. 588]. Thin layers of powder are continually added using a roller until the finished part is produced [66, p. 588]. The powder may be non-metallic (nylon is often used [68, p. 2]) but also may be metallic [66, p. 588]. Typically if a metallic powder is used the process is referred to as Direct Metal Laser Sintering (DMLS) [78]. For improved part strength the powder may contain glass, carbon or ceramic particles [68]. SLS printers lack the simplicity of FDM printers and cost considerably more [79]. SLS printers are advertised as being suitable to manufacture nearly any UAV-related component [74].

The 3D printing process has been used to produce propellers that were operated for laboratory testing [80] [81] seemingly without failure. Stoll's propellers ([80]) were designed for testing under static conditions for the purpose of researching propeller noise and were printed from a glass-filled polyamide powder using SLS. Stoll noted the as-manufactured geometry of his blade was excellent, with only a slightly-rounded trailing edge. Epps et al designed and produced 3DP marine propellers as part of the MIT Remotely Operated Vehicle (ROV) Team [81]. These propellers were manufactured from ABS plastic with a coating of epoxy for added smoothness, but it was felt the blades lacked the required stiffness. An approach of using the blade as either a mold (to make a propeller from a more rigid material) or using a carbon- or glass- fibre skin was suggested.

In the context of the present research it was felt that 3DP would be a suitable method of manufacturing propellers for SUAVs, on the basis of demonstrations of 3DP and the overall advantages of additive manufacturing.

3 Chapter: Development of the Propeller Design Program

3.1 Introduction

Designing a propeller is an iterative process which, given the numerous iterative calculations that need to be performed, necessitates the use of a computer. Several propeller design programs exist and are freely available, such as QPROP and OpenProp.

QProp was created to analyze the performance of propeller-motor or windmill-generator combinations [82]. This program was later modified to become QMIL, which uses Larrabee's method to determine the chord and twist distribution of a propeller with a constant lift coefficient and minimum induced losses [83]. While determining the geometry of the blade due for aerodynamic efficiency is a key part of the process, it is only a small part of the design of a propeller. QMIL exports only the chord and twist distribution of the propeller as a text file, leaving the process of selecting a suitable airfoil for each blade station to the user. While a comprehensive process for using it for design purposes exists [84], QMIL cannot consider structural or manufacturing constraints while the blade is being designed.

OpenProp was created for the design of marine propellers and horizontal-axis turbines [85]. This does not allow it to be used for aircraft propellers as marine propellers are design using much different theories (these differences are beyond the scope of this work but a description of marine propeller design is available in [86]). OpenProp however was designed as a stand-alone program for marine propellers and contains modules for the shaping the propeller, analyzing its performance and structure, and exporting the shape of the propeller in such a way it can be interpreted by SolidWorks (a

3D CAD package) or for rapid prototyping [85]. OpenProp was found after much of the design program had been completed, but the considerable similarities between both programs suggests the adopted approach to propeller design is reasonable. It could be argued that ultimately a process for the design of any fluid-dynamic device – let it be a winglet for a business jet, a spoiler for a race car, or a rotor for a washing machine – would include the same steps.

To design a propeller suited to the aircraft and its mission, a program that uses a process consisting of the following steps was created:

- Accepting the constants provided by the user and analyzing the performance of the aircraft and its power plant
- Selecting the propeller's primary design condition, which is the phase of flight where peak propeller performance is the most important
- Sizing the propeller
- Using an iterative process to design an aerodynamically efficient and structurally airworthy propeller
- Producing the shape files need to recreate the propeller using a computer aided design (CAD) package and a design report with details of the propeller's expected aerodynamic and structural performance.

3.2 Design Constraints

The program requires the following input parameters from the user to be able to design an aircraft-specific propeller:

- Propeller size and speed constraints

- Aircraft performance data
- Power plant characteristics
- Airfoil family characteristics
- Integrated lift-coefficient condition
- Manufacturing method and limitations
- Material properties
- Methods of designing the blade

In each of the following sections, these required inputs are described in detail.

3.2.1 Propeller Size and Speed Constraints

The program requires the user to provide for the minimum and maximum propeller diameter, the number of blades, the diameter of the hub, and a maximum rated speed. The maximum rated speed of the propeller may not be the same as the maximum rotational speed of the motor as due to material properties and operational considerations (for example, aerobatic flight or testing a new material or manufacturing process) as it may not be deemed safe to attempt to run the propeller to that speed.

3.2.2 Aircraft Performance

The methods used for analyzing the performance of the aircraft are detailed in Appendix A. The performance of the aircraft is calculated using a Microsoft Excel spreadsheet rather than in the program's MATLAB code to allow the user to easily enter the aircraft's details and view the effects of changing performance requirements and

parameters, and if desired, change or adapt the methods of calculating the aircraft's performance.

The following speeds are calculated, assuming level flight and a user-defined typical wind conditions:

- Average take-off, or 70% of the rotation speed of the aircraft
- Best rate of climb
- Maximum endurance (loiter)
- Maximum range
- Design cruise speed
- Maximum level-flight speed (calculated as the dive speed of the aircraft)

The thrust needed to achieve these speeds in typical operating conditions, such as cruising in light winds or while performing gentle turns and climbs, is referred to as the normal required thrust (NRT). Additional thrust is required if the aircraft is to be able to manoeuver (climb or turn) or fly in strong winds or through thermal currents, both of which are a considerable factor at the low altitudes where many small UAVs operate. This extra amount of thrust is added to the normal required thrust for the maximum required thrust (MRT).

For each speed the user assigns a ranking as to the relative importance of efficient propeller operation in this phase of flight. One phase of flight must be given a ranking of 5, while each of the other phases need to be given a ranking of less than 5 but at least 0. The phase of flight and associated normal and maximum required thrust values are

considered the conditions that the propeller will be designed to meet and are referred to as the primary design conditions.

3.2.3 Powerplant Characteristics

While a propeller can be designed for peak efficiency at almost any advance ratio, the ability of the engine or motor to efficiently produce the required power is not guaranteed and needs to be checked. Most small UAVs are powered either by a gasoline engine or an electric motor. As electrically powered UAVs are more prevalent and better suited for low-noise and efficient flight, the program has been tailored to design electrically driven propellers. From a few basic details about a given electric motor, the program calculates the motor's ability to produce the required power and the motor's efficiency. The program estimates the optimal power output at a given shaft speed. A full description of the methods used to analyze a brushless direct-current motor and validation of these methods based on the manufacturer-provided test data can be found in Appendix B.

3.2.4 Airfoil Family

As described in section 2.3.3.2 (Airfoil Data) ,the program interpolates the necessary values from a series of look-up tables detailing the aerodynamic characteristics – the drag polar, lift-curve slope, and the critical Mach number – lift coefficient plot. – of several airfoils for a given family. Airfoil data can be imported from [44], using XFOIL, or provided by the user. The program will design the propeller by selecting at each blade

station an airfoil with a thickness-chord ratio between the minimum and maximum found in the look-up tables.

3.2.5 Lift Coefficient Conditions

The lift coefficient condition is determined by the user to govern how the program selects the ideal lift coefficient when designing a blade station with a given airfoil. If a blade station cannot be designed at the ideal lift coefficient (due to structural or geometric reasons), the lift coefficient is decreased to increase the blade's chord until an acceptable blade station is produced. Three lift coefficient conditions are available:

Maximum lift-to-drag ratio: If this condition is set, the program will attempt to design a blade section using the lift coefficient corresponding to the airfoil's maximum lift-to-drag ratio. The propeller will be the most efficient at its primary design point as the propeller is generating the most thrust for the least amount of power. However, designing a fixed-pitch propeller such that the blade's airfoils are at their maximum lift-to-drag ratio for a single given rotational and forward flight speed may result in poor performance in off-design conditions. For some airfoil families (such as most NACA 4-digit airfoils) the maximum lift-to-drag ratio occurs at a high lift-coefficient, which may lead to blade stall when operating in off-design conditions.

Minimum drag coefficient: If this condition is set, the program will attempt to design a blade section with the lift coefficient for the airfoil's minimum profile drag coefficient, which for airfoils is considered the design lift coefficient [41]. This condition is preferable for NACA 6-series airfoils that have a clearly-defined drag bucket with the lowest drag coefficient near the airfoil's design lift coefficient. This condition can be

used for NACA 4-digit airfoils; however, with thicker airfoils the minimum C_D occurs at low lift coefficients.

Fixed lift coefficient: With this condition the program will attempt to design the blade section with the airfoil operating at a fixed user-set lift coefficient for a given Mach and Reynolds number. If the user is unsatisfied with the lift-coefficients selected by the program, this condition is primarily offered as an "over-ride" that will force the program to design a propeller at a given lift coefficient. It was also found that fixed lift coefficients work well with most NACA 4-digit airfoils and this condition is recommended when designing for this airfoil.

Separate functions in MATLAB were written to determine lift and drag coefficients at a given Mach and Reynolds number for each lift coefficient condition. These functions determine the lift and drag coefficients for a given airfoil by interpolating tabulated aerodynamic data for a family of airfoils and using a low-Reynolds number correction (if necessary and if enabled by the user). It then corrects the lift-coefficient for compressibility effects at the blade station.

3.2.6 Manufacturing Method and Material Properties

To ensure that the blade can be manufactured as intended the user must define the minimum wall thickness (the minimum thickness of any part of the blade) and the minimum blade thickness (the cross-sectional thickness of the blade at its thickest point). If a Fused Deposition Modeling (FDM) 3D printer is being used, both of these thicknesses should be a suitable multiple of the deposited layer thickness based on the capabilities of the chosen FDM printer. In addition, if a FDM printer is being used a

trailing-edge correction feature is available to force the trailing edge of the blade to be at least the minimum wall thickness capable of being printed. This also allows the code to be adapted to future improved 3D printer capabilities as manufacturing processes improve.

Material information is provided to the program through a Microsoft Excel spreadsheet. The list of material properties in the spreadsheet was based on those for an entry in the US Military Handbook 5 (MIL-HDBK-5), a standard reference for the properties of metals used in aircraft structures[4], and with some additional polymer-specific properties added.

3.2.7 Methods of Blade Design

A description of the methods of designing the blade is better suited for discussion as part of the detailed blade design section.

3.3 Initial Propeller Sizing

The first step in the process of designing a propeller is to determine the number of blades and propeller diameter. It may also be necessary, depending on the lift-coefficient condition selected by the user, to select a lift coefficient for the blade. These variables are selected by estimating the performance of propellers using all allowable combinations propeller diameter, number of blades (and if required, lift coefficients) to select the

[4] MIL-HDBK-5 has been superseded by the Metal Material Property Data Sheets (MMPDS). However MIL-HDBK-5, unlike the MMPDS, is widely available on the internet free-of-charge. As MIL-HDBK 5 entries are readily found in many texts on aircraft structures the format of it is much more widely known than that of MMPDS.

combination that best produces the required normal thrust. As each combination must be evaluated over the full range of rotational speeds, this process can involve thousands of performance estimates. A single-point performance estimate method is used during the initial blade sizing as it can quickly estimate the propeller's performance with a minimal amount of detail. This allows for the determination of the approximate geometry of the propeller blade and to evaluate the propeller's performance over the full flight envelope.

3.3.1 Single-Point Performance Method

Single-point performance methods assume that the performance of the entire propeller can be predicted based on the average lift and drag coefficient for a blade ($\overline{C_l}$ and $\overline{C_d}$) and a chord length (c/R) based on the blade activity factor (a measure of the solidity, or area, of the blade) [15, p. 314], As the average lift coefficient and chord length are typically close to those at 75% of the propeller blade radius, the characteristics of the blade at this station are used.

From McCormick, the thrust co-efficient C_T and power coefficient C_P of the propeller can be estimated as [15, p. 314]:

$$C_T = \frac{\pi^3 \sigma_m}{8} \overline{C_l} f(\lambda) \quad \textbf{Eq. 19}$$

$$C_P = C_T J + 1.12 \frac{C_T}{2} \left[-J + \left(J^2 + \frac{\pi C_T}{8} \right)^{1/2} \right] + \frac{\pi^4 \sigma_m}{8} \overline{C_d}\, g(\lambda) \quad \textbf{Eq. 20}$$

Where:

$$\sigma_m = \frac{Bc}{\pi R} \quad \textbf{Eq. 21}$$

$$\lambda = \frac{V}{\omega R} \quad \textbf{Eq. 22}$$

$$f(\lambda) = \int_{x_h}^{1} x(\lambda^2 + x^2)^{1/2} dx \quad \textbf{Eq. 23}$$

$$g(\lambda) = \int_{x_h}^{1} x^2(\lambda^2 + x^2)^{1/2} dx \quad \textbf{Eq. 24}$$

Based on Theodorsen's theory of propeller design, the product of the solidity of the blade and lift co-efficient of the blade, σC_L, is [27]:

$$\sigma C_L = \frac{1 + \bar{w}}{\left(1 + {}^1/_2\,\bar{w}\right)\left(1 + {}^1/_2\,\bar{w}cos^2\phi\right)} 2\bar{w}\kappa \frac{sin^2\phi}{\cos\phi} \quad \textbf{Eq. 25}$$

Where:

$$\phi = \text{atan}\left(\frac{V + {}^1/_2\,w}{2\pi r n}\right) \quad \textbf{Eq. 26}$$

$$\bar{w} = \frac{w}{V} \quad \textbf{Eq. 27}$$

It should be noted that McCormick defines propeller solidity differently than in most other works [27] [33], where solidity is defined as:

$$\sigma = \frac{Bc}{\pi x D} = \frac{Bc}{2\pi x R} \quad \textbf{Eq. 28}$$

McCormick actually uses the definition of rotor solidity, or the solidity of a helicopter rotor [88, pp. 3-4]) instead of propeller solidity. Rotor solidity neglects the radial

location of the blade chord, as the chord of a helicopter rotor blade does not typically vary along the span of the blade. While propellers with a constant chord have been produced (such as the A6441FN-606 propeller from the Aeroproducts Company used on the Lockheed L-188 and Convair 580), a constant-chord assumption is not valid for all propellers. In addition, the use of rotor solidity rather than propeller solidity would contradict currently accepted convention

$$C_T = \frac{\pi^3 x \sigma C_l}{4} f(\lambda) \qquad \textbf{Eq. 29}$$

$$C_P = C_T J + 1.12 \frac{C_T}{2} \left[-J + \left(J^2 + \frac{\pi C_T}{8} \right)^{\frac{1}{2}} \right] + \frac{\pi^4 x \sigma}{4} C_d \, g(\lambda) \qquad \textbf{Eq. 30}$$

The values C_L and C_D are calculated with an airfoil that has a thickness-chord ratio at approximately 1/3 of the range of thickness-chord *(t/c)* ratios associated with the aerodynamic data for the airfoil family. For example, if aerodynamic data is available for airfoils with a t/c ratio between 6% and 24%, the aerodynamic characteristics of a 12% thick airfoil will be used. The 1/3 rule was selected after a brief examination of the geometry of typical readily available RC propellers. This showed that the thickness at the 75% station was roughly 1/3 the range of the t/c ratios at the tip and near the root of the blade. While the effects of compressible flow on the lift coefficient can be considered as the Mach number at any blade station and can be easily calculated, the effect of the Reynolds number cannot be assessed accurately until the chord length of blade station is known. For the purposes of the single-point method, the lift and drag coefficients are evaluated at a Reynolds number based on the Mach number at the blade station and the

chord length that would result from the blade having a cross-sectional thickness twice the minimum allowed.

To calculate σC_L the induced velocity (*w)* that is necessary to produce the normal required thrust at the primary design point must be determined. This is calculated through an iterative process using a bisectional search routine to increase or decrease the induced velocity until the desired thrust coefficient is achieved. This bisectional search requires an initial minimum and maximum induced velocity to be first selected. To minimize the number of iterations needed it is desirable that these be close to the final value, which is the only valid solution. A standard method and small-propeller method are available for generating the initial minimum and maximum induced velocities.

Standard Method: The standard method sets the initial minimum and maximum induced velocity for the bisectional search by assuming it is the increase in air speed through the propeller disc needed to produce the normal required thrust when stationary and when the aircraft is at its maximum speed. The actual required induced velocity is higher than estimated for both these conditions as this assumption neglects the profile drag of the blades [15, p. 296]. However the drag-less blades assumption simplifies calculations and the (small) difference between the estimated and actual induced velocity is irrelevant for the purposes of the bisectional search where it is only assumed the actual induced velocity is somewhere between the maximum and minimum.

The maximum induced velocity occurs when the propeller is operating under static conditions (there is no forward flight speed) [15, p. 295].

$$w_o = \sqrt{\frac{T}{2\rho A}} \qquad \textbf{Eq. 31}$$

This value is considered for the bisectional search as the maximum induced velocity, or w_{max}.

As the forward speed of the aircraft (propeller) increases less induced velocity is necessary to achieve the desired thrust. For this case the induced velocity required is [15, p. 296]

$$w = \frac{1}{2}\left[-V_o + \sqrt{{V_o}^2 + \left(\frac{2T}{\rho A}\right)}\right] \qquad \textbf{Eq. 32}$$

Small-Propeller Method: Using the standard method for designing small propellers (less than ~14" in diameter) or operating at low flight speeds will result in the sizing program attempting to make a propeller that produces the normal required thrust at low-rotational speeds by using a large induced velocity. A large induced velocity will cause the pitch of the blade to be very high and lead to a relatively wide blade planform, which may generate large centrifugal forces that cannot be withstood by the blade root. As the pitch of a small propeller is rarely greater than its diameter [10], the small-propeller method uses a user-define maximum pitch-diameter ratio to set the upper limit of induced velocity.

The pitch of a propeller at a given blade station is [15, p. 306]:

$$p = 2\pi \tan\beta \qquad \textbf{Eq. 33}$$

Rearranging for β

$$\beta = tan\left(\frac{p}{\pi Dx}\right)$$ **Eq. 34**

As seen in Figure 2 the blade angle is the combination of the angle of the relative wind, φ, and the angle of attack, α. If the section lift coefficient is known, α can be easily determined (from the lookup tables) for a given airfoil. Therefore,

$$\phi = \beta - \alpha = \text{atan}\left(\frac{V + {}^{1}/_{2}\, w}{xR\omega_R}\right)$$ **Eq. 35**

Rearranging,

$$w = 2(\tan(\beta - \alpha)\, xR\omega_R - V)$$ **Eq. 36**

If the small propeller method is used, w_{min} is taken to as 25% of w_{max}.

At each rotational speed, the thrust coefficient corresponding to a σC_L for w_{min} and w_{max} is calculated. If these induced velocities do not produce thrust (respectively) less-than and greater-than the normal required thrust, the normal required thrust at the design point is not possible.

Once the solidity of the blade has been determined, the propeller's power coefficient is estimated and the cross-sectional thickness is calculated. If the thickness of the blade is below the minimum allowable limit and the efficiency of the propeller is less than 60%, the combination is considered poor and no further analysis is performed and the rotational speed of the propeller is increased.

Overall efficiency is the combined efficiency of the motor or engine and the propeller. As the goal of the propulsion system is to turn fuel or electrical energy into thrust in the most efficient manner, the overall efficiency is considered rather than just

the efficiency of the propeller. For a brushless DC motor, neglecting thermal effects this is equal to:

$$\eta_{overall} = \frac{power\ produced}{electrical\ powersupplied} \qquad \textbf{Eq. 37}$$

$$= \frac{thrust \times velocity}{terminal\ voltage\ \times supply\ current}$$

$$= \frac{C_T \rho \left(\frac{N}{60}\right)^2 D^4 V}{\left[\left(\frac{N}{K_V}\right) + R\left[\left(\frac{Q_{prop}}{k_t}\right) + I_o\right]\right]\left[\left(\frac{T_{prop}}{k_t}\right) + I_o\right]}$$

Where:

$$Q_{prop} = \frac{C_P \rho N^2 D^5}{2\pi(60^2)} \qquad \textbf{Eq. 38}$$

If the overall efficiency is the highest for the current diameter-blade-lift coefficient combination, the speed and details of the analysis are retained and the single-point sizing method is repeated with it for an incrementally higher rotational speed. Once all diameter-blade-lift coefficient combinations have been assessed, they are scored to select which will be used for the propeller.

3.3.2 Scoring Process

The scoring process is used to select the propeller diameter-blade-lift coefficient combination that will best allow the aircraft to perform the mission detailed by the user. The scoring process uses the single-point performance method to check the propeller's overall efficiency and that, for all phases of flight; the propeller will generate the normal and maximum required thrust needed. The overall efficiency of the propeller when producing the normal required thrust is multiplied by a weight factor defined by the user

to reflect the relative importance of efficient propeller performance in that phase of flight. The sum of the weighted efficiencies, referred to as the efficiency score, is used to help the program select the best diameter-blade-lift coefficient combination; however, this is not the only factor. In order of importance, the other factors are:

1) Meeting the normal required thrust – The program will select a propeller that can produce the normal required thrust for as many phases of flight as is possible. This is the most critical factor as without this minimum amount of thrust the aircraft will have no chance of successfully completing its mission;
2) Meeting the maximum required thrust – This requirement is secondary as the mission can still be performed without it, but there will be some limitations on the aircraft's performance; and
3) Highest efficiency score – The highest efficiency score should reflect that the propeller is more efficient in critical phases of flight.

The program will select a propeller that can perform the basic mission (produce the normal required thrust in all phases of flight) at the expense of efficiency or maximum thrust. For example, a propeller that performs the basic mission but will never produce the maximum required thrust for any phase of flight will be selected over a propeller that meets both the normal and maximum required thrust in a few phases. The efficiency score is used to differentiate between propellers of equal thrust-producing ability.

3.4 Detailed Propeller Blade Design

Once the diameter, number of blades and the lift coefficient condition have been selected, the propeller blades themselves are designed. The blade design routine uses Theodorsen's theory of propeller design [27] and the strip-analysis method described in [17].The blade design routine can be considered as a more advanced version of the preliminary sizing routine. As with the sizing routine, the propeller is designed (or sized) for a now smaller range of speeds, and the induced velocity is varied until either the thrust coefficient (or alternatively, a power coefficient) is met. However, the blade design routine, also considers the use of different airfoils at each station. It checks the strength of the blade and evaluates the necessary sweep and flutter speed of each section of the blade.

The blade design routine allows the user to select the conditions for how the blade is designed. These options exist to increase the robustness of the program and allow for it to better design a propeller blade for any operating condition.

3.4.1 Optimum Blade Loading Conditions

The design program can use either a Betz's theory or the calculation of variations approach, both of which were described in 2.3.2.2

Using the calculus of variations method, if the solidity and loading of the blade are allowed to vary, the induced velocity at any station of the blade is [33, p. 170]

$$\bar{w} = V\left(-\zeta - \frac{\tan\gamma}{J/\pi x}\left[\zeta + 1 + \left(\frac{J}{\pi x}\right)^2\right]\right) \quad \textbf{Eq. 39}$$

Where $\gamma = tan^{-1}\left(\frac{C_D}{C_L}\right)$ and ζ is an arbitrary constant chosen to obtain the desired power or thrust coefficient [17, p. 167]. This equation does not hold if the solidity is not allowed to vary. The program will never force a given blade solidity (by fixing the chord length) changing the solidity instead by altering the lift coefficient.

Many propellers made for radio-controlled hobby aircraft are designed with the geometric pitch of the blade constant or near constant. If the lift coefficient is held constant for the full span of a constant-pitch propeller blade, the angle of attack of the airfoil is then fixed and the angle of the relative wind (and the induced velocity) will vary. This is problematic for this program as the lift-coefficient conditions used that attempt to force the airfoil of the blade to have a fixed lift coefficient. For this reason there is no fixed pitch mode currently offered.

The differences between the induced velocity distribution obtained using the Betz and calculus of variations methods will depend on the advance ratio and lift and drag-coefficients. To examine the differences between these distributions and investigate the induced velocity distribution of a constant-pitch propeller with a constant lift co-efficient, the scenario of a UAV flying at 50kts and needing at least 7 pounds of thrust was considered. The 17x12 propeller from APC is a suitable commercially available propeller that produces 32.79 N of thrust at 7000 RPM at 50 kts [89]. Using the equation from the single-point performance method and with the propeller's performance data and geometry, [90], the average lift coefficient of the propeller blade at this operating

condition was determined to be 0.67. Assuming the airfoil used for the blade has the same aerodynamic properties as a NACA 4412 (similar to the airfoil APC uses [40]) and at a Reynolds number of 167,370, the profile drag coefficient of this airfoil is 0.023 [46] and the angle of attack is 2.25 degrees [44]. From Eq. 21 the reference non-dimensional induced velocity, $\bar{w}_{ref}$, was found to be 0.3533. Using this value and rearranging Eq. 39, ζ = -0.4486. For the constant-pitch propeller a pitch-diameter ratio of 12/17 (pitch of 12", diameter of 17") was used to calculate the blade angle at each station, and by using the angle of attack and from Eq. 36 rearranged to be a function of the advance ratio, $\bar{w}$ at each station is calculated. To allow for easier comparison between the differences for each distribution, the $\bar{w}$ at each station is divided by $\bar{w}_{ref}$ or 0.3533.

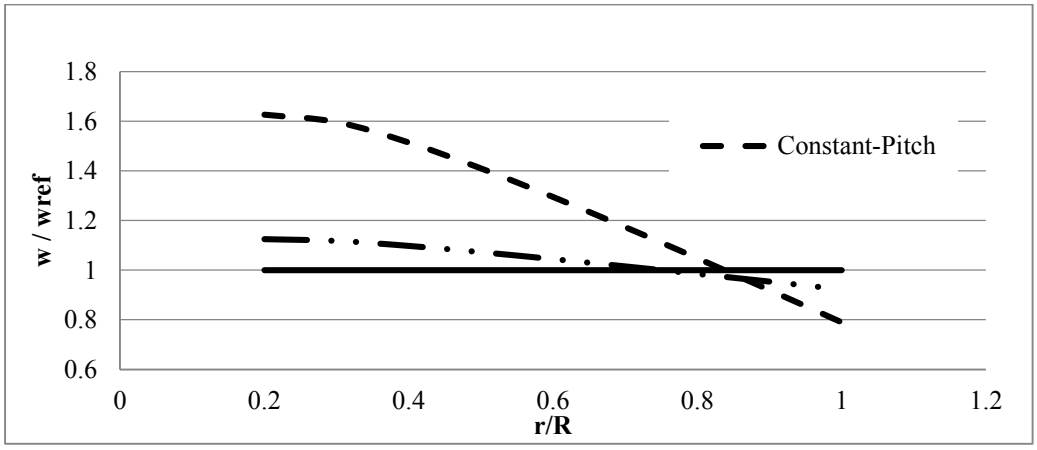

Figure 9 Non-Dimensional Velocity Distribution for different blade-load distributions

From Figure 9 it can be seen that there is a small difference between the $\bar{w}$ distribution produced by the Betz and calculus of variations methods, and that the $\bar{w}$ distribution for a constant-pitch blade (assuming a constant angle of attack) is close to neither. For the calculus of variation distribution, the change in $\bar{w}$ over the span of the

blade is very small. As the drag coefficient decreases the span-wise variation of $\overline{w}$ will also decrease. If the drag coefficient of the blade was zero there would be no difference at all. As might be expected, there is a substantial variation in the $\overline{w}$ distribution over the span of the constant-pitch propeller blade if the lift coefficient is held constant and is not close to either of the optimum distributions. While this may raise questions as to why a propeller manufacturer would use such a distribution, the actual pitch distribution of the APC 17x12 propeller shown in is not constant and shows no similarity with any of the distributions examined. It has been reportedly found that few propellers of the over 200 measured had the "advertised" geometric pitch [58]. The large change near the root of the blade is likely due to the need to smoothly transition the blade into hub. As APC tends to use airfoils with a high thickness-chord ratio near the root that do not effectively produce thrust, there is no benefit to design this section of the blade for optimal blade loading. The pitch variation for the rest of the blade is likely to produce a more optimal lift distribution.

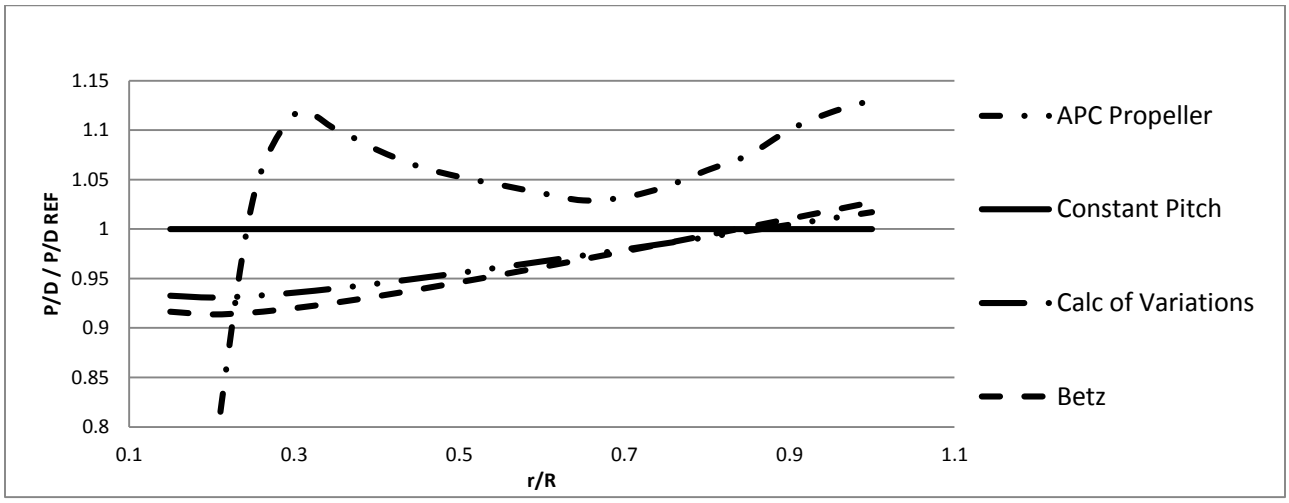

Figure 10 Geometric Pitch/Diameter Distributions

Using either the Betz or Calculus of Variations method does not change the blade sizing process, other than that ζ is used for the bisectional search and the induced velocity is calculated in a separate step. However, it was found that the program is not always able to design a unique blade every time ζ is changed, and as a result the thrust or power coefficient may never converge. The reason for this was not determined conclusively, but it was noted that the outer portion of the blade was not changing as ζ was varied. It was decided to allow the user to select if the either the Betz or variation of calculus method is used. Regardless of the selected method, ζ is calculated for each blade station and is made available to the user. The values of ζ at each blade station can be used as a measure as to how optimized the blade is for a given operating condition, with less variation suggesting the blade makes better use of the power provided to it

3.4.2 Thrust Coefficient and Power Coefficient Modes

As mentioned previously, the widespread use of electric motors on small UAVs allows for propellers to be designed to operate at any given rotational speed, as the power output is flexible and the necessary torque can be obtained by controlling the current supplied to the motor. However, if the propeller is designed for a gas engine, the power output is not flexible and the amount of power provided to the propeller would determine the amount of thrust produced. Electric motors have optimum power output (power produced with the best efficiency) for a given rotational speed, within their rated operating limits and it may be desirable to design the propeller to absorb this amount of

power[5]. To allow for a propeller designed for either a flexible or fixed power output at a given speed, the program has both a thrust coefficient (CT mode) and power coefficient (CP mode). In CT mode the program changes the induced velocity or ζ to obtain a given thrust coefficient, and then checks that the motor can provide the necessary power. In CP mode the program alters the induced velocity or ζ to obtain a given power coefficient, and checks if the propeller produces the required thrust. If the required thrust is not produced, the rotational speed is increased which leads to the propeller producing more thrust.

3.4.3 Blade Design

Designing a propeller involves changing induced velocity or λ to obtain a given thrust coefficient, and with each change comes the need to size each of the blade stations (or points along the span of the blade). Sizing the station involves determining the chord length, lift-coefficient, blade angle and many other details, all of which are dependent on the airfoil. To select the best airfoil, the station is designed with each available airfoil. The station airfoil that offers the best performance while meeting the intent of the lift coefficient condition is selected for the station. While this approach is complete it is also time consuming due to the number of calculations required and inefficient due to the number of blade stations that are designed but rejected. To make this process quicker, the sizing routine uses a series of checks to stop the analysis of the airfoil at its current lift coefficient when it detects that the airfoil will be unacceptable for the station.

---

[5] It was found after this work was performed that a similar argument for matching a propeller to a motor and aircraft was presented by Drela in [120]

At each blade station, limitations are set on the allowable blade thickness, sweep, and chord length. This ensures that the blade can be manufactured and avoids impossible or unwanted features (such as a the blade becoming very thin or having a wide chord at the root but narrow and thicker at the tip)

For each airfoil, an initial lift coefficient is calculated based on the lift coefficient condition and the chord length of the blade is calculated following the strip-analysis procedure described in [17](details are available in Appendix C). From the chord length of the blade the thickness and cross-sectional area, which is used to quickly check the strength of the blade, can be determined.

The largest force acting on the blade is the centrifugal force that acts radially on the blade and results in primarily a tensile stress in the blade. Knowing the cumulative centrifugal force at a particular blade station and the tensile yield stress of the material, the minimum cross-sectional area is, as derived in appendix C;

$$A = \frac{CF_{accum}}{\left(\frac{\sigma_{sy}}{N}\right) - \rho\delta x R^2\left(\sqrt{2}\omega_{\text{max.rated}}\right)^2} \quad \textbf{Eq. 40}$$

If the chord is between the minimum and maximum limits and the thickness and cross-sectional area meet the geometry and structural constraints, the blade sizing process continues. If the thickness or chord length is too low the lift coefficient is decreased and the process is attempted again. If the chord length is over the limit, the lift coefficient is not increased to reduce the chord and instead the airfoil is deemed unacceptable.

Once the airfoil has passed this rudimentary analysis, it is subjected to a more detailed structural analysis, the blade sweep and the blade is checked to ensure when

manufactured it will remain aerodynamically acceptable. The structural check will always be performed but all of the other checks can be disabled. If the blade fails any of the checks, the blade station created with the airfoil at its present lift coefficient is deemed to be an invalid solution. The sizing process is stopped and the lift coefficient is reduced by the program by 0.01. When all checks have been passed, the created blade station is considered to be a valid solution. The solution is saved for comparison and sizing with the next airfoil is attempted.

3.4.4 Simplified Blade Structural Analysis

It would be impossible to produce a safe efficient propeller for any aircraft without thoroughly analyzing its strength. Propeller blades are highly stressed but cannot be built with greater margins of safety through the use of additional material due to the negative effect that the additional material would have on the blade's centrifugal force [18, p. 63]. Therefore, the loads applied to propeller blades and their effects need to be better understood under all operating conditions [18, p. 63] .

When initially sizing the blade the detailed structural analysis methods described in 3.6 are impractical as they require the planform and thickness of the full blade to be known. Instead, a much simpler analysis is used but with very conservative load conditions. It is assumed that the airfoil is at its maximum lift coefficient (and corresponding drag coefficient), the rotational speed is that which would generate twice the centrifugal force at the maximum allowable rotational speed, and the aircraft is

travelling at its maximum flight speed. This scenario produces the highest possible forces that the blade would ever be subjected to in operation.

Both the aerodynamic and mass loads are calculated using a strip method where each force or moment is calculated on a small strip of the blade or blade element. From these elemental forces the cumulative force or moment at any given station on the blade can be determined.

The stresses at any blade station are equal to the combination of the tensile stress due to centrifugal loading and the tensile and compressive stress (depending on which face the stresses are being calculated at). This can be expressed as [30, p. 126]:

$$\sigma_N = \frac{\sum CF_N}{A} \pm \frac{M_{thrust} y}{I_{min}} \qquad \textbf{Eq. 41}$$

Where:

$\sum \boldsymbol{CF_N}$ = the cumulative centrifugal force acting at a blade station N

A = cross-sectional area

M_{thrust} = bending moment due to the thrust of the blade

y = distance from the section's neutral axis to the surface of the blade

I = minimum second moment of inertia of the blade

The centrifugal force can be assumed to act at the centre of gravity of each blade element and can be calculated with the equation [30, p. 80]

$$\Delta CF = \Delta m \bar{r} \omega^2 \quad \textbf{Eq. 42}$$

Where:

ΔCF = centrifugal force of the blade element

$\bar{r}$ = distance from the axis of rotation to the centre of the blade element

ω = rotational speed of the propeller [radians/second]

Δm = mass of the blade element, which can be expressed as [30, p. 80]:

$$\Delta m = \rho A \Delta r \quad \textbf{Eq. 43}$$

Where:

ρ = material density

A = cross-sectional area of the blade at the centre of the element

Δ r = the width of the element

As per FAR 35.35, the rotational speed is calculated as 144% of the maximum rated (or possible) speed of the propeller.

The centrifugal force acting on any blade station along the span of the propeller is the sum of the centrifugal force acting on the portion of the blade away from the station of interest to the tip of the blade:

$$CF = \rho \omega^2 \int_r^R Ar \, dr \quad \textbf{Eq. 44}$$

Using the strip method, the centrifugal force at the element blade of element *N* can be calculated as:

$$CF_N = \frac{1}{2}\Delta CF_N + \sum_{N-1}^{Ntip} \Delta CF \quad \textbf{Eq. 45}$$

The lift and drag generated by an airfoil acts perpendicular to each other, with the lift force acting more-or-less perpendicular to the chord line of the airfoil. The lift and drag force acting on any blade element are calculated as [30, p. 75]:

$$\Delta L = \frac{1}{2}\rho W^2 C_L b \Delta r \quad \textbf{Eq. 46}$$

$$\Delta D = \frac{1}{2}\rho W^2 C_D b \Delta r \quad \textbf{Eq. 47}$$

Where:

ΔL, ΔD = the elemental lift and drag forces

ρ= air density [kg/m^3]

C_L, C_D = lift and drag coefficient

b = average chord of element [m]

Δr = width of element [m]

The twisted-shape of a propeller complicates the calculation of the bending moment due to lift and drag forces as their direction, relative to the y-axis as shown in figure PJAD, changes over the span of the blade. To account for this the lift and drag forces are resolved into the thrust and torque directions using the inflow angle, ϕ:

$$F_Y = \Delta L\, cos\phi - \Delta D\, sin\phi \quad \textbf{Eq. 48}$$

$$F_Z = \Delta D cos\phi + \Delta L\, sin\phi \quad \textbf{Eq. 49}$$

Assuming that F_z is much smaller than F_y and can be safely neglected, the bending moment at any blade station from the thrust of outward stations can be calculated as:

$$M_{Thrust} = \sum_{N}^{N_{tip}} F_y R(x - x_N) \quad \textbf{Eq. 50}$$

where:

F_y = the thrust force of a given strip

$(x - x_N)$ = the difference between the radial position of a station the moment if being calculated around, x_N, and the radial position of the station of the contributing thrust force.

The geometric properties of the blade (such as A, I_{min}, and y) at a given blade station are determined using a polygon method described in [91, pp. 603-606] and in [80, pp. 41-42]. This polygon method is only practical with a computer due to the large volume of calculations that need to be performed, and is still computationally expensive to frequently repeat. Prior to use of this method non-dimensional coefficients listed in [16] [18] [30] were used to determine the airfoil's geometric properties. For example, the area airfoil can be expressed as:

$$A = K_{area} bh \quad \textbf{Eq. 51}$$

Where:

K_{area} = a constant specific to the airfoil

b = chord length of airfoil

h = thickness of the airfoil

This method allows for the properties of an airfoil to be determined quickly, however the coefficients are not always available for all airfoil families. To overcome this difficulty the polygon method is used to determine all of the geometric scaling coefficients when the program is started for the selected airfoils and stores them in a look-up table, allowing for them to be quickly referred to as necessary.

The stresses in the blade are evaluated at both the upper and lower surfaces of the blade and are compared to the yield tensile and compressive stresses for the material. If either had a margin of safety less than 0.5, no further analysis is performed until the blade chord is increased.

3.4.5 Sweep at Speed

The "sweep at speed" function calculates the sweep required to avoid the Mach number at the station from exceeding the airfoil's critical Mach number (M_{crit}). The value M_{crit} is the lowest free-stream Mach number that the local air speed at a point on the surface of the airfoil will become supersonic [15, p. 212]. When this occurs, the airfoil's drag will begin to rise due to compressibility effects, which will result in more power being required and the propeller's efficiency decreasing. The speed at the surface of the airfoil is dependent on the pressure distribution that changes with the angle of attack of the airfoil. As the lift coefficient is also based on the pressure distribution, M_{crit} is often

presented as a function of the low-speed lift coefficient. Many NACA-designed airfoils M_{crit} – lift coefficient plots can be found [44].

The highest station Mach number will be achieved when both the aircraft is at its dive speed and the propeller is spinning at its maximum rated rotational speed. However, since for a fixed-pitch propeller the blade angle is constant, the lift coefficient of the airfoil changes based on the angle of the relative wind, which is dependent on the rotational and forward flight speed. The program calculates the lift coefficient at the blade station a number of points over the range of rotational speeds and checks that the critical Mach number is greater than the station Mach number. If it is not, the blade can be swept to reduce the Mach number "seen" by the airfoil so that only a component of the oncoming air travels over the airfoil. The sweep is calculated as:

$$\Lambda = cos^{-1}\left(\frac{M_{crit}}{M_{stn}}\right) \quad \textbf{Eq. 52}$$

The largest leading-edge sweep required for the airfoil is retained. If the sweep of the airfoil is greater than allowed no further analysis is performed until the section lift coefficient is decreased.

3.4.6 Trailing Edge Correction

The purpose of the trailing edge correction check is to determine the fraction of the chord length of the blade that would require additional layers of printed material to achieve the minimum wall thickness that can be reliably manufactured. Ideally, the trailing edge of an airfoil would smoothly transition to a knife-edge thickness. This can be obtained for moulded or machined propeller blades if desired with little difficulty if there is sufficient material present to allow reshaping. FDM-type printers, can only

produce parts in discrete thicknesses (multiples of the layer thickness) which makes printing a sharp trailing edge difficult. The printer will print as close to the shape of the propeller as possible but the trailing edge may look "hairy" (Figure 11) or have a saw-tooth edge (Figure 12), depending on the size of the blade and layer thickness. In the case of a hairy propeller, the trailing edge can be sanded to obtain a smooth edge, however this will alter the blade platform slightly and will affect the mass and aerodynamic balance of the blade. These changes are minor, and the blade can be re-balanced as necessary. For a saw-tooth trailing edge, however, the imperfection of the trailing edge cannot be corrected through sanding as the material removed would significantly alter the shape of the blade.

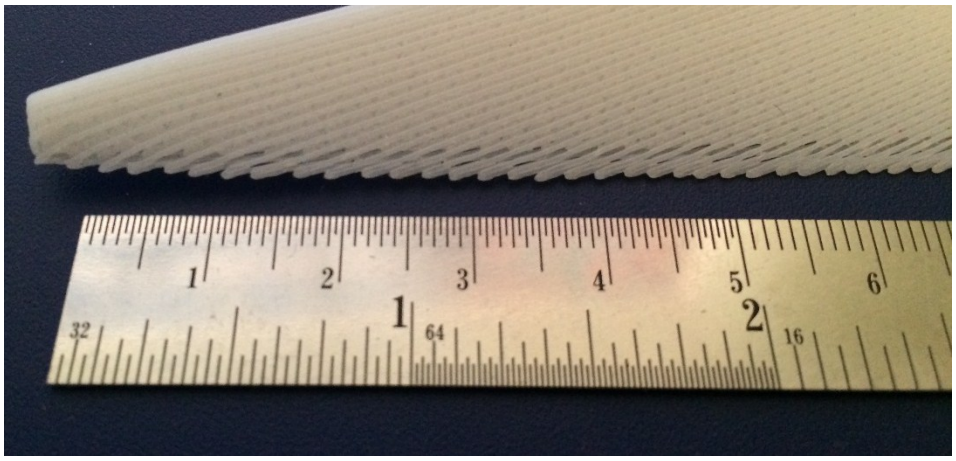

Figure 11 A "hairy" trailing edge

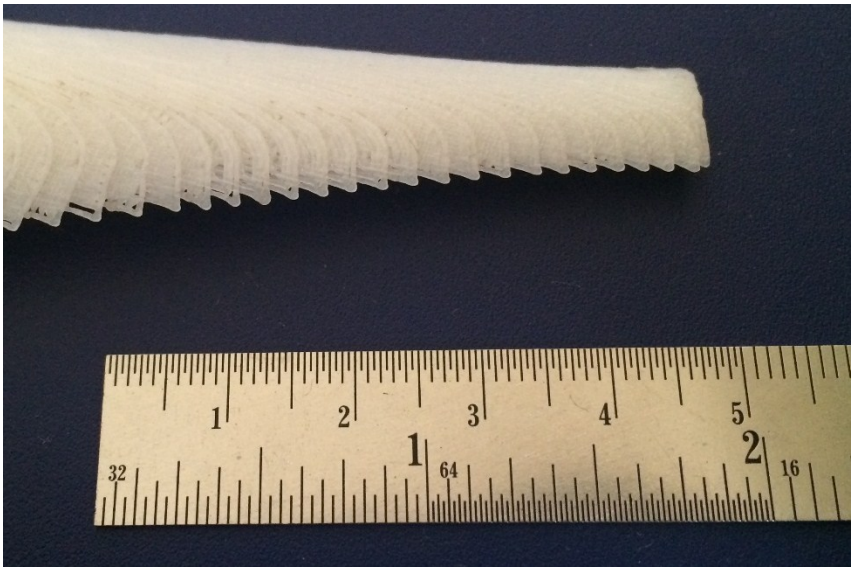

Figure 12 A "saw tooth" trailing edge

To ensure a smooth trailing edge, additional layers of printed material are added to either side of the camber line of the blade. In addition, the slope of the trailing edge of the blade was considered to avoid insufficient layers being affixed. Test blades manufactured using the correction were near-flawless (Figure 13), with only a pinhole void on a particularly curved section of the blade

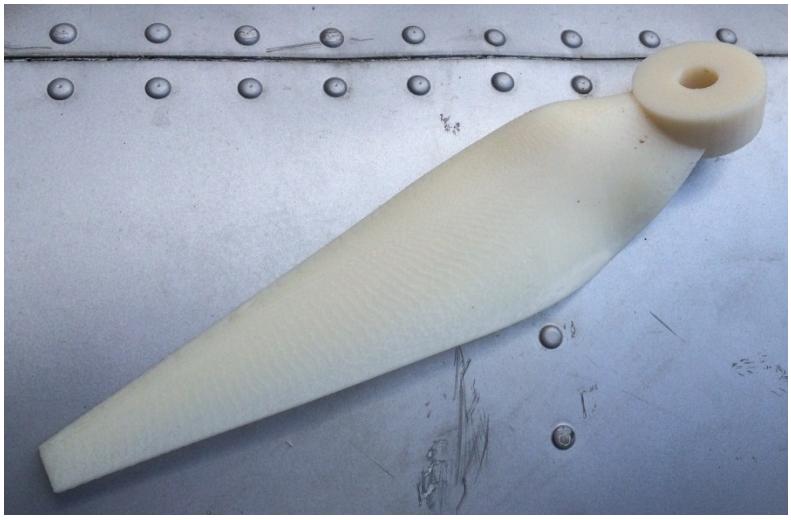

Figure 13 Blade printed with the trailing edge correction successfully applied

To avoid altering a large portion of the blade's chord, the trailing edge correction program calculates the fraction of the chord length that would be altered, and if it is over the user-defined maximum, will require the lift co-efficient to be decreased. Decreasing the lift-coefficient will produce a wider and thicker blade which will have a smaller portion of the trailing edge requiring additional material.

3.4.7 Selecting an Airfoil for a Blade Station

As each airfoil is tested the program will compile a list of blade station solutions presented by all airfoils. The airfoil to be used for the blade station is selected from this list on the basis of three factors:

1. Validity of the solution. If a suitable blade station cannot be created with the airfoil, it will not be selected.
2. Variation in the lift coefficient from the one dictated by the lift coefficient condition. During the sizing process the lift coefficient of the station is reduced to obtain a larger blade chord and so the actual lift coefficient may be significantly lower than desired. If the blade were to be designed with an elliptical lift distribution a large difference would not produce this lift distribution. The code checks that the lift coefficient variance is within a user-defined acceptable variance limit; otherwise it will not use the airfoil. Blade station solutions that are within the acceptable variance limit are treated equally (i.e. a solution with a variance of 0.1 is treated the same as an airfoil with a variance of 0)
3. Highest lift-to-drag ratio, to maximize the efficiency of the blade section

If an airfoil cannot be selected following these criteria, an alternate selection criteria is used. This alternate selection method selects an airfoil based on fulfilling the intent of the lift-coefficient condition rather than being within an acceptable variance level. The program will select the airfoil that is closest to the desired lift coefficient (for elliptical and fixed lift coefficient conditions), the maximum lift-to-drag ratio (maximum lift-to-drag) or the lowest section drag (minimum section drag). The lift-to-drag ratio will be used in the case of airfoils of equal ability in this case (i.e. two airfoils that are both equally close to the desired lift coefficient). An invalid blade solution will never be accepted.

3.5 Propeller Blade Selection

Once the propeller blade has been designed to meet the thrust or power requirement at the primary design condition, the blade is scored. This process is identical to the process used for preliminary sizing other than the blade is analyzed with a strip-analysis method rather than a single point method. Once the score has been calculated, the rotational speed is increased until the performance scores begin to decrease or until the speed has reached the maximum allowable value. The program selects the blade with the highest performance score as the best propeller for the aircraft. The structural and aerodynamic performance of the blade is exported into a Microsoft Excel spreadsheet, and the shape of the blade is exported as series of text files can be imported into a CAD program by the manufacturing portion of the program.

3.6 Detailed Structural Analysis of Propeller Blades

The design program considers only the steady-state loads acting on the propeller as most higher-order harmonic forces have less of an influence and their neglect can be compensated for by the use of a safety factor [30, p. 74]. The loads on the blades are either due to aerodynamic forces, centrifugal forces (both described in **3.4.4**) or the interaction between both.

3.6.1 Aerodynamic Loads

Methods for calculating the thrust and drag acting on the propeller are presented in section 3.4.4 and are used verbatim in this analysis procedure.

The lift generated by any portion of a propeller blade depends on the section's angle of attack, or the difference between the blade angle and the angle that the air enters the propeller. In all of the analysis presented so far it has been assumed that air enters perpendicular to the propeller disc and so both blades generate the same amount of lift. However due to the aircraft's angle of attack and the angle that the propeller was installed in the aircraft the air may enter at an angle other than perpendicular to the propeller disc. This causes the angle of attack of the blade - and consequently the thrust developed by a given blade - to fluctuate based on the position of the blade. The magnitude of this fluctuating aerodynamic load (referred to as the 1^{st} order harmonic lift, or 1xP loading) is proportional the Aq factor, which is the product of the aircraft's angle of attack and free-stream dynamic pressure. While 1xP loads may seem to be a trivial factor, methods to analyze them were created after two instances of in-flight propeller failure on the

Douglas DC-6 (thankfully both aircraft safely landed) [45, p. 113]. The increase in stress due to this effect was significant enough to cause the steel propeller blades to fail.

The maximum additional lift on an element due to the increase in harmonic lift is [30, p. 65]:

$$\Delta L_{HL} = Aq\left[2C_L \cot\phi + \frac{dC_L}{d\alpha}\right] b\Delta r \qquad \textbf{Eq. 53}$$

It should be noted that, for the purposes of calculations, the Aq should be in units of pressure-radians and not pressure-degrees.

The change in lift and drag due the Aq factor effects more than the thrust and torque developed by a blade element. This additional lift increases the deflection of the blade resulting in another additional increase in lift, which is equal to [30, p. 69]:

$$\Delta L_{HL} = \frac{1}{2}\rho W^2 \frac{dC_L}{d\alpha}(\alpha_{1xP}) b\Delta r \qquad \textbf{Eq. 54}$$

Where:

α_{1xP} = the increase in angle of attack of the blade, equivalent to [30, p. 69]:

$$\alpha_{1xP} = \int_0^r \left(\frac{(Q_r)_{1xP}}{C_T}\right) dr \qquad \textbf{Eq. 55}$$

Where

C_T = blade torsional stiffness constant

$(Q_r)_{1xP}$ = torsion due to the first order lift, which is equal to [30, p. 69]:

$$(Q_r)_{1xP} = \int_r^R \left(\frac{\Delta L_{HL}}{\Delta r}\right) x_{cp}\, dr \qquad \textbf{Eq. 56}$$

Where x_{CP} is the distance between the aerodynamic centre of the blade foil and centre of gravity.

Combing the two main equations together,

$$\Delta L_{1xP} = Aq\left[2C_L \cot\phi + \frac{dC_L}{d\alpha}\right] b\Delta r + \frac{1}{2}\rho W^2 \frac{dC_L}{d\alpha}(\alpha_{1xP}) b\Delta r \qquad \textbf{Eq. 57}$$

This additional force, once divided into lift and drag components, can be added to the thrust to find the maximum air loads acting on the blade.

3.6.2 Mass Loads

Spinning any mass will generate a force that acts radially outwards from the centre of rotation, called the centrifugal force. The centrifugal forces generated by propeller blades have a large influence on the strength of the blade and typically cause most of the stresses within the blade. Methods for analyzing the centrifugal force was presented in 3.4.4 and those same methods are used.

The centrifugal force can be assumed to act at the centre of gravity of each blade element. For simplicity, the previous analysis introduced neglected the position of the centre of gravity of a blade element in relation to the rest of the blade, instead assuming they were aligned such that only axial forces were produced.

Any structure will deform when loads are applied to it, and propeller blades are no exception. Due to the air loads the blade will bend towards the thrust and torque directions resulting in the centre of gravity of each blade element moving. The change in the centre of gravity also leads to a shift in the point of application of the centrifugal

forces, creating a moment around the root of the blade. This moment typically acts to restore the blade to its original un-deflected position and is referred to as the blade centrifugal restoring moment. By manufacturing the blade with a built-in deflection, or tilt, it is possible to use the centrifugal restoring moment to reduce or even eliminate the bending moment produced by the thrust and torque forces which reduces stresses in the blade [30, p. 82]. Eliminating most to all of the bending moments from the thrust and torque forces through the use of blade tilt occurs only when the propeller is being operated in a very narrow range of advance ratios (for a fixed pitch propeller) or the blades are at one blade angle (for a variable pitch propeller) [30, p. 82]. The blade tilt needs to be selected for the flight condition that it will produce the most benefit [30, p. 82] but for this case it was assumed that the maximum benefit was on take-off when the propeller is producing its maximum thrust.

Typically the blade is "kinked" or bent slightly forward near the root of the blade during manufacture to achieve this tilt [30, p. 86]. However, if the blade is to be manufactured with additive manufacturing, this is impossible to do. Instead of assuming a constant angle, the deflection at each blade station needed to counteract the bending moment due to the thrust was calculated (Figure 14). This requires knowing the thrust and centrifugal forces acting on each blade element.

The total moments around any blade station in the y-axis or z-axis are:

$$M_{Total} = M_{Aero} + M_{CF} \qquad \textbf{Eq. 58}$$

If it is assumed that the total moments at the station is to be 0, then

$$-M_{Aero} = M_{CF} \quad \textbf{Eq. 59}$$

The bending moment from the thrust is much larger than that of the torque so it will be considered for analysis.

The offset in the z-axis needed to eliminate the bending stresses in the blade are found from the tip inwards. To do this the moment due to bending forces is found about the next station inwards. For this example the offset at the second station inward (Δz_{23}) from the tip will be found and so the moments would be taken around the third station inward. (Note that $\Delta T = \Delta F_y$ of a given station and that $r_1 - r_3$ is instead represented as Δr_{13}; these changes were done for greater visual clarity)

$$M_{aero\,3} = \Delta T_1 \, \Delta r_{13} + \Delta T_2 \, \Delta r_{23} \quad \textbf{Eq. 60}$$

The bending moments caused by the offset in the z-axis and elemental centrifugal forces is:

$$M_{CF\,3} = \Delta CF_1 \, \Delta z_{13} + \Delta CF_2 \, \Delta z_{23} \quad \textbf{Eq. 61}$$

$z_1 - z_3$ can also be seen as:

$$\Delta z_{13} = \Delta z_{12} + \Delta z_{23} \quad \textbf{Eq. 62}$$

Combining the previous four equations,

$$\boldsymbol{M_{CF\,3} = \Delta CF_1(\Delta z_{12} + \Delta z_{23}) + \Delta CF_2(\Delta z_{23})} \quad \textbf{Eq. 63}$$

Setting $M_{CF} = -M_{Aero}$,

$$\Delta CF_1(\Delta z_{12} + \Delta z_{23}) + \Delta CF_2(\Delta z_{23}) = -(\Delta T_1 \Delta r_{13} + \Delta T_2 \Delta r_{23}) \quad \textbf{Eq. 64}$$

Simplifying and solving for Δz_{23}

$$\Delta z_{23} = \frac{-(\Delta T_1 \Delta r_{13} + \Delta T_2 \Delta r_{23}) - \Delta CF_1 \Delta z_{12}}{\Delta CF_1 + \Delta CF_2} \quad \textbf{Eq. 65}$$

After the Δz between each blade station, the z position of the blade relative to the root of the blade (which is assumed to be at 0) is calculated. The offsets for the centre-of-gravity of each blade station in the y-axis are calculated using a similar procedure but also takes into account the z-axis locations.

Borst uses an iterative approach to solving for the blade bending moments due to the effect of blade deflection on the centrifugal bending moment. While thorough and accurate, the earlier approach provided in ANC-9 is sufficiently accurate and straightforward to understand. It was implemented verbatim and the interested reader is referred to ANC-9 for the full procedure.

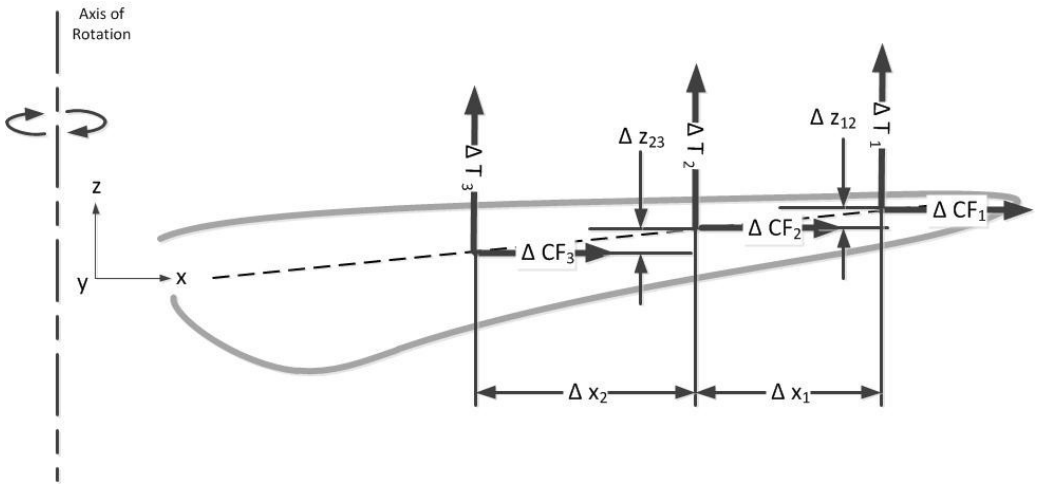

Figure 14 Centrifugal bending

4 Chapter: Material Testing

4.1 Introduction

4.1.1 The Need for Material Testing

One of the requirements in both FAR 35 and F2506 is that the designer ensures the selected material is useable in the intended operating environment and that the mechanical properties used for stress and fatigue analysis are representative of those of the actual part. The mechanical properties of many 3DP plastics are detailed on material data sheets provided by the manufacturer; however, these properties listing is usually minimal and lacks some key details such as the build orientation or infill of the part. The fatigue properties of 3DP plastics are typically not provided or there is limited literature on the topic [92], which complicates performing a fatigue analysis of the blade.

For most applications, sufficient data on the material's properties exists or the consequences of the part failing are not significant enough to require in-depth material testing. Material testing was justified, as the goal of this research is to prove a process for the design and manufacture of prototype UAV propellers suitable for wind tunnel and flight-testing. Without knowing life expectancy of the propeller flight-testing would be too risky to ever attempt. Likewise, if a propeller were to fail during wind tunnel testing the necessary "recovery time" (i.e. repairing the test rig & manufacturing new propellers) would delay or prohibit testing to be completed in a timely manner.

4.1.2 Tensile Stress Rupture

Propeller blades are subjected to large tensile stresses in operation due to their thin cross-section and the centrifugal loads generated by the mass of the blade being spun. Sustained tensile stresses (either due to static or dynamic loading) will lead to stress crazing and cracks forming over time, resulting in failure at stresses well below the yield stress [64, p. 275]. This phenomenon, known as stress rupture, is similar to creep but does not only occur at elevated temperatures. The time needed for a part to fail due to stress rupture depends on three main factors [64, p. 275]:

- Stress Environment
- Environmental conditions (chemical exposure)
- Stress risers (nicks, notches, sharp corners, etc)

Budinski & Budinski provide suggestions on how to avoid stress rupture that include [64, pp. 277-278]:

- *Using an alternative polymer*. This is not possible with current state of 3DP as many of the few available 3DP plastics are variants of one another
- *Fiber Reinforcement*. Fiber reinforcement is used by APC for the manufacture of their propellers, and a fibre-reinforced 3DP plastic called Duraform HST is available. However, adding fibre-reinforcement to 3DP blades is not necessarily practical without significantly modifying the printer or making a custom printer to produce 3DP blades.
- *Designing based on a stress of 1/6 to 1/10 of the material's yield stress.* A safety factor of 6-10 would be difficult to achieve using the conventional approach of

simply adding more material. The additional material cannot be added to the blade as it would increase the centrifugal force and the tensile stress, which would in turn require more material. This high of a factor of safety could only be achieved by reducing the diameter of the propeller or lowering its rotational speed, both of which would detrimental effects on the propeller's performance.

- *Design the part around a critical rupture stress.* This is suggested by Budinksi & Budinski as a best method of avoiding tensile stress rupture and for this application very much is the appropriate option.

The critical rupture stress is not readily available for all polymers and had not been investigated for rigid 3DP polymers, although some work has been done by the University of Texas on 3DP elastomers [93] . Anecdotal reports on the long-term performance of 3DP polymers (i.e. "3D printed fan blade ran for exactly 10 minutes and then shattered into a million pieces" [94]) were found through an internet search, but no quantitative data on stress or information on the design of the component was provided.

4.1.3 Objectives of Material Testing

Given the lack of test data for a number of 3DP polymers beyond that provided on the manufacturer's material data sheets along with the unknown critical rupture stress, material testing was undertaken to complete two primary objectives:

1. To evaluate the as-manufactured properties of 3DP plastics prior to their use in a propeller blade.

2. To ensure that the materials to be used for 3DP propeller blades can withstand continuous tensile stresses for the expected lifespan of the propeller blade during testing.

4.2 Material Testing

4.2.1 Overview

Testing was completed on two materials considered suitable for manufacturing 3DP propellers. As planned testing for this research was conducted indoors within a wind tunnel and under controlled laboratory conditions, environmental effects will not be a factor. For each material a batch of ten test coupons were produced all in the same print orientation to ensure that they are identical.

At least three sample from each batch printed were used to determine the tensile yield stress (σ_{ty}) of the material. Tensile testing will allow for the tested strength of the test specimens to be compared to the expected strength given on the material data sheet and to evaluate how the material fails.

Stress rupture testing was conducted by subjecting specimens to a constant tensile load until they failed. The propeller blades are designed such that when subjected to twice the maximum centrifugal loads, they will have an overall factor of safety of 1.5. The maximum applied tensile stress in this case is then $2/3\sigma_{ty}$. When the blade is generating its maximum centrifugal loads the maximum allowable stress is then $1/3\sigma_{ty}$. To meet the requirements of FAR 35.35, the blade would need to be able to be stressed to $2/3\sigma_y$ under a load for at least one hour or preferably beyond this until failure, and the

specimens stressed to $1/3\sigma_{ty}$ would, under a worst-case scenario loading need to last preferably for the upper range of the operational lifespan of a small UAV (250 hours) but at least for the amount of time needed for wind tunnel testing (10 hours).

4.2.2 Materials Tested

The two 3DP materials that were tested were as part of this research were:

- P400 ABS, a common ABS plastic widely used in office/industry-grade fusion-deposition manufacturing (FDM) 3D printers. P400 is suited for making models and simple 3DP parts [95].
- Duraform HST, a glass fibre-reinforced plastic with very high stiffness. This material is printed using selective laser sintering (SLS) 3D printers. Duraform HST is intended for functional prototypes, fans and impellers, and UAV components [96].

Some basic mechanical properties as provided by their manufacturers are listed below [95] [96].

		P400 ABS	Duraform HST
Specific Gravity		1.04	1.2
Tensile Strength, Yield	[MPa]	22	48
Tensile Modulus	[GPa]	1.627	5.475
Flexural Strength, Yield	[MPa]	41	85
Flexural Modulus	[GPa]	1.834	4.4
Tensile Elongation		6%	4.50%

Table 1 Material Properties of P400 ABS and Duraform HST

4.2.3 Guidance for Testing

ASTM D638-10 *Standard Test Method for Tensile Properties of Plastics* and D2990-09 *Standard Test Methods for Tensile, Compressive, and Flexural Creep and Creep-Rupture of Plastics* were consulted for guidance on conducting tensile and stress rupture testing. As it would take too long to complete a thorough evaluation of the creep rupture properties of both plastics (due to the number of specimens and tests that would be required) and was deemed unnecessary for the purposes of designing propeller blades, the standards were followed only for the test process and test specimen design.

4.2.4 Test Specimen Design

Type I dog bone-style test specimens, as detailed in D638, were manufactured from both plastics. These specimens were used for both tensile and stress rupture testing. Based on use of 3D printing as a substitute to injection moulding, the dog bones were printed with a thickness of 5 mm as dictated by D638. The dimensions of the dog bones are shown below

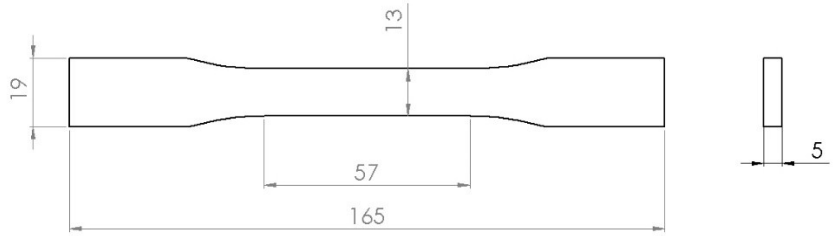

Figure 15 Type I Dog bone

4.3 Tensile Testing

4.3.1 Overview

Tensile testing was completed in two separate sessions that occurred approximately a month part. Testing for both sessions was conducted with the same equipment and procedures; the only difference between sessions was the materials that were tested. The first session - "Round 1" – involved testing four P400 dog bones while "Round 2" tensile testing involved testing six P400 dog bones (three from two different batches) and three Duraform HST specimens.

4.3.2 Test Equipment & Procedures

The tensile tests were conducted using a MTS Dynatron 810 Universal Test Machine (Figure 16). The Dynatron 810 is capable of applying a 10kN load that is well in excess of what is required for material testing. The axial force applied and displacement of the head was recorded automatically at a rate of approximately 2 samples per second.

Before testing, as per ASTM D638-10, the width and thickness of the specimens were measured at the limits of the gage section and any defects were noted. Approximately 25mm of the grip of each ends of the specimens were gripped with the serrated jaws of the MTS material testing machine and a pressure of 100 psi was applied to clamp the specimens in place. The dog bones were tested by moving the measurement head at a constant rate of 5mm/min until the specimen failed.

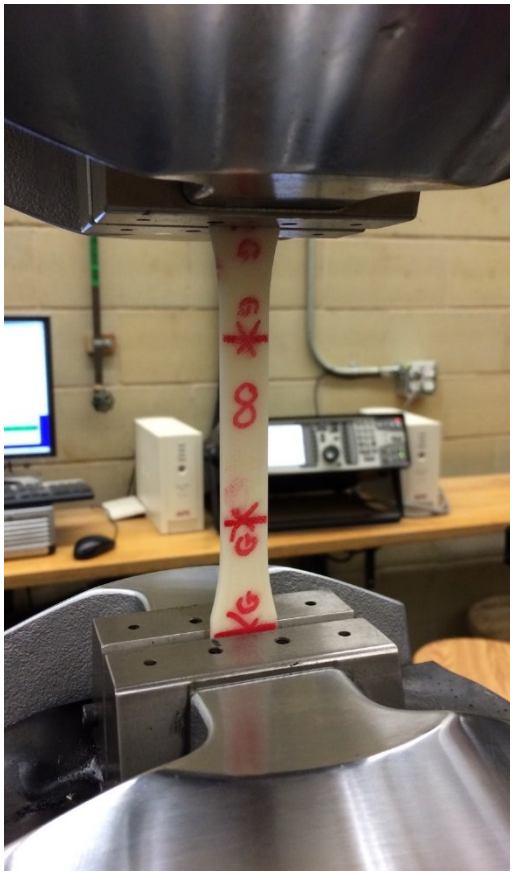

Figure 16 Batch A dog bone installed in Dynatron 810 MTS

4.3.3 Round 1 Tensile Testing

4.3.3.1 Summary

A series of P400 dog bone specimens (referred to as Batch A) were used for the initial round of testing as they were inexpensive and replacements could be easily manufactured within the department (Figure 17). These dog bone specimens were printed on a Stratasys BST 1200es FDM printer as a single batch. This printer has a build volume of 254mm x 254mm x 305mm and deposits a layer thickness of 0.33mm [75]

A small bump was noted on the side of the dog bones approximately 39 mm from the edge of a grip of each part (Figure 18). The bump extends approximately 1 layer

(0.33mm) above surface and is not visible in .STL file used to print the part. The cause of the bump is unknown but it possibly is from printer head at start/ completion of part. One specimen had a small void (~2mm) with traces of the build support material stuck inside the void. This specimen was kept aside from being used for testing.

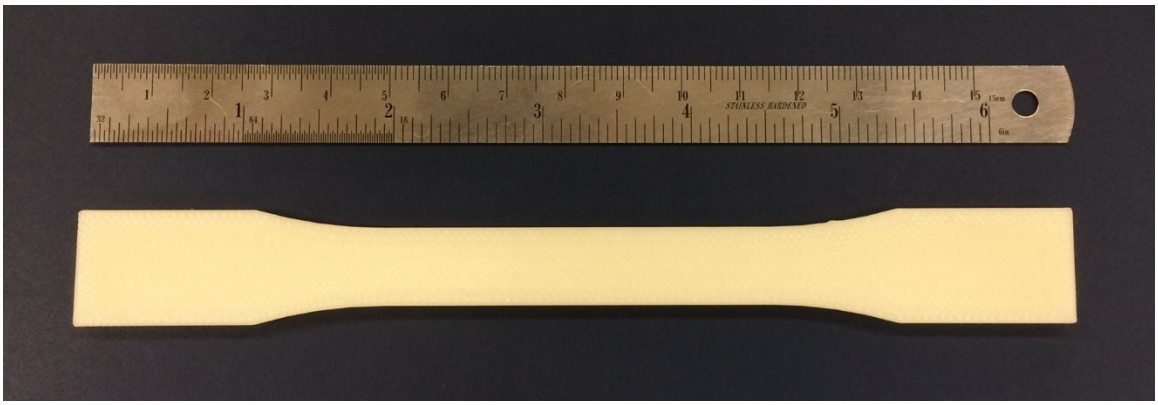

Figure 17 P400 dog bone material specimen

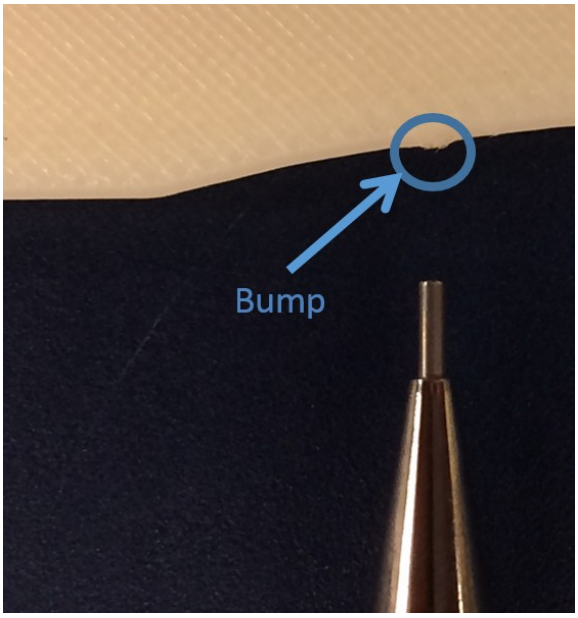

Figure 18 Bump noted on material dog bone (tip of 0.7 mm mechanical pencil for scale

The specimens were measured prior to testing and it was found that the width and thickness at both ends of the gage section varied slightly (Table 1). The specimens were into three groups of three specimens, with two sets being “mirror images” of one another

(each with specimens of the same sizes) which were to be used for creep rupture testing. The third set was used for tensile stress testing.

Specimen	Width [mm]	Thickness [mm]	Area [mm^2]
1	12.88	3.45	44.49
2	12.88	3.45	44.49
3	12.88	3.48	44.81
4	12.88	3.53	45.47
5	12.88	3.53	45.47
6	12.90	3.45	44.57
7	12.90	3.45	44.57
8	12.90	3.48	44.90
9	12.90	3.51	45.23
10	12.95	3.48	45.08

Table 2 As-measured dimensions of Batch A specimens

The first dog bone tested failed near neck at the bump. For the test to be considered valid, the failure needed to occur within the narrow gage section. As a result, this test was unacceptable test according to ASTM standard. One possible reason why the failure occurred in this location was that the bump acted as stress riser. While this seemed unlikely due to the bump's small size, the second dogbone tested had its bump sanded lightly with 400 grit sand paper until it felt (to the touch) as if it was almost fully removed. (Some of the bump was left on to avoid removing too much material). Regardless of this sanding, the second specimen failed at the bump again. Both specimens had been orientated so that the bump was located at the "top" of the specimen, with raised the possibility that the upper grip may be, in some way, a factor. For the third trial, the specimen was "flipped around" so that the bump was closer to the bottom grip; however, failure still occurred at the location of the bump.

Markings had been drawn on the specimens intended for tensile or stress rupture testing with a Sharpie 13-14 hours before testing. These markings had been applied to indicate grip and gage lengths, with the goal of allowing quick and correct installation of the samples into the MTS machine. The location of the bump was also marked so that parts could be tested in a uniform orientation. The grip and gage markings were drawn on the front and back faces of the dog bone with the bump marks being drawn on the side of the specimen. ABS generally resists chemical attacks very well but is susceptible to attack from organic solvents [64, pp. 298-299]. It was found that organic solvents are a key component of the inks in permanent Sharpie [96]leading to the possibility that the part failing was due to chemical attack.

When a line is drawn on a 3DP part the ink seeps away from the line due to the grooves formed by the beads of plastic. Based on visual observations of the part, the ink will seep away mostly in-plane (on the surface it was applied) as the groves on this layer are the path of least resistance. Some ink will also penetrate into the part in the openings between each layer. The ink applied to the top and bottom faces behaved this way and considerably more ink was applied to these faces than on the bump on the side. However, the ink applied to the side of the part spread through the groves between the beads and was applied to the full thickness of the part, affecting more plastic than the surface markings. This, along with the increased stress in the neck region, likely led to the part failing at the bump.

Due to the minor defect, sample 10 had not been marked with Sharpie (prior to immediately before testing) and was available. It had been set aside for a quick check of the stress rupture properties of P400 by stressing it to $2/3\sigma_{ty}$ for a short duration to see if

failure occurred. This test was conducted (with the specimen showing no signs of failure after constant loading of about 45 minutes) and it was then subjected to a tensile yield test in the MTS machine. This dog bone failed inside the valid gage region and under a slightly higher load, which indicated that the Sharpie ink had likely chemically attacked the specimens.

4.3.4 Lessons Learned From Round 1 Testing

Specimen	Width	Thickness	Cross-sectional area	Failure Load		Head Displacement	
				Predicted	Actual	Yield	Failure
	[mm]	[mm]	[mm^2]	[N]	[N]	[mm]	[mm]
3	12.88	3.48	44.81	988.7	1139	2.25	6.50
4	12.90	3.51	45.23	997.9	1152	2.26	5.82
8	12.95	3.48	45.08	994.6	1143	2.34	5.74
10	12.95	3.48	45.08	990.7	1165	-	5.74

Table 3 Round 1 Tensile Testing

The test results were adversely affected by the Sharpie ink such that accurate material properties could not be determined from the test. The failure loads and the head displacement from testing are shown in Table 3and, even after chemical attack, the failure loads were higher than was predicted based on the properties provided by the manufacturer. The manufacturer completed testing in compliance with ASTM D638 and so it is likely that the properties they reported was based on testing more than four specimens. The orientation that the samples were 3D-printed and the percent infill (the ratio of the volume of plastic to ideal volume of the part) was not mentioned. The tested samples were printed in the strongest orientation and 100% infill. It is possible the manufacturer chose to test a “middle-of-the-road” infill and build orientation to have

slightly more conservative material properties. Regardless, the testing showed that the material performed as intended and datasheet values could be trusted.

4.3.5 Round 2 Tensile Testing

4.3.5.1 Summary of Testing

The goals of the second round of testing were to determine the yield and ultimate tensile stress of:

1. P400 ABS specimens not affected by Sharpie ink ("Batch B")
2. Duraform HST specimens
3. P400 ABS specimens that had been marked, several weeks earlier, with Sharpie-ink ("Batch A") to see if the ink had any lasting effect on the strength of the material.

There were no visible defects on Duraform HST specimens, and batch B of P400 samples still had the small bump noted on batch A specimens (Figure 19). However, six of the ten batch B P400 specimens had defects (Figure 20). Defects were mostly gouges ("craters"), some with build material adhered to them and while they occurred only on one face, they were not consistently located in one region of the part. A possible reason for large number of defects and only on one side is that the printer bed had not been thoroughly cleaned prior to printing.

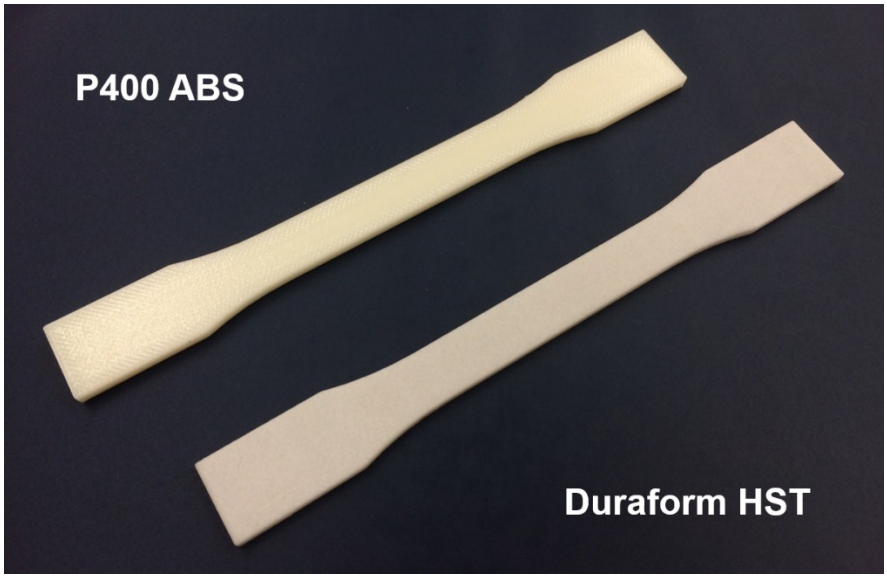

Figure 19 P400 ABS and Duraform HST specimens

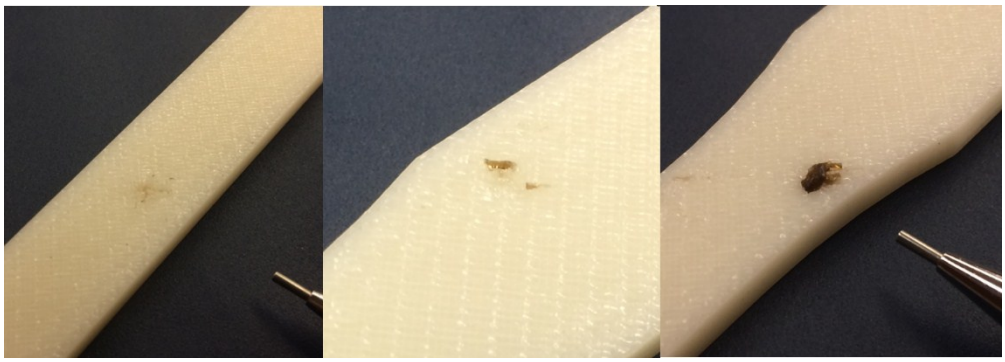

Figure 20 Surface defects on Batch B P400 specimens. From left to right: crater with no build material, crater with minor build material, crater with major build material

Measurements showed both the Duraform HST and P400 samples had some slight variation in thickness, but the variance was approximately equal for both materials. The Duraform HST specimens were closer to the intended shape than P400 specimens, especially in thickness. This was likely due to the finer build layers.

Sample	Width "A" [mm]	Width "B" [mm]	Thickness [mm]	Area [mm^2]	Est. Breaking Force* [N]
1	12.90	12.88	3.175	40.93	1989
2	12.93	12.88	3.175	40.97	1991
3	12.88	12.88	3.175	40.89	1987
4	12.83	12.85	3.099	39.79	1934
5	12.93	12.90	3.175	41.01	1993
6	12.90	12.90	3.124	40.31	1959
7	12.90	12.93	3.099	40.02	1945
8	12.90	12.88	3.099	39.95	1942
9	12.88	12.88	3.175	40.89	1987
10	12.90	12.90	3.175	40.97	1991
11	12.90	12.88	3.124	40.27	1958
12	12.90	12.88	3.124	40.27	1958
**Based on ultimate tensile stress of 48 MPa from mfr. datasheet*					

Table 4 Dimensions of Duraform HST dog bone specimens

While testing was conducted with the same process as was used for Round 1 testing, there was some difficulty in mounting specimens in the MTS machine. The grip length (the distance between the grips) was supposed to be 115mm according to D638-10. This was easily achieved when mounting batch A P400 samples as markings were available for alignment. Markings had not been applied to Batch B or Duraform HST specimens and so the grip length varied and was typically less than defined in the test standard. The true grip length of each specimen was determined post-test by measuring the length of the indentations on the grip portion of the specimen made by the grips of the MTS machine.

Sample	Width "A" [mm]	Width "B" [mm]	Thickness [mm]	Area [mm^2]	Est. Breaking Force* [N]	Defects
1	12.88	12.88	3.480	44.81	1139	No flaws
2	12.88	12.88	3.480	44.81	1139	Crater above midpoint, 2 craters w/ build minor material below neck, crater & build material on top grip near edge
3	12.88	12.88	3.454	44.49	1131	2 craters on bottom neck, scratch & build material on top grip near the top edge
4	12.88	12.90	3.454	44.53	1132	Major build material on top neck, scratch near edge of top neck
5	12.88	12.88	3.480	44.81	1139	Scratch on top grip, crater & minor build material on top neck
6	12.90	12.88	3.454	44.53	1132	Craters on top grip & upper-mid
7	12.90	12.90	3.454	44.57	1133	Crater at midpoint
8	12.95		3.454	44.75	1137	None - used as a stress rupture test specimen
9	12.88		3.480	44.81	1139	None - used as a stress rupture test specimen
10	12.90		3.429	44.25	1124	None - used as a stress rupture test specimen
**Based on an ultimate tensile stress of 25.4 MPa from round 1 testing*						

Table 5 Batch B P400 dimensions and noted defects

Three P400 batch B specimens were tested and did not show any significant difference in strength from the batch A specimens tested in either round 1 and 2. The batch B specimens were tested a week after they had been produced which for some unknown reason may have reduced their sensitivity to the Sharpie ink. The specimens failed nearly instantaneously across their full width and thickness and away from the surface defects, suggesting that these did not have a major influence in the tensile strength of the material.

Three Duraform HST specimens were tested. A computer glitch during first test of a Duraform HST caused data not to be recorded. Based on the author's recollection, the first specimen failed at a load similar to other two. Failure occurred instantaneously with two of the samples failing outside of gauge area.

Three mechanical properties were extracted from the test data:

- 0.2% offset yield stress;
- yield; and
- breaking (or ultimate) stress.

The results of the tensile tests of round 2 are shown in Table 6, Table 7, and Table 8 . Overall both materials performed were expected of them and samples failed under consistent stresses suggesting reliable mechanical properties. Testing revealed that the Duraform HST behaved slightly different than P400. For P400, the stress increased at a constant rate with respect to elongation until the yield stress was reached, at which point the stress remained approximately constant while the material continued to elongate until failure (Figure 21). Duraform HST acted in a similar manner (Figure 22) but had a

distinct 0.2% offset yield point, and a different yield and ultimate stress. The 0.2% offset yield stress of Duraform HST was much lower than the yield point, possibly due to this material's increased stiffness.

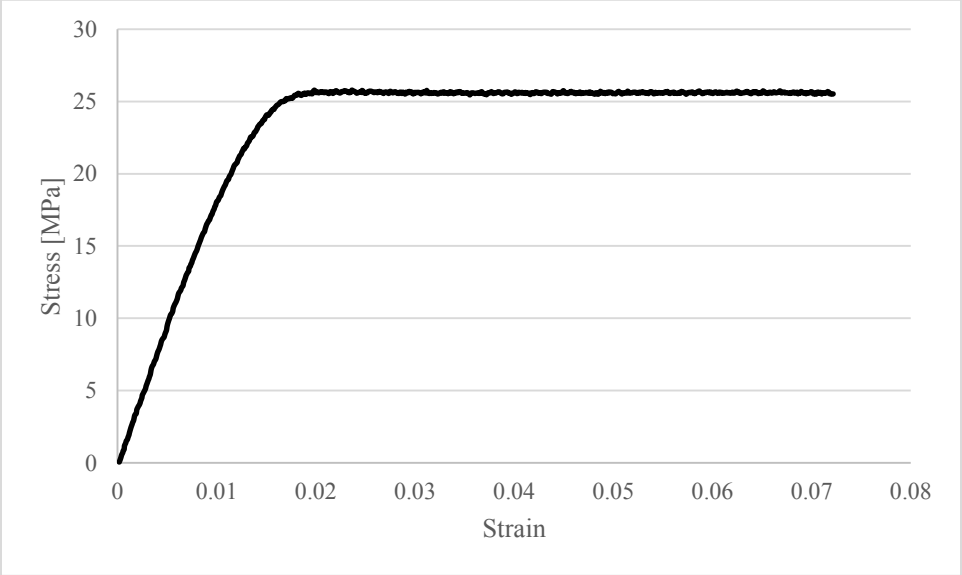

Figure 21 Typical stress-strain curve for a P400 dog bone (Batch B, sample 5)

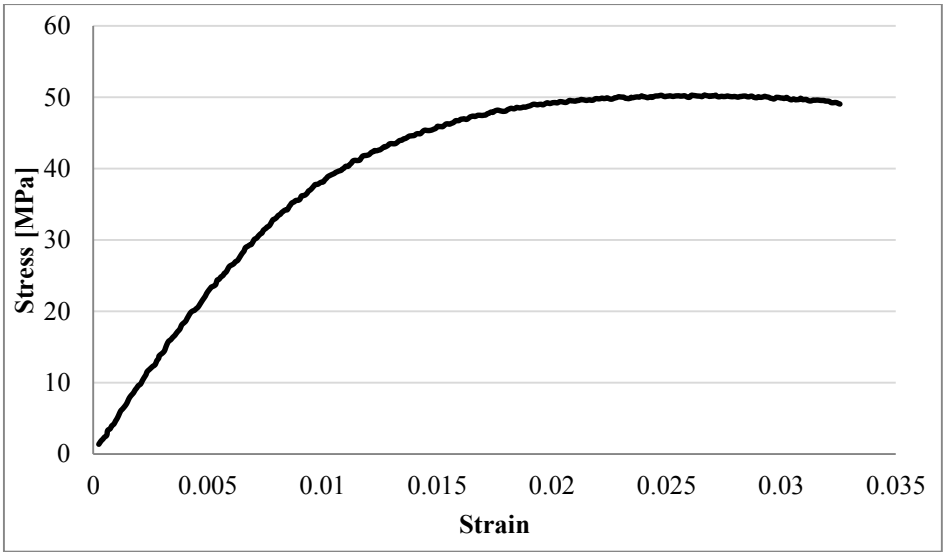

Figure 22 Typical stress-strain curve for a Duraform HST dog bone (for sample 9)

Another observation made during test was that P400 stress whitened before failure whereas the Duraform HST did not (Figure 23). While the whitened area is not much lighter in colour than the original material and may be difficult to recognize on more complex shapes, stress whitening is a useful indicator the part beginning to fail. This trait is useful for propellers that are likely going to be only subjected to a visual inspection.

Figure 23 Comparison of failed P400 and Duraform HST dog bones

4.3.5.2 Lessons Learned From Round 2 Testing

Overall it was assessed that P400 and Duraform HST performed as expected based on the material properties indicated on their datasheets. It was also determined that minor printing defects did not have did not have any significant effect on the mechanical properties of the material.

Sample	Est. Breaking Force* [N]	0.1% Offset Yield			Yield Point			Ultimate (breaking)			Failure location (as mounted)
		Applied Force [N]	Stress [MPa]	Strain	Applied Force [N]	Stress [MPa]	Strain	Applied Force [N]	Stress [MPa]	Strain]	
1	1989	Not Recorded									Bottom, above neck but outside of gage
3	1987	1631	31.14	0.0162	2022	49.46	0.0591	2004	49.02	0.0699	Bottom, near gage limit
9	1987	1432	31.34	0.0162	2051	50.17	0.0565	2004	49.02	0.0698	Bottom, above neck but outside of gage

Table 6 Duraform HST Round 2 tensile test results

Sample	Est. Breaking Force* [N]	0.1% Offset Yield			Yield Point			Ultimate (breaking)			Failure location (as mounted)
		Applied Force [N]	Stress [MPa]	Strain	Applied Force [N]	Stress [MPa]	Strain	Applied Force [N]	Stress [MPa]	Strain]	
1	1139	1138	25.39	0.0169	1163	25.95	0.0221	1138	25.40	0.0673	Bottom, upper portion of neck
5	1139	1069	23.86	0.0149	1151	25.69	0.0225	1127	25.32	0.0769	Near top of gage section
6	1132	1110	24.93	0.0174	1132	25.42	0.0221	1144	25.53	0.0722	Near bottom of gage section

Table 7 P400 Batch B round 2 tensile test results

Sample	Est. Breaking Force* [N]	0.1% Offset Yield			Yield Point			Ultimate (breaking)			Failure location (as mounted)
		Applied Force [N]	Stress [MPa]	Strain	Applied Force [N]	Stress [MPa]	Strain	Applied Force [N]	Stress [MPa]	Strain]	
1	1131	1151	25.88	0.0168	1183	26.60	0.0208	1163	26.15	0.0713	Near bottom of gage section
2	1155	1060	23.32	0.0175	1101	24.21	0.0545	1081	23.77	0.0550	Near bottom of gage section
7	1133	1179	26.44	0.0166	1203	26.99	0.0200	1167	26.18	0.0339	Bottom, upper portion of neck

Table 8 P400ABS Batch A round 2 tensile test results

4.4 Stress Rupture Testing

4.4.1 Overview

Stress rupture testing was conducted over the course of three months. After a brief initial test to ensure the material could withstand a stress of $2/3\sigma_{ty}$, a stress rupture test rig was assembled and weights were hung from the test specimens, first for a period of approximately 250 hours, and then (with new specimens) until failure.

4.4.2 Initial Testing

The purpose of this test was to ensure that the material could withstand continuous tensile stresses long enough to make it worth evaluating this phenomena. As mentioned, this test occurred on the MTS machine as part of round 1 testing. The specimen was subjected to a constant load of (765N), which was 2/3 of force that the other specimens failed at. After 45 minutes of load application the dog bone had elongated 0.1016mm but otherwise showed no other signs of damage.

4.4.3 Stress Rupture Test Rig

A stress rupture rig was assembled to test the material specimens until failure (Figure 24). This rig allowed for three specimens to be tested and recorded the time of each part failure. Clamps made from two pieces of 0.125“ 3003-H14 aluminum by a pair of ¼” Grade 5 hex-head bolts and nylon lock nuts held the specimens (Figure 25). To prevent the specimens from slipping within the clamps, a strip of drywall sandpaper was sandwiched between either side of the specimen and aluminum plate. Oversized holes in the clamp allowed for the specimen to self-align when the weights were hung from the

lower clamp. To record the time of failure and to allow for off-site checking of the specimens an Arduino Duemilanove and a laptop with an Internet connection was used. A “tear switch” was fashioned by wrapping thin single-strand wire around the upper and lower clamps and loosely hooking a strip of aluminum foil to the wires. When the specimen failed, the wire attached to the falling clamp would tear free of the foil (or, alternatively, rip the foil free of the wire on the upper clamp) breaking the circuit. The Arduino was configured to sense the state of the tear switches of each specimen and constantly send the switch states to the program running on the laptop, which would create a text file if a change was sensed and at five minute intervals. These files were synced to a Google Drive account, allowing for the state of the specimens to be checked from any device with Internet access. A daily check was performed by opening and closing a toggle switch that had been wired into each circuit in series. During this daily check a visual inspection of each specimen was performed to look for cracking.

Figure 24 Stress Rupture Test Rig

Figure 25 Mounted test specimen

4.4.4 Stress Rupture Testing

Three samples from batch A of the P400 dog bones were tested for between 208 to 231 hours before they were removed for material testing. Subsequent testing of batch B samples at comparable or higher stress levels lasted well in excess of 1000 hours. One specimen, that had been stressed to 14.74 MPa (slightly less than the $2/3\sigma_{ty}$ stress of 17.18 MPa) failed due to stress rupture after 644 continuous hours of loading (Figure 25). Fracture occurred near the neck of the part and cracking was first seen here after approximately 150 hours of continuous loading. It should be noted that in accordance with D2990-09, failure outside of the gage area renders the test invalid. However, the goal was to prove that the material could withstand the stresses that it would see in

service. As the duration was much greater than was necessary, the need to meet D2990-09 was considered as irrelevant. A specimen from batch B has been subjected to the same stress for over two months without failure. One Duraform HST sample was put on the frame and stressed to over 40% of σ_{ty} for over two months without failure.

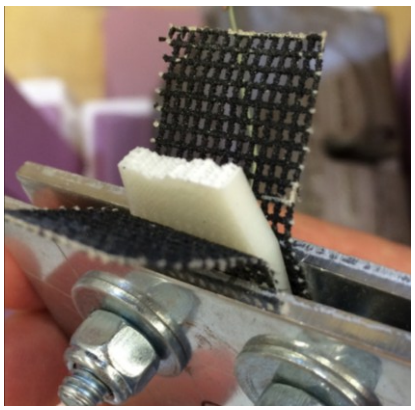

Figure 26 P400 specimen which failed due to stress rupture

4.4.5 Effect of Tensile Stress on Strength

Three samples that had undergone continuous tensile loading for between 208 and 231 hours were subjected to a tensile load test during round 2 testing. A summary of the loading and duration is shown in Table 9 and test results are presented in Table 10. It was found that the stressed specimens broke at a marginally lower stress after less elongation than the remaining batch A specimens which were also tested that day. This suggested that while the material did fatigue, the effect of constant tensile loading was minimal and did not seriously affect the strength of the part.

4.5 Conclusions

The two objectives of the material testing program were met. The as-manufactured strength of the blade, even when the part has minor surface defects, is still

higher than the values provided on the material data sheet. This provides assurance that even if there are minor defects, the propeller blade can be still used. It was also beneficial to see how both materials fail as that allows for better visual inspections to recognize any defects or signs of damage before blade failure occurs. The stress rupture testing also confirmed that the P400 material could be stressed to twice the maximum stress seen in service for longer than the lifespan of the propeller before failure. This was only a simple assessment of the stress rupture properties and did not fully consider fatigue, however given the short lifespan of a SUAV propeller fatigue failures are more unlikely to occur than the loss of the aircraft.

Overall, testing showed the durability of both 3DP and gave significant confidence in using these materials for propellers.

Sample	Width "A" [mm]	Width "B" [mm]	Thickness [mm]	Area [mm^2]	Est. Breaking Force* [N]	Applied Load & Duration
5	12.88	12.88	3.531	45.47	1155	39.05kg for 8 days, 16 hours, 36 minutes and 14 seconds (~208 hours)
6	12.88	12.88	3.454	44.49	1131	25.553kg for 9 days, 15 hours, 59 minutes and 3 seconds (~231 hours)
9	12.88	12.90	3.454	44.53	1132	54.114kg for 8 days, 19 hours, 38 minutes and 59 seconds (~211 hours)

Table 9 Summary of loading and duration of loading of P400 stress rupture test specimens

Sample	Est. Breaking Force* [N]	0.1% Offset Yield			Yield Point			Ultimate (breaking)			Failure location (as mounted)
		Applied Force [N]	Stress [MPa]	Strain	Applied Force [N]	Stress [MPa]	Strain	Applied Force [N]	Stress [MPa]	Strain]	
5	1155	1065	23.43	0.0166	1096	24.11	0.0261	1073	23.60	0.0359	Near bottom of gage section
6	1131	1145	25.74	0.0163	1182	26.57	0.0207	1078	24.23	0.0300	Mid gage section
9	1132	1113	24.99	0.0159	1146	25.74	0.0208	1095	24.59	0.0274	Upper-mid gage section

Table 10 Results of tensile testing previously stressed P400 ABS specimens

5 Chapter: Design and Testing of the Wind Tunnel Propeller Test Rig

5.1 Introduction

To facilitate safe performance testing of propeller blades in a low-speed wind tunnel for this research, the wind-tunnel propeller test rig (WTPTR) was designed and manufactured (Figure 27). The WTPTR consisted of two major components – an instrumented test stand to measure propeller thrust and torque and a protective shroud that would, in the event of a structural failure of the propeller, contain any possible damage to the wind tunnel. If the propeller failed during testing outside the wind tunnel, the shroud would significantly reduce the kinetic energy of the blade to avoid injuring bystanders.

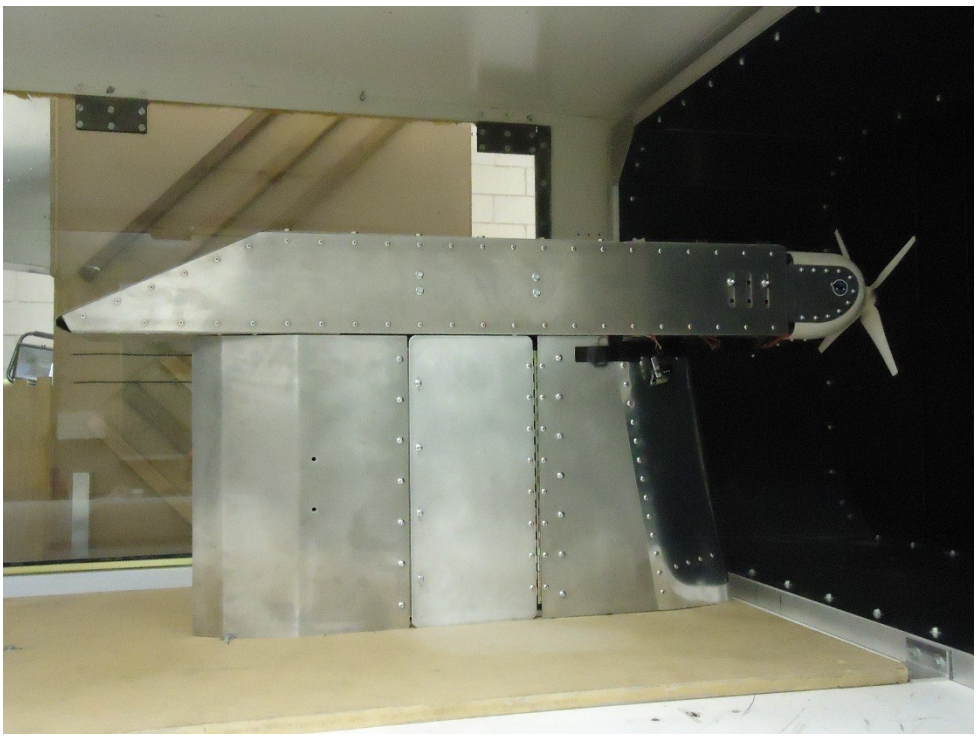

Figure 27 Wind Tunnel Propeller Test Rig (WTPTR) assembled and installed in the 4' x 6' low speed wind tunnel at Carleton University

5.2 Propeller Test Stand

5.2.1 Overview

The purpose of the test stand is to measure the thrust and torque generated by the propeller in static or simulated flight conditions. Unsurprisingly, the thrust and torque generated by a propeller with a diameter between 0.25 – 0.58 m is very low: <200N thrust and less than 11.5 Nm of torque. As the rig was testing experimental propellers, it was required to withstand the forces that would occur in the event of a propeller failure where a single blade is ejected from the hub. This force, which would be applied to the propeller shaft of the motor, is equal to the centrifugal force of the ejected blade and is proportional to the motor's rotational speed. For a large diameter propeller spinning at high rotational speed (over 6000 RPM) the force subjected to the propeller shaft of the motor in a blade-off condition can be in excess of 4400 N (1000 lbf).

5.2.2 Review of Existing Test Rigs

A review of several existing test rigs lead to several observations:

1. Test rigs that mechanically amplify the thrust force before measurement [97] using a lever mechanism generally worked better than test rigs which attempted to measure it directly [98].
2. Designs that used sliding or rolling contacts generally had measurements with a greater amount of error than designs which avoided these types of contact. Therefore, rolling, pivoting or sliding contacts should be avoided [98].

3. Properly sized and integrated commercially available off-the-shelf transducers generally worked better [9] than “homemade” ones [99].
4. Few if any designs incorporated any nacelle or cowling behind the propeller to conceal the test rig or mimic the shape of a representative aircraft. Thrust generated by the propeller when installed on the aircraft depends on the geometry of the nacelle or the fuselage housing around the engine [16] [100]. The design of an aircraft's nacelle is typically selected through significant wind tunnel testing as even small changes of the aft body shape affect the thrust generated by the propeller [16]. Some of the researched test rigs had significant amounts of structure behind the motor and propeller that likely had some effect on the measured thrust [99].
5. Withstanding the forces generated in a blade-off condition was not listed as a design condition in any other test rig design.

These observations were used to create the design of the wind tunnel rig shown in Figure 27 and Figure 28 for this research project. The mechanical design of the test rig was loosely based on the design of the University of Illinois propeller test rig due to the high quality of measurements taken with it and dimensions and the nacelle and pylon skins were based on those of propeller test rigs designed by Fokker [101] and Lorenz [34].

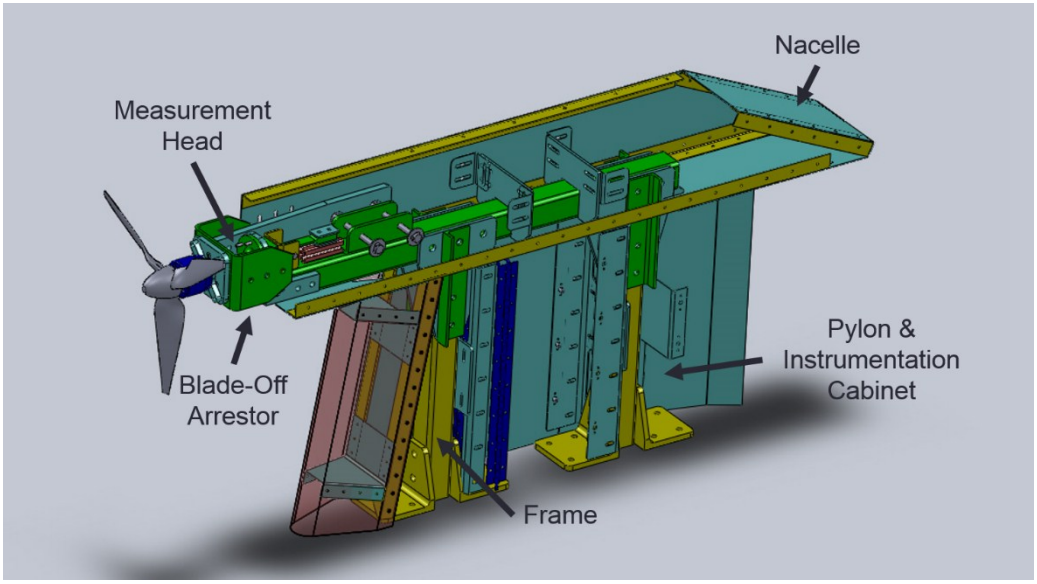

Figure 28 Propeller test stand with major subassemblies noted

5.2.3 Design and Operation of the Test Stand

The test stand was made entirely from aluminum sheet and extrusion and was mounted to ¾" thick sheet of Medium-Density Fibreboard (MDF), which acted as a support base to allow the rig to be easily removed from the wind tunnel for static performance testing. The stand has a maximum overall height of 0.6 m (24") length of 1.3m (52") and width of 0.16 m (6.25"). It is composed of five major subassemblies noted in Figure 28.:

- The **measurement head** which is designed to measure thrust and torque of the propeller by means of strain gauges attached to a torque cell and a bending beam;
- The **blade-off arrestor** which retains the measurement head in the event of a blade-off situation;
- The **frame** which provides a rigid and strong mounting fixture; and

- The **nacelle, pylon and instrumentation cabinet** which protects instrumentation and wiring from the wind and simulate the shape of a small UAV.

5.2.3.1 Measurement Head

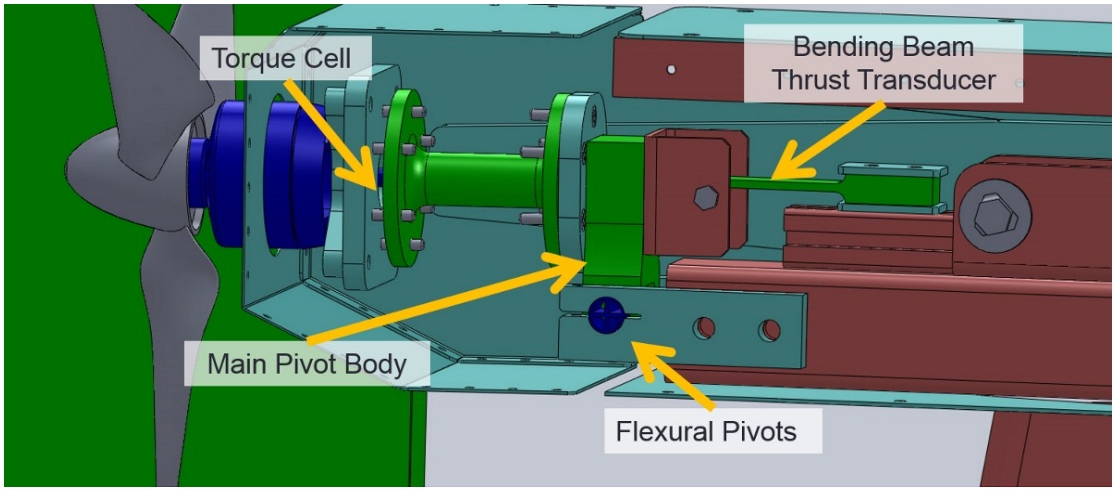

Figure 29 Measurement Head Components

As shown in Figure 29, the propeller and motor are attached the measurement head, which is an assembly of machined 6061-T6 aluminum parts including a torque cell, motor mounting plates, and a main pivoting body which rotates on flexural pivots. Flexural pivots were used to allow for frictionless and hysteresis-free movement for the small amount of rotation required for the pivoting body. When the propeller is generating thrust the measurement turn pivots downward until it a bar at the back of the head makes contact with a short metal beam. This beam is instrumented with strain gauges and is used to measure the thrust generated by the propeller. The flexural pivots are held in place by clamps located on the measurement head and attached to the upper member of the frame. One of the major components of the measurement head is a thin-

walled aluminum tube with flanged ends. This tube is instrumented with strain gauges and acts as a torque cell that measured the torque generated by the propeller.

5.2.3.2 Blade-Off Arrestor

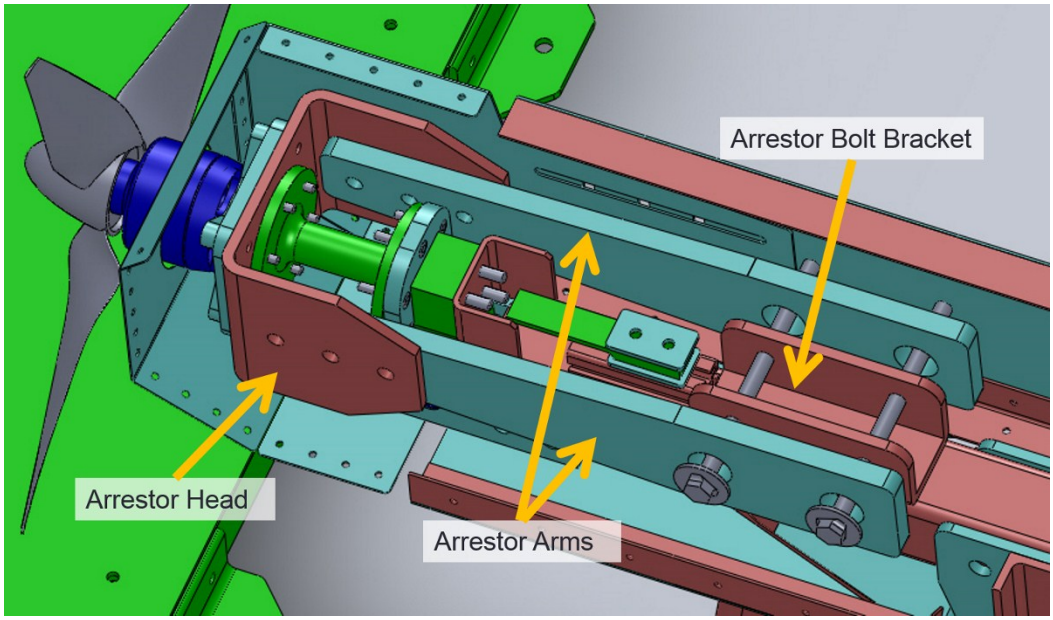

Figure 30 Blade-Off Arrestor

In the event of an ejected propeller blade, the forces applied to the shaft of the propeller may be large enough to cause the flexural pivots to shear, causing the measurement head to possibly break free from the test stand. To prevent this, a blade-off arrestor attaches to the measurement head between the motor mount and the torque cell. During normal operations the blade-off arrestor allows for the measurement head to flex freely but should excessive rotation or failure of the flexural pivots occur, the two holes in the arrestor's arms will catch around two ½" bolt or contact an aluminum C-channel extrusion welded onto the top of the upper member of the frame. The blade-off arrestor consists of a U-shaped frame (cut down from 5" x 5" x 0.25" 6061-T6 square aluminum

tubing (with square rather than filleted edges) and two arms, made from 0.5” thick 6061-T6 plate.

5.2.3.3 Frame

Figure 31 Gusset for rear vertical member of the test stand illustrates most of the details of the frame’s construction

The frame of the stand is made of 2”x2”x0.25” 6061-T6 square aluminum tubing and consists of an upper member that spans the full length of the test stand. It is mounted on two legs made of the same material. The legs are bolted using a combination of 3/8” and 1/2” SAE Grade 5 and Grade 8 bolts to the upper member using gussets made from 0.25” thick 6061-T6 plate. To better withstand side loads, channel sections (made from cut-down 1” x 2” x 0.125” 6061-T6 rectangular tubing) are bolted onto the gussets. Bolted joints were used instead of welds to allow for disassembly if required and to avoid

having to weld the frame together. The upper beam of the frame has in addition to the C-channel for the blade-off arrestor, two hangars used for mounting the nacelle and a length of 80/20 T-slotted tubing that used as a mounting base for the bending beam thrust transducer. Plates for mounting the pylon were installed on the two vertical members.

5.2.3.4 Nacelle and Pylon

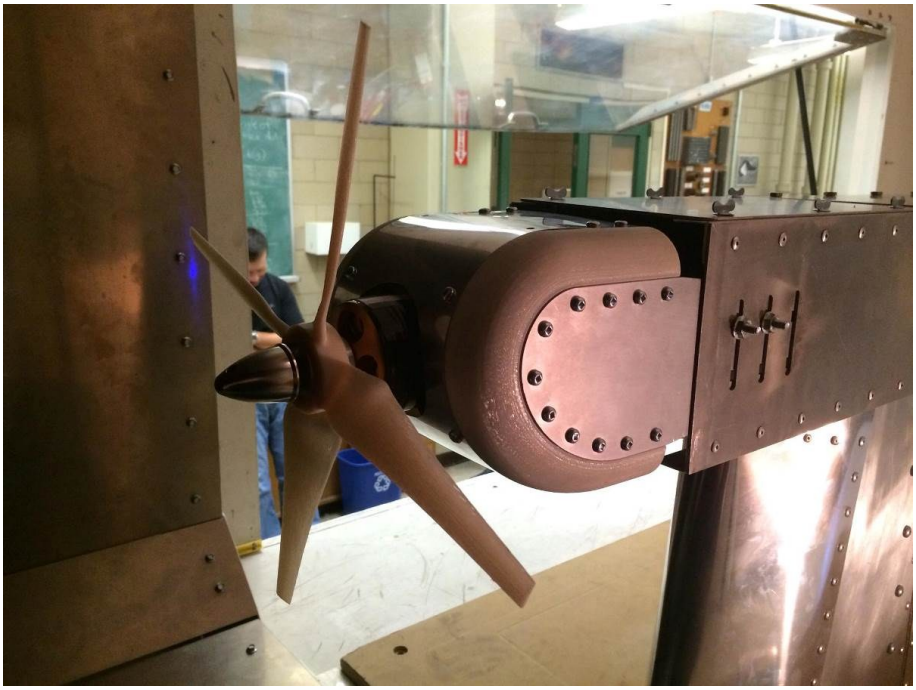

Figure 32 Nose-cone, nacelle and pylon

As shown at Figure 32, the nacelle and pylon are non-structural and serve only as aerodynamic fairings and to house the instrumentation. They are attached to the frame with slotted shear clips and can be moved as needed for alignment. The nacelle is made of 0.050" and 0.080" thick skins made from 3003-H14 aluminum attached to longerons, which are lengths of 1" x 1" x 0.063" 6063-T5 architectural angle. The skins that make up the sides and cover the top and bottom of the rear of the nacelle are riveted to the

longerons with blind rivets. The skins at the top of the nacelle are attached with removable fasteners so that they can act as access panels

The smaller access panel at the front was attached with size DZUS D4-style quarter turn fasteners with wing-headed studs to allow easy access to the measurement head without the need for a tool. The receptacles for the DZUS fasteners were riveted on the upper flange of the upper pair of longerons. The rear upper skin was attached to upper longerons with AN4 aircraft bolts and MS21059 floating nut plates.

The pylon was manufactured from 0.125" and 0.08" 3003-H14 and 6061-T6 aluminum panels. A rounded nose made of a 0.020" Alclad 2024-T4 skin (with two 0.050" 3003 ribs inside to give the nose form) was installed on the front of the pylon to let air flow smoothly around the sides. The pylon has outward-opening doors on both sides to allow access to the instrumentation area between the forward and aft vertical members of the frame. The doors swing on piano hinges and are each secured by four DZUS fasteners. For smooth airflow around the rear the pylon and simplified manufacturing, tapered panels bent in approximately 10-15° increments to a 30° angle are installed.

5.2.4 Test Stand Design and Construction Details

5.2.4.1 Water-Jet Cutting and CNC machining

Due to time constraints related to the test facility, the test stand needed to be manufactured as quickly as possible. This was accomplished by the use of water-jet cutting for as many of the components as possible, including skin panels for the nacelle

and pylon, the blade-off arrestor arms, and parts of the frame and measurement head. Water-jet cutting enabled most of the rig to be assembled quickly and easily through the reduction of touch labour (parts needed to be only de-burred before assembly rather than manufactured from scratch) and slots for bolt and screws instead of holes (where acceptable) could be easily manufactured. The use of slots permits minor misalignments between parts and reduced the need to obtain precise bend radii in sheet metal parts, and better accommodated distortion in parts from welds. Water jet cut parts also acted as drill guides when fabricating parts of the nacelle or pylon that were not water jet cut, thus eliminating the need to lay out hole patterns on these parts. While mechanically fastened joints for any "primary" (load-bearing) structure, tack-welds were also used to hold a few key brackets needed for mounting pylon and cowling structures.

Computer numerical controlled machining was used for manufacturing the torque and thrust transducers to achieve high dimensional tolerances and to reduce touch labour. Machining also allowed for fully interchangeable spare parts to be quickly produced in the event that a transducer was irreparably damaged.

5.2.4.2 Standard Aircraft Hardware

A large quantity of aircraft-grade hardware was used for the assembly of the measurement head. The use of 3/16" diameter bolts (AN3) and structural machine screws (MS24649) allowed for the size of components (such as the torque cell) to remain small while maximizing the clearances for wrenches and hands during assembly. Aircraft grade washers (AN960) in both thick and thin variants were also used as they had a smaller footprint than typical "hardware store" washers.

5.2.5 Instrumentation

The test stand would be useless without accurate instrumentation. To measure the thrust and torque of the propeller, strain gauges were installed on the thrust and torque transducers so that the voltage changes corresponding to thrust and torque measurements could be sensed using analog-to-digital converters (ADCs). The ADCs were interfaced with Arduino microcontrollers and then connected to a PC that recorded the signals for data analysis.

5.2.5.1 Strain Gauge Installation

Four strain gauges orientated in a full Wheatstone bridge were installed on both the bending beam and torque cell transducers. The use of full Wheatstone bridges maximized the voltage difference sensed when a load was applied to either transducer which was beneficial when attempting to measure the low thrust and torque values associated with the propeller. The use of a full bridge also meant that the strain gauges could be arranged so that they would compensated for temperature effects due to passing an electrical current through a tiny wire, permitting them to be sensitive only to the forces they were supposed to measure.

The strain gauges were installed on the thrust and torque transducers following orientations provided in [102]. A pair of Vishay CEA-XX-250UN-350 strain gauges were installed on both the upper and lower surface of the thrust transducer, with all gauges orientated to be parallel to the longitudinal axis of the transducer (Figure 33). Two Vishay CEA-XX-250UW-350 strain gauges, which have three individual gauges on a single package, were used on the torsion cell (Figure 34). These were located 180° apart

and beside the centerline of the cell. Gauges were bonded to the transducers with 5-minute epoxy after the metal had been lightly sanded with fine grit sandpaper and the metal had been cleaned using acetone

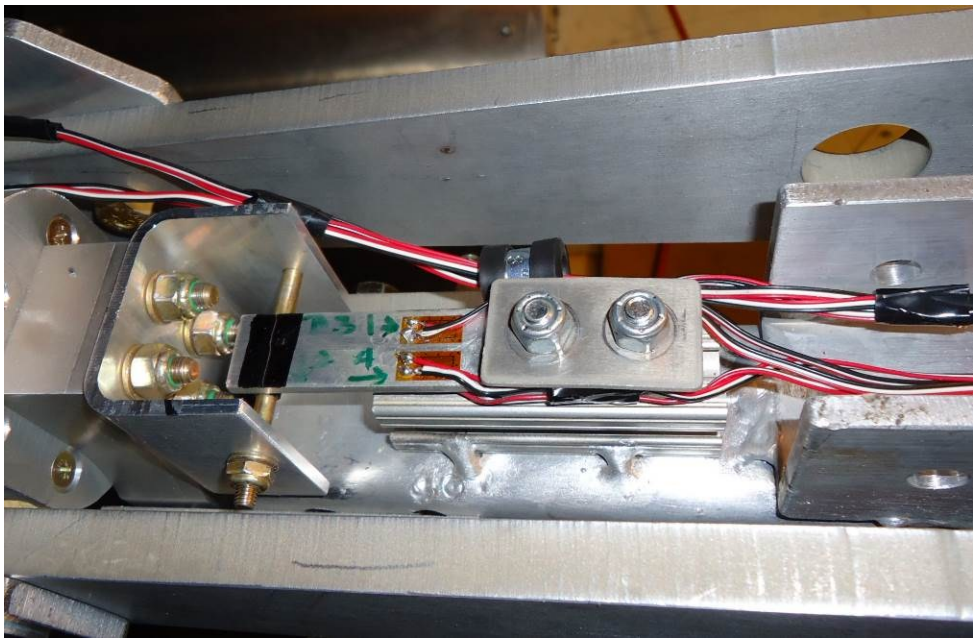

Figure 33 Bending-beam thrust transducer with strain gauges installed

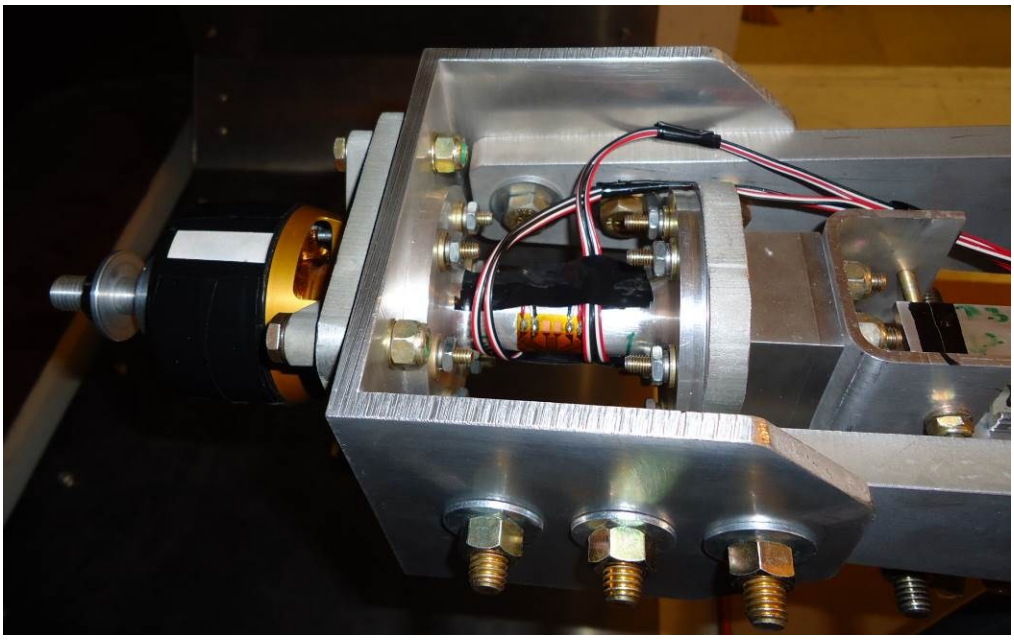

Figure 34 Torque Cell with strain gauges installed

5.2.5.2 Measuring Strain Gauge Voltages

A Linear Technologies LTC2400 analog-to-digital converter was used for reading the voltage shift across the strain gauge bridge. The LTC 2400 was used in a circuit based on one designed by Linear Technologies intended for reading 4-arm 350 ohm Wheatstone bridges (Figure 35) [103]. The circuit as designed use a LT1043 capacitor block as a filter, a LT1050 operational amplifier (or op amp) configured as a non-inverting amplifier with a gain of 101, and a LTC2400 24-bit A/D to convert the analog signal to a digital signal in a 3-wire Serial Peripheral Interface (SPI) format, which was then read by an Arduino Duemilanove. Some changes were made: the LT1050 op amp was substituted with an on-hand Analog Devices OP177 op amp and increased gain to 2136 through changing R2 to a combined resistance of 474 kΩ and R1 to 2.1 kΩ. Two bench-top precision variable laboratory power supplies set to 8VDC were configured to provide +8/GND/-8 VDC power supply to most of the circuit. This voltage was slightly higher than the circuit was designed to operate, which was +5/-5V, but was well within the safe operating voltage of all of the components. The change to +8V was done so that sufficient voltage was available to power the voltage reference in a +5V precision supply. This power supply was based on one included in an instrumentation circuit designed by Analog Devices [104, p. 4.11] and was included to provide a stable power supply for the strain gauges and ADC. The +5V precision power supply used a LT1236-5 +5V voltage reference connected to an OP177 op amp configured as a negative-feedback amplifier with no gain that provided a voltage to the base of a 2N2219A NPN transistor. The op amp would sense the emitter voltage of the transistor and adjust the voltage provided to

the base so that the output of the power supply was held at a constant 5V. As the collector of the transistor was supplied with +8V and the op amp was supplied with +/- 8V the power supply was able to provide a stable +5V supply regardless of the current draw of the strain gauges and the LTC 2400.

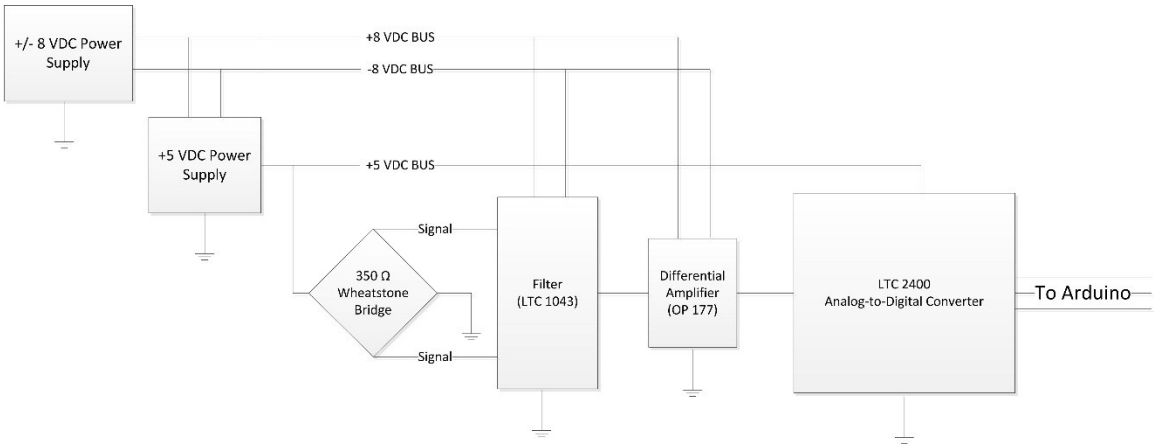

Figure 35 LTC 2400 – based data acquisition system

5.2.5.3 Calibration

Both the thrust and torque cells were calibrated prior to use. This was completed by using weights to simulate the expected thrust and torque and recording the voltages read by the ADCs. By correlating the applied thrust or torque to the read voltage the calibration curve needed to interpret test data was created.

The thrust force was simulated pulling axially on the shaft of the motor using a pulley and weights up to 22.73N were applied in 2.2N increments (see Figure 36). Three loading cycles were completed and the thrust calibration data was analyzed with the methods discussed in section 6.6 and the voltage readings at each load were fitted with a third order polynomial trend line (Figure 37). It was noticed that the direction of loading

had some influence on the read voltage, as at each load the readings for when weights were being applied or removed were tightly grouped. Therefore, the direction of loading needed to be taken into account when interpreting test data. The two separate distinct trendlines suggests that the transducer did not return to its no-load position, possibly due to friction or perhaps mechanical damage.

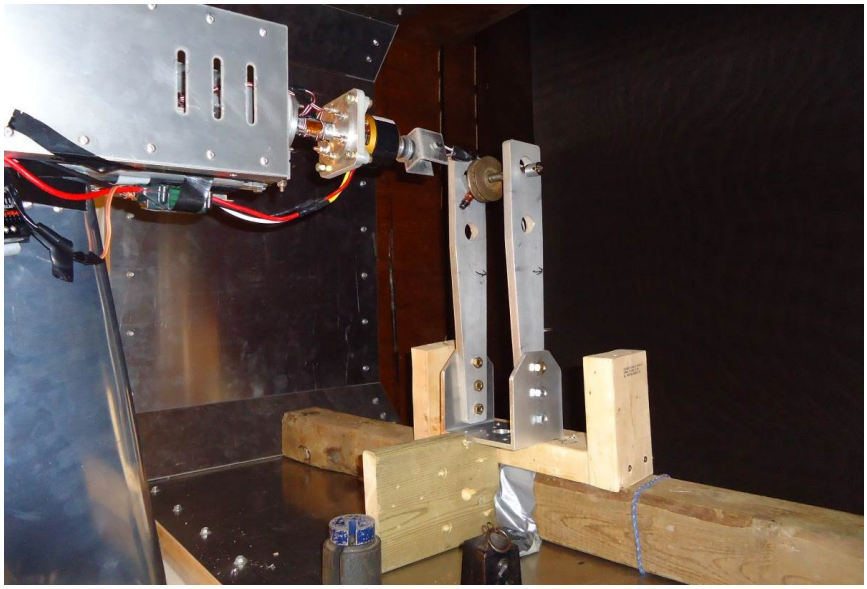

Figure 36 Calibration of the thrust cell

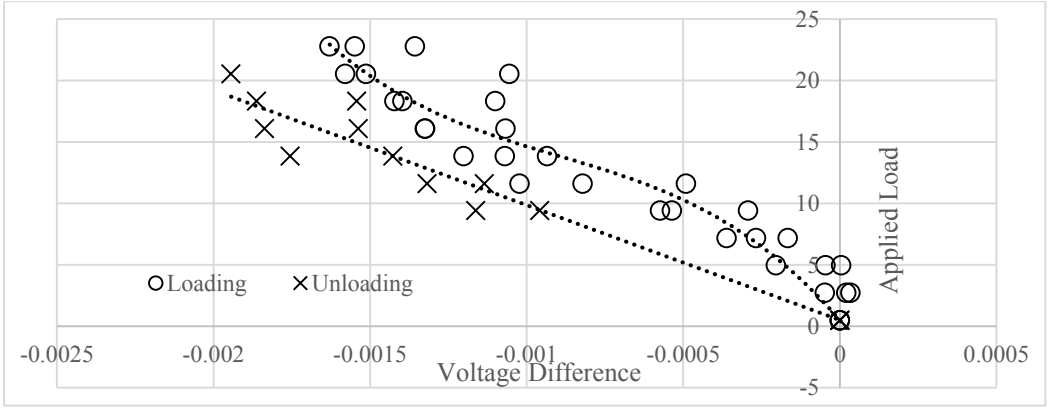

Figure 37 Thrust cell calibration data

The torque cell was calibrated by hanging weights on a moment arm attached to the motor-side face of the torque cell. The moment arm was a standard 9/16" crescent wrench, the open head of which was fitted around 3/8" bolt welded to a steel adaptor plate. The wrench had a moment arm of 15cm when fitted to the adaptor plate, and weights up to 20.6N were applied in 2.2N increments for a maximum torque of 3.0 Nm. The calibration data (and actual test data) were both unusable for a variety of reasons as is fully discussed in 7.1.3.1

5.2.6 Tunnel Calibration

To evaluate the effects of the test rig and wind tunnel on the performance of the propeller, a calibration run was completed. As will be further explained in 6.4, due to the poor-quality data collected this test was somewhat irrelevant as the instrumentation had serious voltage drift issues, the test method was flawed, the torque transducer lacked the sensitivity to be able to measure the propeller's torque, and good reference data was unavailable.

5.2.6.1 Effect of Test Stand

As previously discussed, objects in front of and behind the propeller disc affect the thrust produced by the propeller. These affects can be quite significant as descirbed by Weick [16, pp. 146-147]. To investigate the effects of the nose cone, nacelle and pylon a propeller that had been tested in another wind tunnel was to be mounted and spun on the test stand. Small propeller wind tunnel test data is available from the University of Illinois Propeller Database [89] . The APC 11x7E, as it was approximately the same diameter as both test propellers and available, was used for this purpose. This propeller

was spun at 3000 and 4000 RPM at tunnel wind speeds of 25 and 35 km/h but no useable data was obtained. This was likely due to the thrust and torque transducers being incapable of measuring the low amounts of thrust generated at these speeds and due to drift in the signal. None of the other propellers listed in the database were on-hand so the decision was made to use an APC 20x13 propeller. This propeller is considerably larger than the test propellers but due to its size, it generated useable readings. The estimated performance data for the APC 20x13 is available from APC [105]. To check the validity of this data, the estimated performance of a similar propeller (the APC 19x12) was compared to its test data. The test data of the APC 19x12 was collected with the propeller running at a constant rotational speed of 3007 RPM and was corrected for tunnel effects [89]. The estimated and actual power coefficients closely agree; however, the thrust coefficient is larger and changes with respect to advance ratio much more than predicted, resulting in a poor agreement

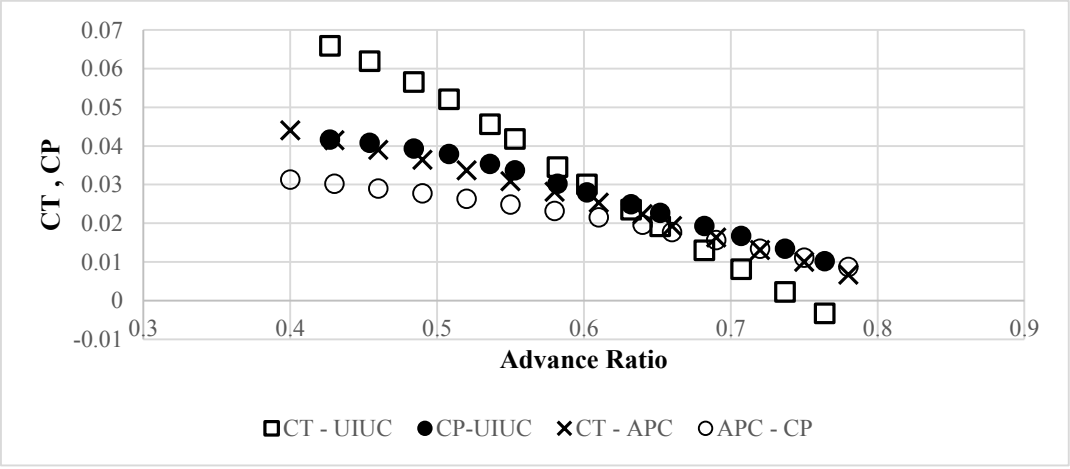

Figure 38 APC 19x12 Wind tunnel test results from UIUC compared to predicted data

Useable test data was obtained for only two unique advance ratios and at a single wind speed, making it impossible to evaluate the effect of the nacelle on the performance

of the propeller. This was due to the thrust transducer jamming, which made it send a constant signal until the motor was shut down at the end of the test and the measurement head returned to its no-load position. The load cell jammed at a setting that was outside the range of calibration and registered such an erroneous value it was unusable. For the two usable data points obtained, the propeller produced twice the thrust predicted.

One possible correction that could be applied to compensate for the effects of the test stand is to assume that the test rig is typical of the geometry of a nacelle and then find the corrected advance ratio, using the equation [100, p. 384]:

$$J_{corr} = J\left(1 - 0.329\frac{S_c}{D^2}\right) \quad \textbf{Eq. 66}$$

Where:

J_{corr} = corrected advance ratio

J = advance ratio

S_c = maximum cross-sectional area of the cowling immediately behind the propeller

D = propeller diameter

This correction to the advance ratio accounts is based on historical data and is intended for use during the preliminary design of an aircraft to estimate the installed thrust of the propeller. While this approximation is useful for aircraft design purposes, it would be inappropriate to apply it to results from the test rig as this correction is for typical engine nacelle (the geometry of which is unclear, given the wide range of nacelle designs that have been employed on aircraft) and not the test rig.

5.2.6.2 Wind Tunnel Interference

When a propeller is run in a wind tunnel its wake will disturb the flow produced by the tunnel fan [106, p. 222]. This disturbance results in the propeller generating the same thrust and torque it would outside of the wind tunnel at a lower airspeed [106, p. 222]. To estimate the equivalent free airspeed, [107, p. 14] provides a tunnel interference correction factor (originally presented in [108]).

The equivalent free air speed, V' is calculated as:

$$V' = V\left[1 - \frac{a}{2}\frac{\tau}{\sqrt{1+2\tau}}\right] \quad \textbf{Eq. 67}$$

with

$$\tau = \frac{T}{\rho A V^2} \quad \textbf{Eq. 68}$$

Where:

V = tunnel air speed [m/s]

a = the ratio of the propeller disc area to the tunnel cross-sectional area

τ = disc loading

T = thrust [N]

A = propeller disc area [m^2]

ρ = air density [kg/m^3]

As the tunnel velocity increases (or the thrust decreases) the tunnel interference effects diminish. Based on the tunnel air speeds used for performance tests and the

calibration range set for the thrust cell, the equivalent free airspeed is presented in Table 11. At most tunnel speeds the thrust generated by the propeller did not significantly change the advance ratio of the propeller.

Thrust	Equivalent Free Airspeed at Tunnel Wind Speed			
	14.2	25	35	40
[N]	*[km/h]*	*[km/h]*	*[km/h]*	*[km/h]*
0	14.2	25	35	40
1	14.0	24.9	34.9	39.9
2	13.9	24.8	34.8	39.8
3	13.9	24.7	34.8	39.8
4	13.8	24.7	34.7	39.7
5	13.7	24.6	34.7	39.7
6	13.7	24.5	34.6	39.6
7	13.6	24.5	34.6	39.6
8	13.6	24.5	34.5	39.5
9	13.6	24.4	34.5	39.5
10	13.5	24.4	34.4	39.5
11	13.5	24.3	34.4	39.4
12	13.5	24.3	34.4	39.4
13	13.4	24.3	34.3	39.4
14	13.4	24.2	34.3	39.3
15	13.4	24.2	34.3	39.3
16	13.3	24.2	34.2	39.3
17	13.3	24.2	34.2	39.2
18	13.3	24.1	34.2	39.2
19	13.3	24.1	34.1	39.2
20	13.2	24.1	34.1	39.1
21	13.2	24.0	34.1	39.1
22	13.2	24.0	34.1	39.1
23	13.2	24.0	34.0	39.1

Table 11 Equivalent Free Airspeed at tunnel wind speed

5.3 Shroud

5.3.1 Overview

The containment shroud (Figure 39) was included for the purpose of stopping an ejected blade or reducing the kinetic energy of an ejected propeller blade to a level that, should it strike something, would not result in serious injury or damage. Non-lethal projectiles may not impart more than 12 J/cm^2 [1], and given the knife-like geometry of most propeller blades there is little chance of imparting less than this amount. The shroud was 24” deep, 42” tall and 57” wide and was sized to occupy as much of the cross section of the wind tunnel as possible to reduce further tunnel blockage effects. The shroud is consists of panels of 0.125" 5052-H32 bolted to built-up frames of 3"x1.5"x 3/16 or 1/4” 6061-T6 C-channel extrusion.

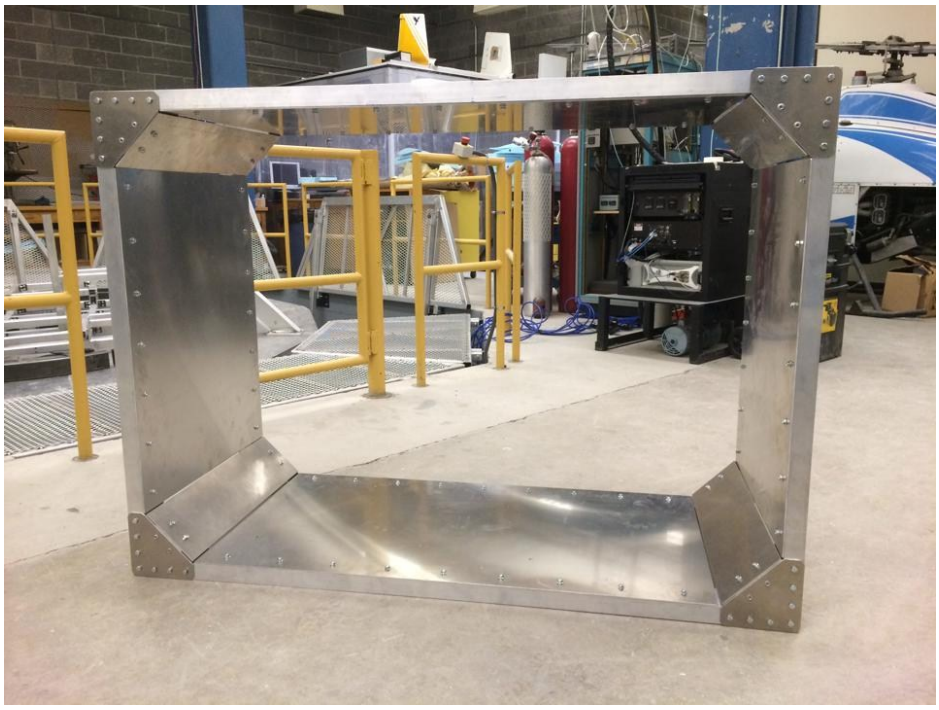

Figure 39 Containment Shroud

5.3.2 Shroud Testing

While the size of the C-channel was selected as it allowed for good wrench and hand clearances during assembly/disassembly, the thickness of the panels was chosen through material testing to avoid penetration if struck by an ejected propeller blade.

5.3.2.1 Kinetic Energy of an Ejected Propeller Blade

The energy of an ejected propeller blade was estimated for a worst-case scenario based on the following assumptions:

- The average propeller has a diameter of 16” (0.406 m) and the same geometry as an APC 14x4W propeller. The blade of an APC 14x4W is wide, thin and knife-like in appearance, making it have much more kinetic energy that other narrower blades
- The propeller is made of a polymer with a specific gravity of 1.2, which corresponds to the specific gravity of Duraform HST
- The propeller is spinning at 7500 RPM when it separates from the hub at the root the blade
- When the blade separates from the hub, the energy of the blade when it was rotating becomes kinetic energy and the blade moves axially away from the hub
- After the blade separates from the hub it is not effected by any external forces (such as aerodynamic drag)

The kinetic energy associated with a rotating mass, E_R, can be calculated by the equation

$$E_R = \frac{1}{2} I \omega^2 \quad \textbf{Eq. 69}$$

Where:

I = mass moment of inertia [kg m^2]

ω = rotational speed [rad/s]

The mass moment of inertia of the blade is calculated as the sum of the mass moments of inertia of each segment of the blade. The mass moment of a blade segment is:

$$\Delta I = \frac{\Delta M \Delta r}{12} \quad \textbf{Eq. 70}$$

Where:

ΔM = mass of the blade segment [kg]

Δr = length of the blade segment, which is taken as the distance between two consecutive blade stations [m]

$\bar{r}$ = the distance from the axis of rotation of the propeller to the centre of gravity of the segment of the blade [m]

When the propeller blade separates, the blade goes from rotating to translating motion. The kinetic energy of the blade undergoing translating motion, E_T, is:

$$E_T = \frac{1}{2} M v^2 \quad \textbf{Eq. 71}$$

Where

M = mass of the blade [m]

v = velocity of the blade [m/s]

Equating the energy associated with the rotating motion to the blade's translating motion, after ejection the blade will have a velocity, axially away from the hub, of:

$$\Delta I = \frac{\Delta M \Delta r}{12} + \Delta M \bar{r}^2 \quad \textbf{Eq. 72}$$

The chord and thickness of the blade of an APC 14x4W propeller was measured and used for calculating the moment of inertia and mass of the blade. It was assumed that the cross-sectional area of an airfoil is [30, p. 36]:

$$A = 0.656bh \quad \textbf{Eq. 73}$$

Where

b = chord length of the airfoil [m]

h = overall thickness of the airfoil [m]

The propeller blade under the described conditions was estimated to have a mass of 54.7g and 216J of energy when it is rotating at 7500 RPM. If the blade were to be ejected from the hub it would travel at an initial velocity of 122 m/s.

5.3.2.2 Drop Tower Testing

Testing was conducted initially with an Instron 8200 drop tower on 0.125" 6061-T6 plate, which was initially selected for shroud panels. 1/2" plywood, ½" Lexan, and stacked multiple layers of 0.020" 2024-T4 aluminum were also tested, but the 0.125" aluminum panels were selected on the basis that they could take multiple impacts without the need for replacement, 0.125" material is readily available for patches or replacement panels, and the material is inexpensive and easy to work with. Samples were impacted with a hemispherical instrumented indentor (tup) at a speed of 4.4 m/s and 132J of energy. This speed and kinetic energy were at the limits of the tower but still much less than the energy of the ejected propeller blade. The tup also had several limitations as it did not represent the actual shape of the propeller, had a fixed-trajectory, and could not deform. While an unyielding tup being forced into the material represents a worst-case scenario, the rounded head distributed the force and energy over a much greater area (it has a diameter of 25mm) than the pointed tip of a propeller blade would.

The specimens were also rigidly clamped around their edges to a rigid steel frame, with only a 0.15m x 0.15m (6" x 6") area able to deform. This a more extreme mounting case than what would be seen by the shroud, where the large panels in an impact would likely flex to absorb more energy before penetration by the blade would commence. Regardless of these differences, the 0.125" aluminum performed well as it required an average 8 to 10 impacts for penetration. After a single impact the metal showed no signs of cracking, typically displaying only a dent approximately 12 mm deep.

5.3.2.3 Ballistic Pendulum Testing

The material for panels was changed during manufacturing from 6061-T6 to 5052-H32 of the same thickness as this alloy is less expensive and comparable in strength. To verify the material substitution was appropriate and to evaluate the material's performance at the expected speed and energy of a propeller blade strike, a ballistic pendulum test was conducted that allowed for higher-energy impacts with an actual propeller blade striking the metal. Propeller blades were mounted to a freely swinging arm which, when struck by a projectile, would strike samples of the 5052-H32 panel with a propeller blade. The ballistic pendulum test was meant as a preliminary confirmation of the suitability of the panels and should by no means be considered as an exhaustive characterization of propeller blades striking 0.125" 5052-H32 aluminum. While a proof test of the shroud could have been conducted where an intentionally-damaged blade was spun with the intention of it breaking, this test allowed for a high-energy impact without the risk of unnecessarily damaging the shroud or the relatively-expensive brushless DC electric motor.

Figure 40 Ballistic Pendulum

The ballistic pendulum was struck by a few different projectiles fired at a range of ~30 m. For most impacts, a 17 calibre Hormandy Magnum Round (HMR) (Federal Premium V-SHOK P771) was fired at the pendulum using a Savage 93R17 bolt-action rifle. A single impact test based on a Winchester 1 ounce 2-3/4" target shot was fired from a Mossberg 535 12-gauge shotgun[6]. When fired at the range of 30m, the HMR round has a kinetic energy of 220J [109] , and the target shot had a kinetic energy of 414 J based on a muzzle velocity of 298m/s and the assumption that at least 1/3 of the pellets

[6] All firearms and ammunition were purchased, registered, stored, transported and handled in accordance with federal and provincial laws. Firearms were used under the close supervision and direction of their responsible and appropriately licensed owners in a safe and controlled location.

strike the pendulum [110]. Two different types of propeller blades were also used to strike the samples. For most testing blades cut from an APC 14x4W propeller were used. One impact used a blade cut from an APC 11x7 to evaluate the effects of blade planform. APC manufactures its propellers from a glass-reinforced plastic that is considerably stronger (and less likely to deform) than any 3DP plastic likely to be used for blade construction. Both blades represent the worst-case scenario of a hardened, unyielding propeller blade.

The arm of the pendulum was made from 2" x 2" x 0.125" 6061-T6 square aluminum tubing with one side removed so that it had a C-channel cross-section, and a sacrificial 0.5" aluminum plate was bolted to the front to be struck by the projectile to transfer the energy to the pendulum. Based on the large craters caused by the projectile hitting the sacrificial plate, a portion of the bullet's energy was being absorbed by the plate and not transferred to the propeller blade. However, impacts from a loosely-supported 14x4W or 11x7 blades resulted in some slight damage to the tip of the propeller blade and, at worst, a minor scratch on the test specimen. The tip of the 14x4W blade tended to "mush down" on impact while a few millimeters of the thinner tip of the 11x7 blade were broken off of the propeller.

When a 14x4W blade was butted up against the back of the pendulum and firmly duct taped to the C-channel flange, a small dent was formed in the specimen. Based on an examination of the deformation created during testing, the dent appeared to be far from the point of penetrating the material due to the lack of stress whitening or cracking. It was concluded that it was unlikely that the blade would ever have been driven into the panels of the shroud

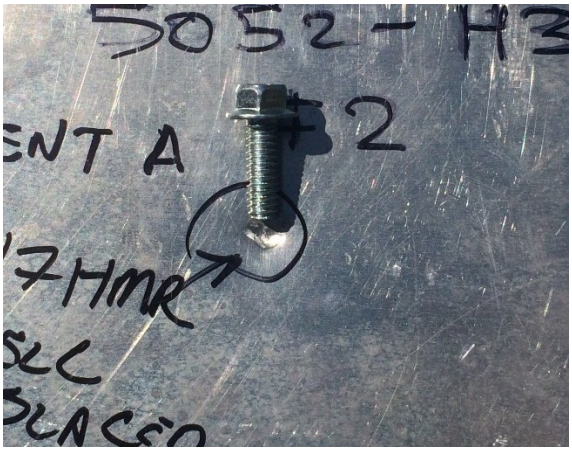

Figure 41 Largest dent obtained from ballistic pendulum testing

Given that the plate on the pendulum was absorbing some of the bullet's energy, one test was conducted where a shotgun shell was fired at the pendulum. It was considered that shotgun round would impart its energy onto a larger area of the plate, which would reduce the amount of deformation and instead transfer more to the propeller blade. The shotgun was also equipped with a holographic red-dot sight, allowing for the gun to be better aimed at the target. To present a larger target, a small piece of 0.125" aluminum was fixed to the arm. A 14x4W propeller blade was attached to the side of the pendulum but was not rigidly fixed. On impact, the propeller blade bent the plate inward and then ricocheted approximately 5 meters away from the pendulum. Examination of the specimen showed only a small scratch but no other damage. The plate attached to the arm was severely dented inwards, but the tight grouping of marks from the pellets indicated most of the shotgun round had impacted the pendulum, likely imparting more than the estimated 414J.

Overall, it was assessed that the combination of drop tower and ballistic pendulum testing had confirmed that the panels were of sufficient thickness to stop an ejected propeller blade.

6 Chapter: Process Testing

6.1 Introduction

It would be impossible to conclude that the proposed propeller design process works without realistic testing. To do this, the design program was used to design a propeller for a small UAV, which was then manufactured using 3D printing and testing in simulated flight conditions in a low-speed wind tunnel using the test rig and instrumentation described in Chapter 5.

6.2 Overview of Testing

One major constraint of the simulated flight testing was the maximum speed of 40 km/hr (21 kts) permitted in the wind tunnel. As most 20-35 kg small UAVs tend to fly at speeds greater than this, the propeller was designed for a 5 kg Senior Telemaster. The Senior Telemaster (Figure 42) is a RC aircraft widely used, including at Carleton University, as a test bed for UAV autopilots and systems. Key design features of the aircraft are detailed in Table 12 and were taken from **[109]**. One Telemaster at Carleton was equipped with an e-flite Power 60 brushless DC motor driving an APC 14x10 propeller. However, since an AXI Gold 5325/18 motor had been acquired for the test rig the propeller was designed around this motor instead. There are some slight differences in between the specifications (Table 13) and performance (Figure 43 and Figure 44) of the two motors, but the AXI Gold 5325/18 is appropriate for the aircraft.

Figure 42 Senior Telemaster

Mass, m	[kg]	5
Ref. Wing Area, Sref	[m^2]	0.858
Wing Span, B	[m]	2.3368
Aspect Ratio		6.364
Parasite zero-lift drag coefficient, c_{D0}		0.0323
Max. lift coefficient, no flaps deployed, C_{LMAX}		1.4000
Oswald Efficiency		0.9
Aircraft Lift Slope, a	[cl/deg]	*0.0761*

Table 12 Estimated Aerodynamic Properties of the Senior Telemaster

		AXI GOLD 5325-18	e-flite Power 60
KV	[RPM/V]	308	400
No-Load Current	[A]	1.7	2.7
No-Load Current Voltage	[V]	20	10
Maximum Voltage	[V]	29.2	28.8
Maximum Continuous Current	[A]	65	55
Peak Current	[A]	80	65
Winding Resistance	[ohm]	0.032	0.05
Winding Resistance @ Temperature	[Deg C]	25	25
Max Rated Temperature	[Deg C]	130	100

Table 13 Specifications of AXI Gold 5325/18 and e-flite Power 60 motors

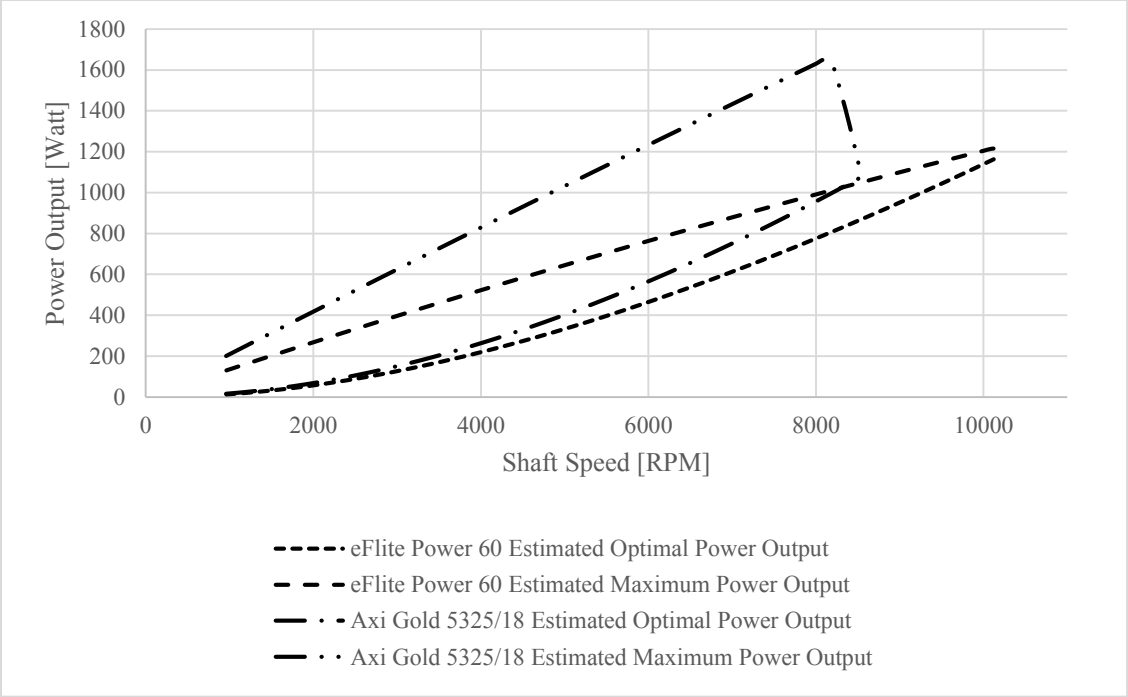

Figure 43 Estimated Performance of the Axi Gold 5325/18 & e-flite Power 60 Brushless DC Motor

Based on the performance methods detailed in appendies A and B and the data available from [109] and [110], the performance of the aircraft and motor were analyzed. It should be noted that the drag polar for the aircraft was not available but was created based on estimates of the aircraft's drag provided in [109]. As a result, the parasitic drag coefficient were set to closely mirror the drag and neither may be the exact value for production aircraft. The conditions used when determining the normal and maximum thrust are summarized in Table 14, Table 15 and Table 16. After testing it was noticed that the propeller was designed to meet unrealistic requirements as it had been designed to produce enough thrust for the aircraft to constantly climb at 400 fpm. This is far from a level flight condition, and unless the aircraft was designed to fly in high headwinds, extreme turbulence, or a constant turn demanded far too much thrust from the propeller. The maximum climb rate of 1181 fpm was also far too extreme for the aircraft. Based on some brief performance calculations, it was found that, at the two operating conditions

seen in testing, the propeller was designed to provide the thrust needed for a 17kg version of the aircraft rather than the intended 5 kg version.

		Typical	Operating Limits
Desired Take-off Distance	[ft]	98	98
Head (+) /Tail (-) wind component	[kt]	-5	-18
Obstacle Height	[ft]	50	50

Table 14 Typical and Maximum Take-Off Performance

Desired Rate of Climb		
Desired Climb Speed	[KTAS]	19
Desired Rate of Climb	[fpm]	787
Maximum Rate of Climb		
Recommended Best Climb Speed	[KTAS]	19
Max Rate of Climb, based on NRT T/O Power	[fpm]	1009
Max Rate of Climb, based on MRT T/O Power	[fpm]	1461

Table 15 Climb Performance

	Typical Operating Conditions			Operating Limit Conditions		
	Speed* [KTAS]	Minimum Wind Speed [kt]	Minimum Rate of Climb [fpm]	Maximum Head Wind [kt]	Max. Rate of Climb [fpm]	Maximum Bank Angle* [deg.]
Best Endurance	19	---	400	11	1181	0
Best Range	23	4	400	11	1181	45
Carson Speed	50	4	400	11	1181	82
Desired Ground Speed	33	0	400	11	1181	71
Desired Maximum Speed	68	0	400	11	1181	86

Table 16 Cruise Performance

6.3 Propeller Design

Based on the performance scores the design program was directed to make a propeller with its optimal performance at low speeds that could be easily obtained in the wind tunnel. The airspeed, normal and maximum thrust and flight phase ranking are shown in Table 17.

Phase of flight	Speed [KTAS]	Normal Required Thrust [N]	Maximum Required Thrust [N]	Performance Score
Take Off (at 70% rotation speed)	13	39.53	53.47	3
Desired Climb	19	23.85	23.85	2
Maximum Climb	19	29.93	41.43	4
Max Endurance	19	14.45	23.15	3
Max Range	23	12.73	16.69	5
Carson Speed (Design Cruise)	50	15.52	17.95	2
Desired Ground Speed	33	11.65	11.44	2
Desired Maximum Ground Speed	68	23.85	33.61	1

Table 17 Thrust Requirements and Performance Scores

To reduce cost and lead time the propeller was made from P400 ABS plastic printed on a Dimension 1200 BST FDM 3D printer owned and operated by the Department of Mechanical and Aerospace Engineering. The propeller was designed using airfoil data for the NACA 44xx family of airfoils that was collected for Reynold's numbers between 75,000 and 300,000 using XFOIL 6.3.4 for airfoil thicknesses between 12% and 24%. The diameter was set to be the maximum allowable for the printer bed (13.14") and it was designed with four blades at a nominal integrated lift coefficient at the primary design condition of C_L=0.6. The details of the blade are shown in Figure 44

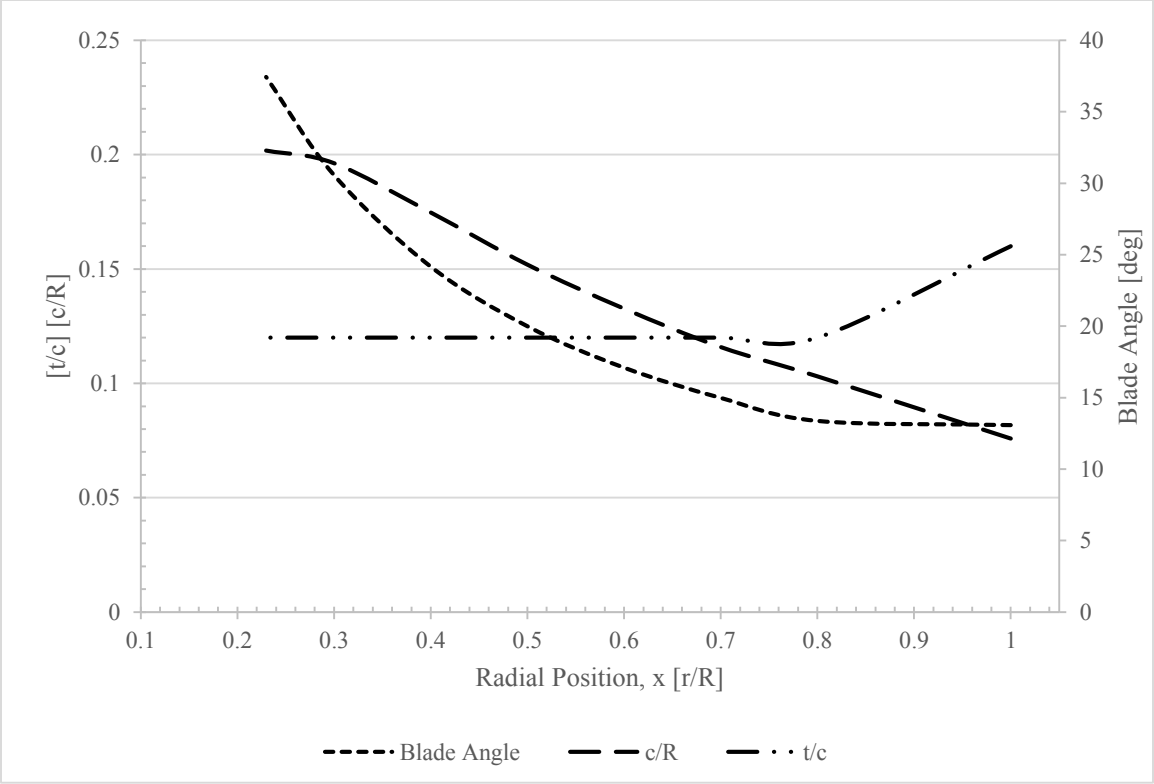

Figure 44 Blade Geometry of Test Blade Propeller

According to the detailed performance calculations, the program determined from its full-blade performance estimating routine that the propeller could only generate the required and maximum thrust for three of the design conditions highlighted in Table 18. However the single point-method showed it was able meet the normal thrust requirements at four operating points Table 19. It should be noted that for one of the operating points, the estimated propeller efficiency using the full-blade estimating program was in excess of 728% due to an exceptionally low power coefficient. During validation checks, it was found both the full-blade and single-point methods accurately predicted the thrust coefficient of the propeller but the single-point method was considerably better at predicting the power coefficient. This discrepancy may be caused by either an error in the program, or a weakness inherent to the estimating method. Borst [17] notes that single-

point methods for propeller performance are often much more robust than those that consider the full blade's geometry or poor aerodynamic data. The single point method was included mainly to provide a second estimate for the user to cross-check the results from the full-blade performance method. In future it would be advisable to incorporate a cross-check into the program to prevent clearly erroneous results from driving design decisions. Regardless of this lack of a cross-check, manufacturing and testing the propeller was still deemed to be a worthwhile exercise as it would provide performance data that could be used for correcting performance calculations.

A final structural analysis check was performed using the structural analysis methods detailed in section 3.6. This check was performed using the air loads that would be encountered when the propeller was operating at 144% of the maximum rated rotational speed of the motor at the average take-off speed and included the first-order harmonic air loads that would be seen if the air entered the propeller disc at a 10° angle from perpendicular to the disc. The structural analysis showed the blade had less than half of the strength at the root that was needed to cope with the expected bending loads. While the propeller had been designed to meet conditions that were expected to represent a highly unlikely worst-case scenario where the airfoils operated at their maximum lift coefficient at 144% of the maximum rated rotational speed of the motor, they were not structurally analyzed for the effects of the blade deflecting due to air and centrifugal loads. The deflection of the blades is not always a major factor in the structural analysis of propellers if the blade is sufficiently stiff. In some references [37] it is entirely neglected and a simple bending plus axial stress approach is used. This however is not a constraint as the motor-combination could only achieve a maximum rotational speed of

~6500 RPM, and in the wind tunnel air enters the propeller disc at an angle much less than 10°, eliminating the additional blade loading due to the Aq factor.

6.4 Propeller Manufacturing

Two propellers were manufactured (Figure 45), with less than optimal quality and obvious manufacturing flaws. To maximize the printed bed, each propeller was printed such that the blades would span the diagonal of the printer bed. This was a different orientation than was used for manufacturing test blades, or a single propeller blade and hub. While the quality of a test blade printed at a similar size and settings was superb, the actual trailing edge of the propeller had many voids large enough to allow air to pass through from the lower to upper surface (Figure 46). This defect would reduce the propeller's thrust by effectively shortening the chord of the propeller. While the program's trailing edge correction feature, which adds additional material to the trailing edge of the blade to prevent this defect, worked nearly flawlessly for the test blades, it failed to add sufficient material to the trailing edge on the actual propeller. The cause of this is likely due to the printer head needing to move in two directions (X & Y) rather than just one direction when the blade is orientated vertically or horizontally. To mitigate the aerodynamic effects of the voids, the upper and lower surfaces of the blades on one propeller were lightly covered with 5-minute epoxy to fill the voids. After coating, the surfaces were sanded for balancing and to provide a more smooth and consistent surface finish. The overall increase in the propeller's mass due to epoxy was 3.62g, and the increase in the centrifugal force of each blade due to this additional 0.9g of mass is trivial. However, due to the defects and uncertainties as-manufactured structural strength

versus the design strength of the blades, it was decided that the propellers would be tested at much less than their maximum design speed.

Figure 45 As-manufactured test propeller

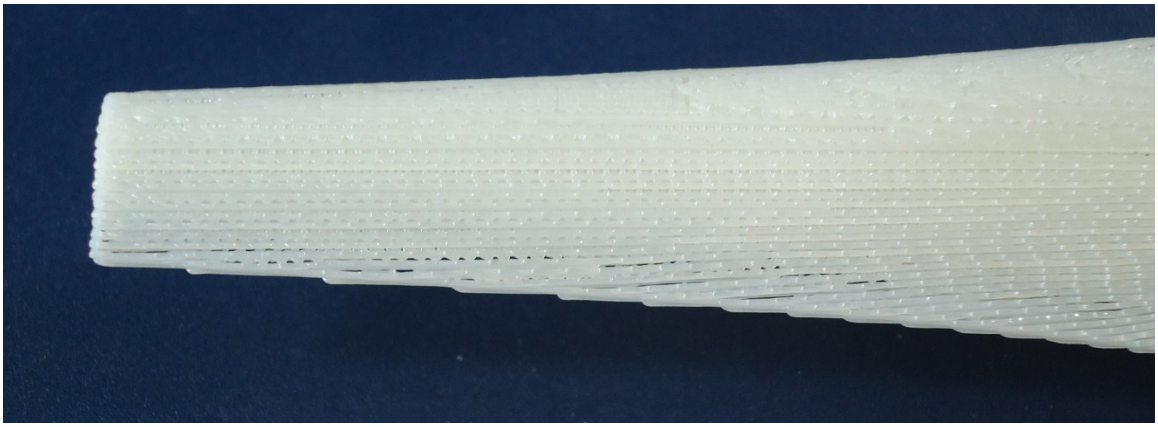

Figure 46 Voids at the trailing edge of the blades. The chord of the tip is approximately 17mm.

	Speed [KTAS]	Design Thrust [N]	Rotational Speed [RPM]	Advance Ratio	Delivered Thrust [N]	Propeller Power [W]	Electrical Power Required [W]	Propeller Efficiency [%]	Overall Efficiency [%]	Performance Weight	Score	MRT Possible?
Maximum Endurance	19	14.45	4200	0.3593	14.74	120	144	76.01	100.46	3	301	Yes
Maximum Range	23	12.73	4000	0.4190	12.96	94.1	118	82.24	127.84	5	639	Yes
Desired Ground Speed	33	11.65	3800	0.6790	14.93	21.0	39.4	728.60	644.22	1	644	Yes

Table 18 Predicted propeller performance using full blade analysis method

	Speed [KTAS]	Design Thrust [N]	Rotational Speed [RPM]	Advance Ratio	Delivered Thrust [N]	Propeller Power [W]	Propeller Efficiency	MRT Possible?
Maximum Endurance	19	14.47	4300	0.4095	14.47	227	55.93	No
Maximum Range	23	12.58	4000	0.5237	12.58	208	63.26	No
Carson Speed (Design Cruise)	50	20.33	5000	0.9263	20.33	614	75.86	Yes
Desired Ground Speed	33	11.59	3800	0.8041	11.59	239	74.05	Yes

Table 19 Predicted propeller using full-blade analysis method

6.5 Propeller Performance Testing

6.5.1 Initial Propeller Testing

Prior to testing the propellers in the wind tunnel, a brief static run-up was conducted to verify the blades had sufficient strength. To avoid damaging the wind tunnel test rig, the propeller was first tested outdoors on a stand made of pressure-treated 4" x 4" lumber and spruce 2" x 3". The as-printed propeller was run at rotational speeds between 1800 and ~5500 RPM for a period of approximately 20 minutes. It was noted after the test that small hair-like strands of the ABS plastic appeared at the tip of the blades. These hairs were likely due to the centrifugal forces stripping short, loosely-bonded beads of plastic off the blade. Inspection of the blades did not show any cracking or signs of imminent failure such as stress whitening or crazing that is found during polymer material testing proceeded specimen failure. After a few hours of wind tunnel testing it was noticed that the hairs stopped appearing at the tips of the blades.

6.5.2 Wind Tunnel Testing

Based on the speed limitation of the wind tunnel, the propeller was performance tested at speeds of 14 km/h (7.5kt), 25 km/h (13.5kt), 35 km/h (18.9 kt), and 40 km/h (21.6 kt)[7]. The 14 km/h wind speed does not correspond to any particular aircraft speed but was the wind tunnel's start-up wind speed. This wind speed was used for initial

[7] As the wind tunnel air speed indications were provided in km/h, knots will be listed as a secondary unit to better preserve the accuracy of the test data

testing of the propeller and test rig. The remainder of the wind speeds corresponds with those seen by the aircraft in flight.

6.5.2.1 Test Technique

At each tunnel speed the propeller was run at three throttle settings at least three times. The wireless controller had seven marked “detents” on the throttle including cut off (first detent) and maximum (last detent) as shown in Figure 47

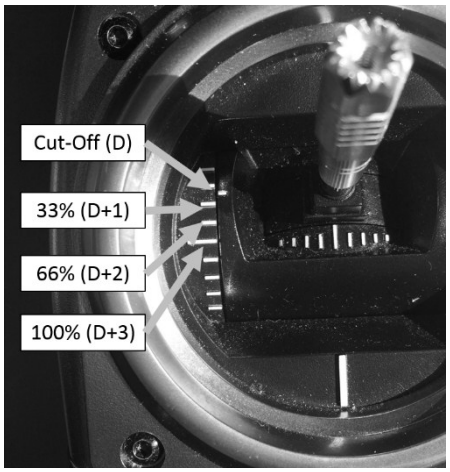

Figure 47 Throttle Detents

Two throttle profiles for completing a “run” - or a set of three increases to maximum power - were used during testing. The wind tunnel tests done with the as-printed blade used a “pyramid” schedule where the throttle was increased from cut-off to D+1, D+2, D+3, then stepped down through D+2 and D+1 before the motor was shut-off. At tunnel speeds above approximately 22 km/h (12kt) the propeller was prone to wind milling and so as a result the tunnel speed needed to be decreased until the propeller stopped. This problem could have been avoided by using the brake feature found on the electronic speed controller (ESC); however, this was feature was not understood during testing. For the epoxy-covered blade and for tunnel calibration a step and drop profile

was instead used – after data had been collected at D+3, the throttle was decreased to a D+1 setting. This procedure avoided the need to change the tunnel speed to stop the wind-milling propeller and resulted in the collection of an equal number of test points at each speed

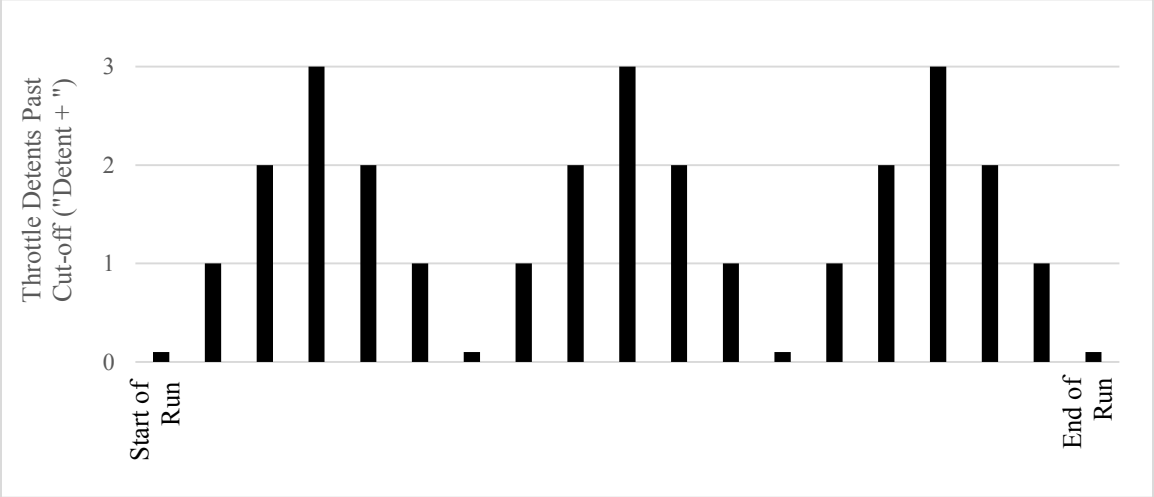

Figure 48 Pyramid-style throttle schedule

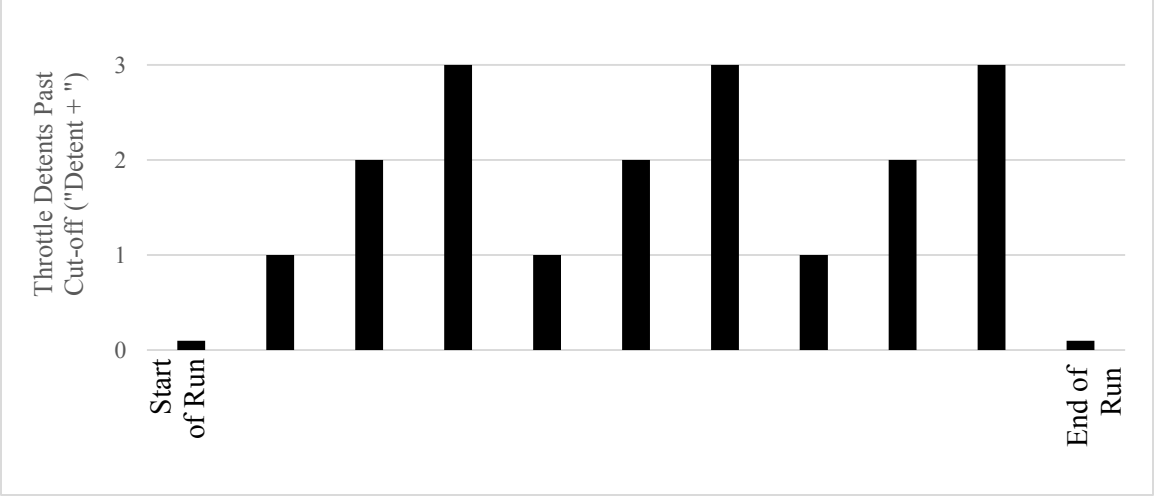

Figure 49 Step-style throttle schedule

6.5.2.2 Data Collection

At each throttle setting, over 300 voltage readings were collected from the thrust and torque transducers (described in 5.2.7) for later analysis.

An air data computer integrated into the wind tunnel measured the air speed. No calibration or verification of its readings was completed and it was only recorded at the beginning of a run.

The rotational speed of the propeller was measured using a timing strobe light. A strobe light can be used to find the speed by setting the flash rate so that the propeller appears to be static. As the propeller would appear static whenever the flash rate was a multiple of the rotational speed it was necessary to apply paint to the tips of the propeller blades so a single blade could be identified. To aid in setting the strobe flash rate an IR bounce tachometer was assembled and installed inside the nose cone. This tachometer was built and coded based on the plans detailed in [111] but provided an accurate speed (that is, one close the speed determined by the strobe light) once for every 6-8 readings, which did not allow it to be used instead of the strobe. It was useful in determining the rotational speed of the propeller when it was wind milling as that speed was difficult to determine quickly due to the lack of a throttle setting.

The motor on the test stand was controlled by a Phoenix Ice 100 ESC that has built in data logging features. The ESC was configured to record, at a rate of one sample per second [112];

- battery voltage;
- battery current;
- battery power input;
- motor speed;
- % motor power out;

- throttle setting; and
- power consumption rate

While the ESC's data-logger should have been a useful feature, it was found that the readings obtained from it were either:

- Erroneous, such as the RPM, which was logged as being 500 to 1000 RPM less than measured with the strobe light
- Questionable, such as the amount of power being drawn from the battery as being so low that it would mean that the propeller was over 98% efficient, or
- Vague, such as the how the percentage of power out of the controller was calculated and how it was possible that, when no current was being drawn from the battery, the output power was ~10-15%

The manufacturer of the ESC, Castle Creations, states that the ESC was never intended as a precision data-logging device but for comparison purposes [113], so the error associated with its readings is likely meant to be "good enough" for hobby users.

Overall, data collection was hampered by the poor quality of the instrumentation and transducers. The final torque transducer was not sensitive enough to measure the small amounts of torque generated by the propeller and the minute changes in voltages were masked by the significant voltage drift and noise of the analog to digital converters. Less than a third of all data collected was usable and no usable torque measurements were obtained from the current test stand.

6.6 Data Reduction

As a load was applied to either of the transducers the deformation of the strain gauges would result a drop in voltage, which was read by the ADC. Due to the drift of the ADC's it was impossible to correlate a specific voltage to a force or torque, instead the difference between the signal voltage and the null voltage (the signal voltage under no load) was used. During testing, no-load periods were included to provide a null voltage that could be used as a reference. However due to the non-linearity of the drift and signal noise determining the difference between the reference and the signal voltage was not a simple task. MATLAB was used to interpolate the reference voltage between two recorded voltages and then subtract the signal voltage from it. Typically linear regression was used, but if the reference signal start and end points indicated some curvature quadratic regression was used instead.

The quality of the signal was evaluated by calculating the voltage resolution based on the input signal. The smallest voltage that can be read by converter, ε_v, is equal to [102, p. 386]:

$$\varepsilon_V = \frac{\Delta V_{fs}}{2^n} \qquad \textbf{Eq. 74}$$

Where:

ΔV_{fs} = full scale voltage range of the converter

n = number of bits

Assuming that the input given to the transducer is held constant, the effective number of bits of the signal was calculated as:

$$n = log_2\left[\frac{\Delta V_{fs}}{\varepsilon_{Vmeasured}}\right] = log_2\left[\frac{\Delta V_{fs}}{V_{Smax} - V_{Smin}}\right] \quad \textbf{Eq. 75}$$

Where V_{Smax} and V_{Smin} are the maximum and minimum voltages in the sample. Typically the resolution was between 14.5 – 15.5 bits corresponding to ε_v of between 2.157 x 10^{-4} V and 1.078 x 10^{-4} V.

6.7 Results

6.7.1 As-Manufactured Propeller Performance

The thrust generated by the as-printed prop is shown in Figure 50 thru Figure 53. The propeller thrust observed during testing was close to the predicted thrust using both the single-point and full blade performance methods**.** As airspeeds increased the propeller's performance became less than predicted, indicating the blade pitch may be decreasing under the increased air loading due to vibrations or quasi-static deformation.

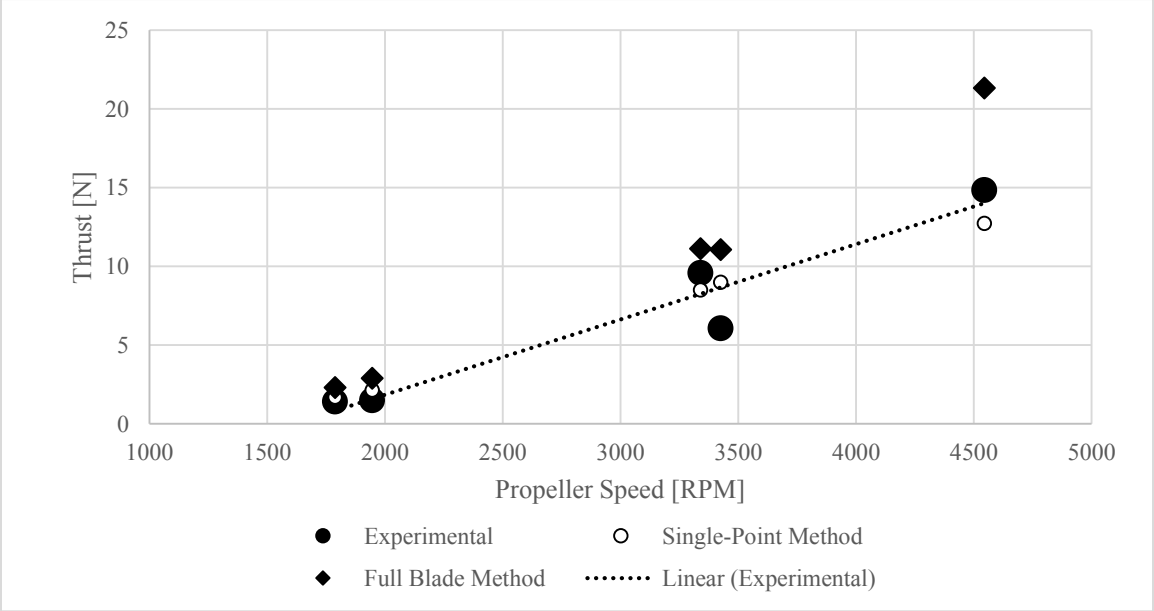

Figure 50 As-manufactured propeller performance at 14.2 km/h (7.6 kt)

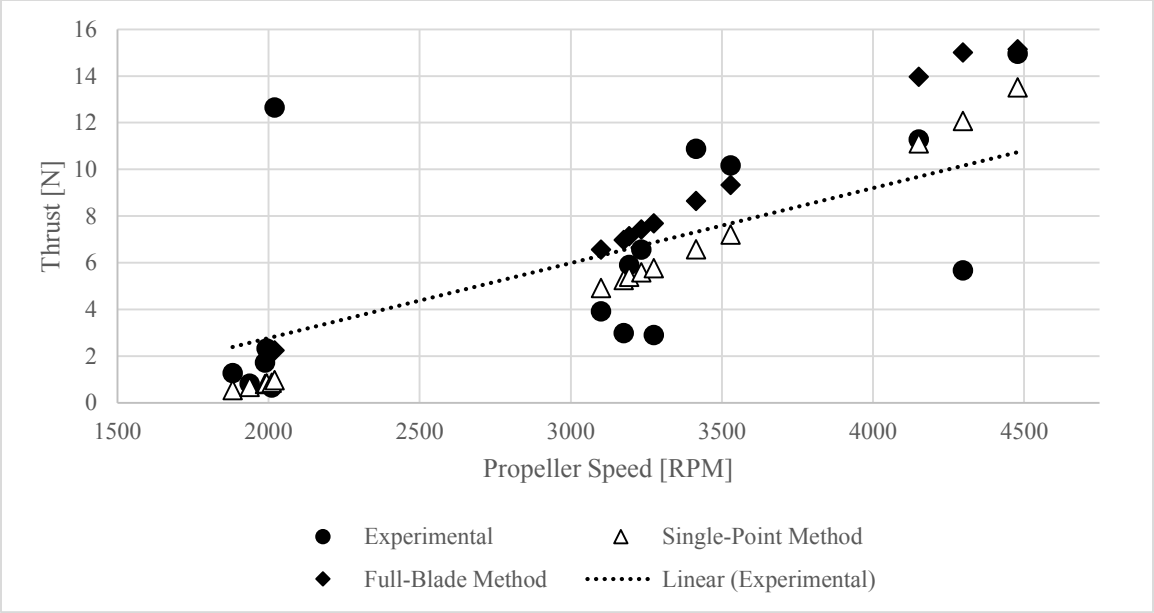

Figure 51 As-manufactured propeller performance at 25 km/h (13.5 kt)

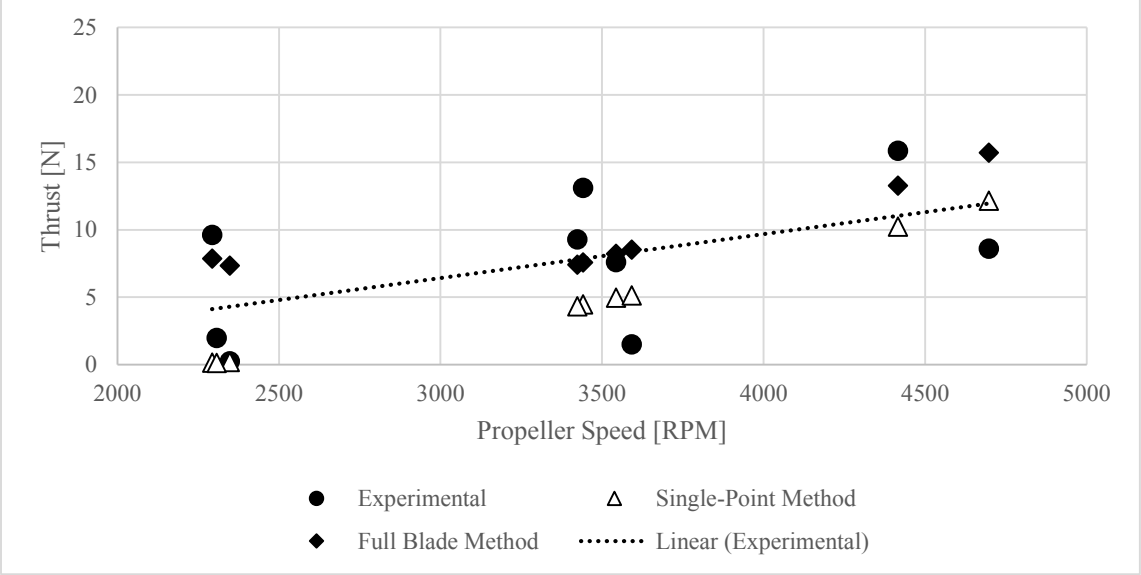

Figure 52 As-manufactured propeller performance at 35 km/h (19 kt)

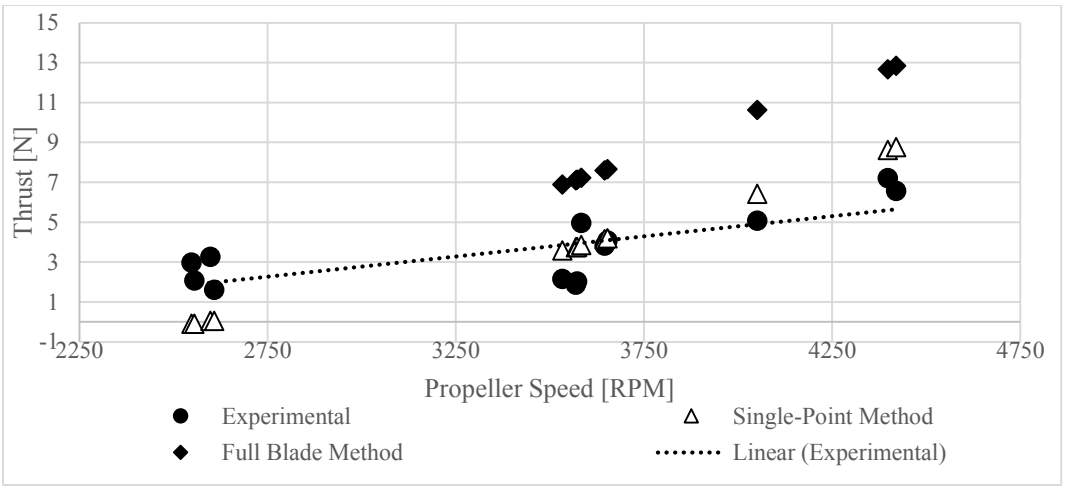

Figure 53 As-manufactured propeller performance at 40 km/h (22 kt)

The power consumption was recorded for one test with the ESC and is presented in Table 20. The ESC data did not help to assess the efficiency of the propeller and motor combination as it appeared to suffer from inaccuracies in the recorded values. For example, some combinations the ESC suggested that considerably more power is being absorbed by the propeller (assuming the thrust measurement is accurate) than was provided by the battery.

Speed [km/h]	**Throttle Detent**	**ESC Power Draw** [W]	**Single-Point Estimate** [W]	**Full-Blade Perf. Method** [W]	**Thrust** [N]	**Power Absorbed** (Thrust × Velocity) [W]
	D+2	65	103	133	10	38
	D+3	191	190	327	15	59
14.2	D+2	65	111	135	6	24
	D+2	63	101	133	10	71
	D+3	166	223	260	15	104
25	D+2	62	91	120	11	76
	D+2	40	75	118	13	127
	D+3	141	183	242	16	154
35	D+2	39	73	115	9	90

Table 20 ESC battery power draw compared to estimated motor power

6.7.2 Epoxy-Coated Propeller

The epoxy-coated propeller was run at three tunnel speeds – 14.2 km/h, 25 km/h, and 35 km/h – and the thrust measured is compared to the estimated thrust in Figure 54 - Figure 56. The epoxy-coated blades were slightly stiffer, but were tested with the step profile and, as a result, there was less scatter in the data showing a much stronger correlation with the predicted performance. The epoxy-coated propeller when compared to the as manufactured appears to produce marginally more thrust; however, it would be difficult to make this conclusion based on the existing test rig. One interesting trait was that, while the as-manufactured blade also wind milled, this blade seemed more susceptible to it. This may have been due to a manufacturing defect influencing the blade angles, or, as only one test was completed, an anomaly with the instrumentation

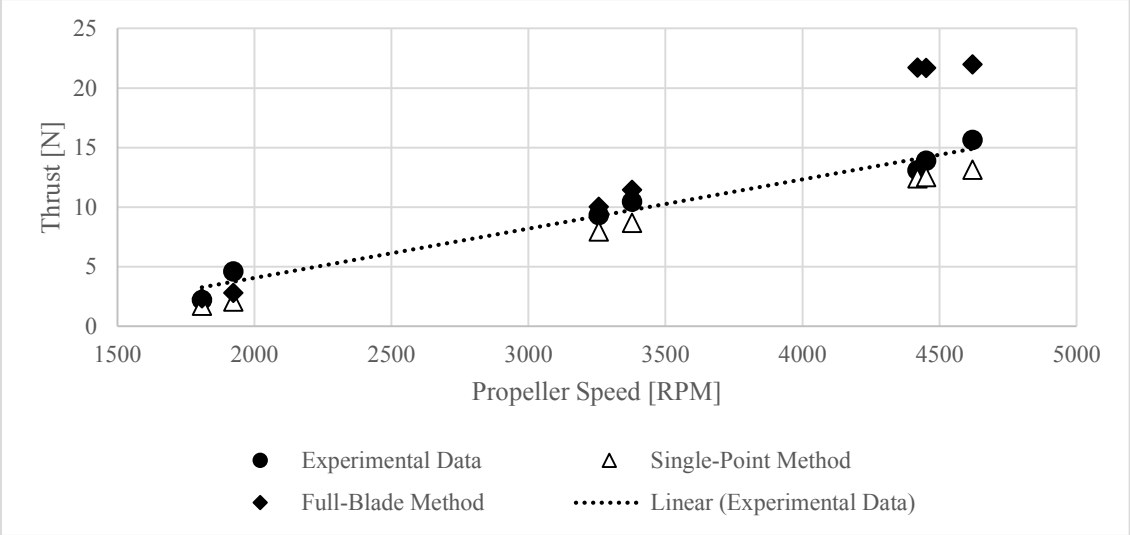

Figure 54 Epoxy-coated propeller at 14.2 km/h

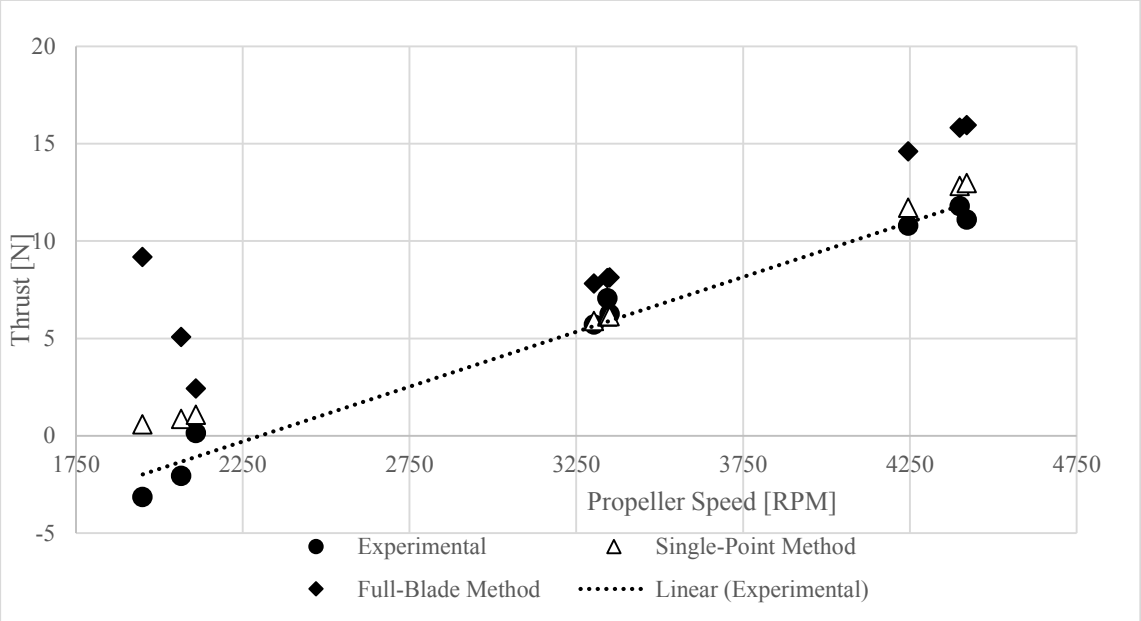

Figure 55 Epoxy-coated propeller at 25 km/h

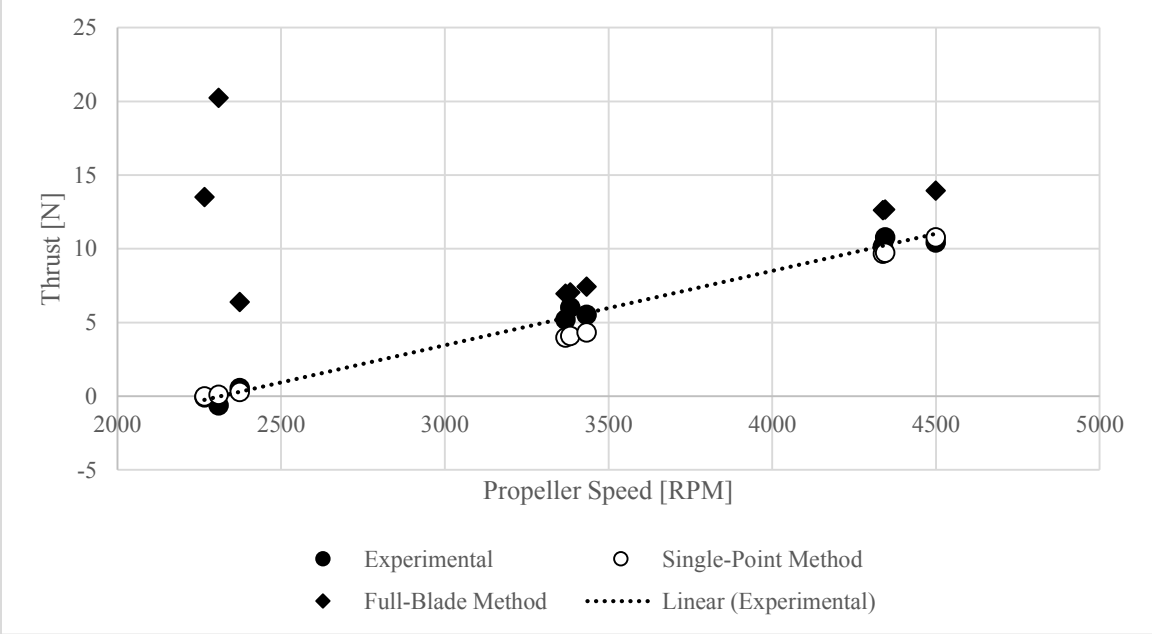

Figure 56 Epoxy-coated propeller at 35km/h

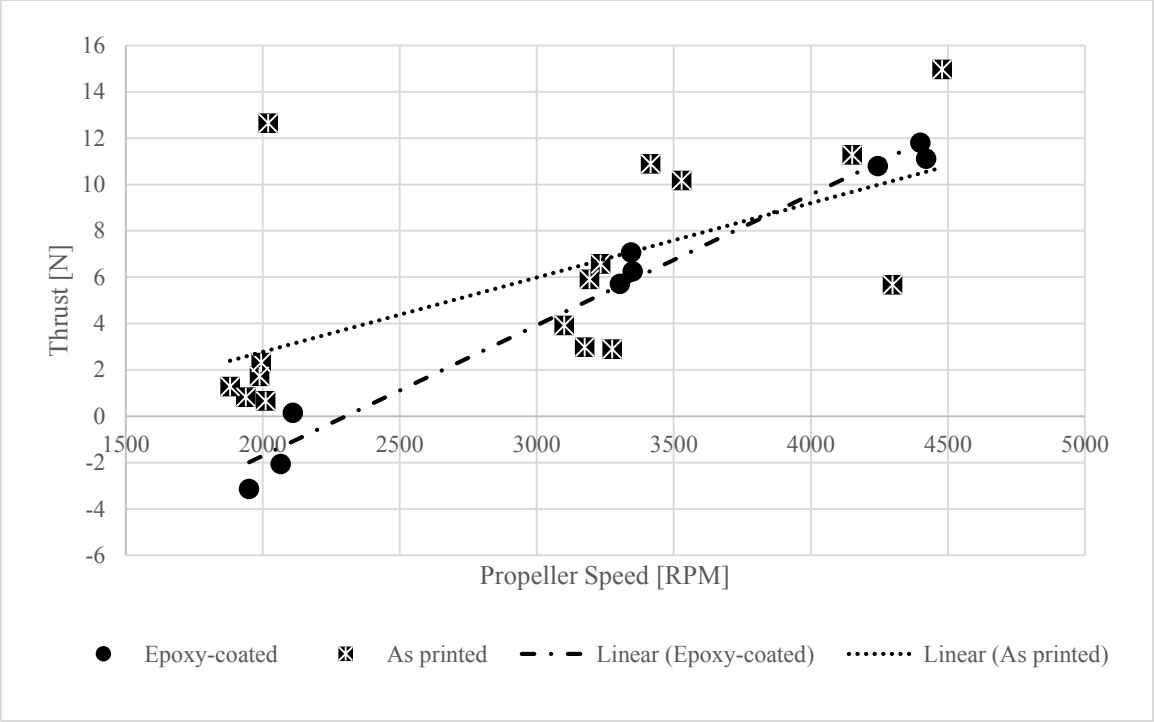

Figure 57 Comparison between as-manufactured and epoxy-coated propeller when operating at 25 km/h

6.7.3 Meeting Mission Requirements

Based on the mission requirements detailed in section 6.3 the propellers that were manufactured produced less thrust than expected, with thrust decreasing as the rotational and forward speeds increased. There are two possible reasons for this:

1. The centrifugal twisting moment acting on a blade will attempt to twist it towards a flat pitch. Given the flexibility of the blades, it would not take a significant amount of torque to reduce the blade pitch. As the forward speed increased the angle of attack of the blade decreased, reducing lift and thrust.
2. The thrust predicted by the full-blade performance method is incorrect. This is very possible as the measured thrust shows a strong correlation to the single point

performance method predicted thrust and the full-blade estimates at some point are obviously wrong (such as predicting 20N of thrust at speeds just beyond the propeller wind milling)

It is worth nothing that, while the requirements for the propeller were incorrectly defined and corresponded closer to the needs of a 17kg aircraft, the propeller did produce sufficient thrust for a 5kg aircraft to fly the intended mission.

Better thrust measurement and perhaps the use of a third party code (such as QPROP) would help to establish if the predictions are correct, and testing a much stiffer blade (such as one made from Duraform HST) would allow for the stiffness to be investigated.

	Speed		**Design Thrust**	**Rotational Speed**	**Delivered Thrust @ Rot. Speed**	**Max Delivered in Testing**
	[KTAS]	*[km/h]*	*[N]*	[RPM]	[N]	[N]
Maximum Endurance	19	*35*	14.45	4200	10.00	12
Maximum Range	23	*42*	12.73	4000	7.00	8

Table 21 Thrust required and measured during testing

7 Chapter: Conclusions and Recommendations

7.1 Conclusions

The objective of this thesis was to develop a process for the design and manufacture of mission- and aircraft- specific propellers for small unmanned aerial vehicles. This objective was accomplished in part as propellers were produced and tested in simulated flight conditions without failure. However the series of design, manufacturing and instrumentation issues prevented a thorough and accurate evaluation of their performance. Although a thorough examination of the propeller performance was not possible, specific conclusions from the propeller design process, material testing, wind tunnel tests and overall feasibility of this approach can be made. To the knowledge of the author, this research represents the first full implementation of an integrated process for the design, manufacture and qualification of mission specific propellers for small UAVs.

7.1.1 Thoughts on the Design of the Propeller

A program was written to create the propeller by combining proven propeller design methods and a detailed analysis of the performance of the aircraft and motor. This code took into account many aspects neglected by other design programs and is comparable to the in-house software used by manufacturers of RC [40], UAV [114], and manned-aircraft [11] propellers. However, with increasing complexity comes a greater likelihood of errors being made both of which undermine the capabilities of the program. This was definitely the case as both errors in judgment and implementation occurred.

The program had a few shortcomings. The lack of a cross-check between the temperamental results of the full blade performance method and the single point estimate method allowed incorrect results to drive the selection of the blade design used for the propeller. The structural analysis of the propeller was not well incorporated into the blade design process. By performing the structural analysis after the blade had been designed, there was no way of correcting the any deficiencies. This essentially left the strength of the blade dependent on a crude estimate of the stresses within the blade.

While there are clear problems with the current version of the design program, all of the aforementioned in-house software used by propeller manufacturers was described as being developed over the course of several years of refinement and testing. In the case of the design program used by Hamilton Standard [11], this includes the methods developed over decades of propeller design and manufacturing. While it would be a major achievement from the present research, a flawless program that produces perfect propellers on the first round of testing is unrealistic. Further development by future students is needed. None of the problems noted requires a major revision of the methodology but rather further refinement of the code itself to become fully competitive with any existing comprehensive propeller design program.

7.1.2 Thoughts on Materials and Manufacturing

If the research completed proved anything, it is that durable and functional 3D printed propellers can be manufactured for small UAVs using currently available materials and manufacturing methods. While the propellers produced for testing did not reflect the quality that had been achieved during manufacturing trials, they did demonstrate the durability of the material. Even with obvious defects, the test propellers

underwent over 10 hours of simulated flight-testing without any visually-detectable signs of imminent failure. The laboratory material coupon testing completed showed that even a low-end 3DP plastic was able to withstand the maximum stresses that would be seen in a propeller blade for over three times the expected lifespan of the aircraft.

It was noted that, during testing, the blades did have a considerable amount of vibration that reduced the net thrust produced. A thin coat of epoxy improved performance and stiffness, but it is likely that the use of stiffer plastics and an improved structural design approach is required.

7.1.3 Thoughts on Wind Tunnel Testing

The primary reason that the test results are inconclusive is because accurately measuring the thrust and torque of the propeller was incredibly challenging. This was due a combination of problems with the transducers and the instrumentation.

7.1.3.1 Thrust and Torque Transducers

The thrust transducer was able to measure thrust but the measurement head had difficulty returning to its original position. This was due to the sliding/rolling nature of the bolt (on the back of the measurement head) sliding along the bending beam. It was found that when both parts were lubricated the head returned to its original position much easier. After lubrication, and with a modification in the test pattern, it was found that useable thrust data was obtainable.

The torsion cell did not work for several reasons. The cell had been designed for the torque produced by a much larger motor so it was inappropriate for the much smaller

motor that was used during testing. Other constraints, such as the rear shaft extending from the motor, the need for it to interface with other components, manufacturing limitations, and hand and tool clearances added complications and made it difficult to design a torque transducer in such a way it could measure the motor's thrust. Installing a strain gage onto a round surface is not a simple task and it is possible that the gages were installed improperly and could not sense the slight deformation under the light torque applied to the cell.

7.1.3.2 Instrumentation

The analog-to-digital converters were found to be incapable of providing repeatable, low-drift and readings due to one of several factors. A 100 uF filtering capacitor was installed to cut down on signal noise, and this may have contributed to the drift problem by essentially turning the entire ADC into a large RC charging/discharging circuit. The long time period between the rise and fall of a constant voltage would suggest that this were the case. The filtering capacitors were a deviation from the plans due to exceptionally high signal noise. The circuit was assembled on a prototype board, which is suited to proving the functionality of electrical circuits and not assembling precise ADC. If the circuit was built on a breadboard, as was planned, it would likely have reduced noise to the extent that the filtering capacitors could possibly have been removed. While the drift can be removed, the time needed to remove it is not trivial, which makes quick data analysis very difficult

7.1.3.3 Overall Approach to Testing

The test stand had some major shortcomings but is no different than any other aspect of this work as it can be improved. It is likely far easier to fix than the code or material selection as improvements to the test stand require nothing more than purchasing and integrating off-the-shelf equipment. Other than the time needed to become familiar with the equipment this is a simple mechanical design problem. Two features of the test rig – large volumes of internal space and large, easy-to-open access panels - proved invaluable during testing when adjustments needed to be made or equipment relocated. The test stand was also designed specifically with a body-on-frame design to allow the nose cone, nacelle, and pylon to be easily removed and replaced, allowing other external geometries to be installed. Once the instrumentation is upgraded, the test stand should be able to serve as an invaluable tool for any future propeller research.

7.1.4 Overall Feasibility

While the results of testing were disappointing, the feasibility of the process to produce propellers for a small UAV was firmly established. Manufacturing flight-worthy propellers, however, would take refinement of the design program, possibly a change of material, and require additional ground and wind tunnel testing.

7.2 Future Work

7.2.1 Correcting Issues Identified During Testing

7.2.1.1 Improved Structural Analysis Methods and Integration

As has been mentioned the structural analysis methods could be better integrated into the blade design process. The detailed methods described in Borst [30] which were developed for flexible propeller blades for V/STOL aircraft which would be well-suited to the similiarly flexible 3DP propellers.

7.2.1.2 Improved Transducers and Instrumentation

Ultimately, commercially available thrust and torque transducers and data acquisition systems should be installed into the test stand. The design and manufacture of a transducer capable of accurately measuring small amounts of thrust and torque is not a trivial task and making one is more than likely a trial-and-error process than anything else. The existing head design could be retained however as similar designs have been successfully used in the past.

Data was collected from the ADC by recording the serial data captured from the Arduino and recording it to a text file, or initially, copy-and-pasting it into Microsoft Excel. While simple, neither method allowed for readings to be easily observed in real-time during the testing as a scrolling list of raw voltages, with noise and drift, is hard to interpret. Had the ability for real-time monitoring existed some tests could have been aborted if it was observed that no useable data was being collected. A commercially-available ADC may also offer less noise than the ones that were built and make it easier

to experiment with different gain settings for amplifying the raw singles from the strain gauges. This would allow for a stronger and clearer thrust measurements to be made.

7.2.2 Improvements to the Process

7.2.2.1 Interfacing XFOIL with the Design Program

The design program used tabulated data from XFOIL for design purposes. Collecting data from XFOIL is not a particularly difficult task but it is very time consuming creating tables to provide that information to the program in the correct format. The code should be modified to create the lookup tables with data from either XFOIL.

The trailing-edge correction changes the rear portion of the airfoil, which has some effect on its aerodynamic characteristics. To account for these changes either program could be used to obtain the new aerodynamic characteristics of the modified airfoil. This was attempted using another code but the results obtained from this program were questionable and could not be trusted.

7.2.2.2 Modelling the Airflow Around the Airframe

The program designed the propeller to operating with either a constant forward velocity or the velocity profile that would be expected if the propeller were operating with a NACA D-style spinner. It is likely that the actual free stream airflow was neither condition. To better integrate the propeller with the aircraft, the airflow around the front of the fuselage of the application UAV should be modelled (likely using CFD) and be

used to improve the design of the propeller. As this is a time consuming process, standard profiles could be created for typical UAVs.

7.2.2.3 Externally-Reinforced Blade Structure

Fiber-reinforced SLS plastics offer good strength and stiffness but are considerably more expensive than low-cost FDM plastics such as P400. One possible method for obtaining a stiffer blade while maintaining a low overall cost would be to print a P400 blade core and bond strips of CFRP to the upper and lower surface to act as spar caps. The blade would then be covered, if necessary, with some sort of coating or covering for a smooth aerodynamic surface and to reduce the possibility of the bond between the core and spar caps being compromised. This style of construction was based on that used by Dowty for their modern propeller blades (such as those used on the Bombardier Q400 and Lockheed Martin C-130J) [39]. This construction unfortunately could not be tested as planned.

7.2.2.4 Designing Flexible Propellers or Ground-Adjustable Propellers

An alternative to constructing rigid propellers would be to take advantage of the deflection of the blade and use it to make it a passively-variable pitch propeller that would be deform to the desired blade angle for a specific operating condition. Some work on this subject has been performed [115] but was published too late in the design process to be incorporated into the program. Designing the propeller with the intention of it flexing to achieve a given blade angle in flight is by no means simple but would eliminate some of the limitations of a fixed-pitch propeller.

One means of producing a larger propeller without using a larger printer would be to manufacture each blade and the hub separately and then assemble the propeller. As the blades are independent of the hub, it may be possible to design the hub so it is ground adjustable. This would allow the blade pitch to be changed before flight, allowing for the propeller's performance to be tuned to whatever is needed for the mission. A proof of concept model of the ground-adjustable hub used by Sensenich for propellers for LSA was made for evaluation. This type of hub was not used due to the additional complexity of the ground-adjustable propeller increasing the risk of propeller failure during testing. Ground adjustable propeller design should be investigated to permit 3DP propellers to be produced for larger UAVs.

7.2.2.5 Complete Modelling of a UAV's Propulsion System

Considering the overall efficiency of the propulsion system is more relevant than looking only at the performance of the propeller as it includes the power losses incurred by the motor. As was the case during testing, the motor may not be operating anywhere near its optimum and its inefficiency may counteract any benefit from using an optimal propeller. The aircraft's battery should also be included the analysis as it likely has an optimal power output. By operating the propeller, motor and batteries at/near the conditions they perform optimally at the overall efficiency of the propulsion system can be maximized, enabling longer aircraft loiter duration and range.

7.2.2.6 Improved Instrumentation

It is doubtful that making an ADC saved any money or time over purchasing or borrowing an off-the-shelf strain gauge module, ADC and building a Labview script to

read, display and store the test data. For future testing, employing COTS instrumentation hardware is strongly recommended.

7.3 Implications of Work

7.3.1 Use for Manned-Aircraft Propeller Design

Ignoring the work completed on 3DP, the design code could be modified and expanded to produce propellers for manned aircraft. This new use would require additional work, such as to fully capture the effects of compressible flow on the propeller blades and a code for determining the optimum performance of a internal-combustion or turboprop engine.

7.3.2 3D Printed Mission-Specific UAVs

Recent advances in the size of large 3D printers make it possible to 3DP an entire flying-wing UAVs. A majority of the code composed and material testing provided the basis of what would be needed to write a program to design small, mission-specific 3DP UAVs. A flying-wing style of aircraft could be designed with the same framework used to produce the propellers. After entering the aircraft's payload and mission parameters, the program would size the aircraft to achieve the mission's main objectives. The airframe would then be designed using a similar iterative approach where each wing station is sized considering performance, stability and control, structural, and payload requirements. Using the propeller design code and a databank of available motors and batteries, the propulsion system would be designed. The curves of the fuselage would then be exported.

Alternatively, if a large printer is unavailable or if a configuration other than a flying wing design is desired the program scale and optimize a generic airframe that would then be assembled after printing. While the production of larger sections may be impossible or uneconomical to print (such as wing and fuselage skins), the program could be used to create files to be waterjet or laser cut and attached to the 3DP frames, much like was done for the test stand nose cone.

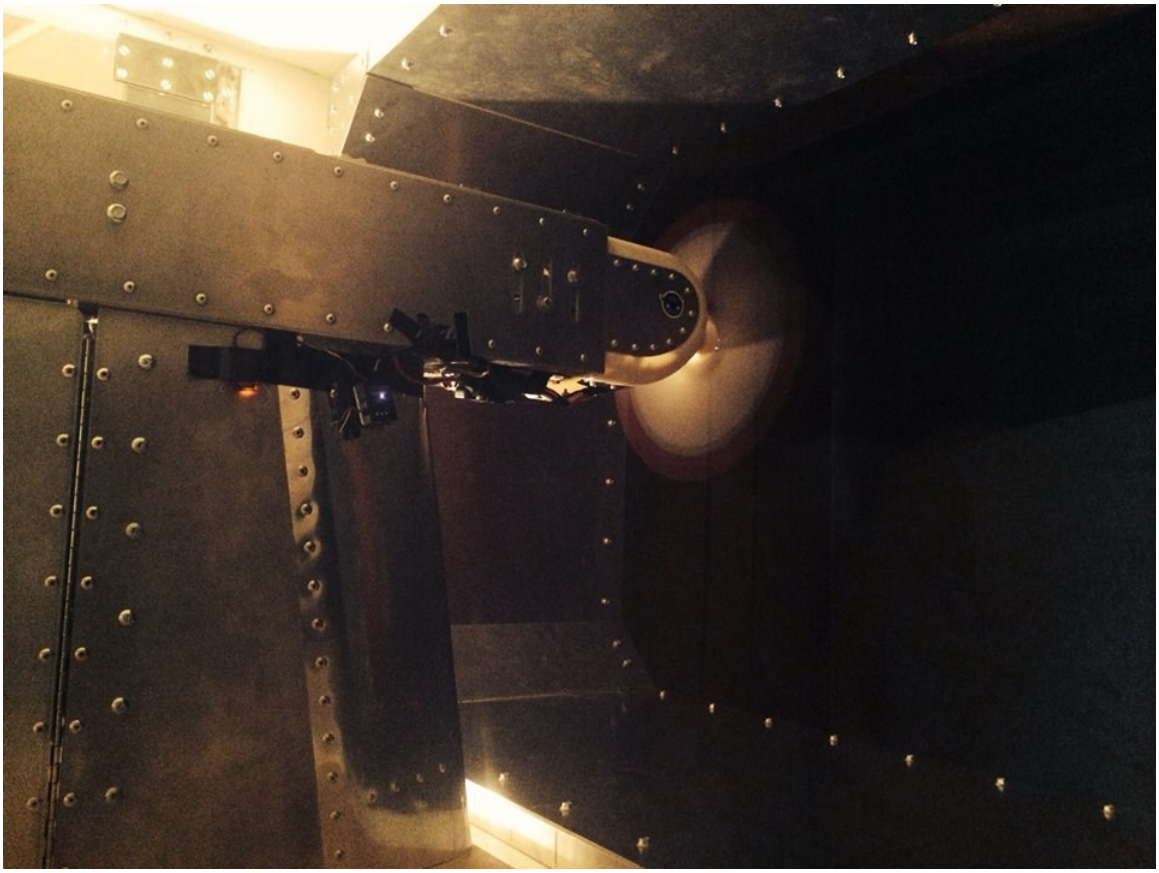

Figure 58 Epoxy-coated propeller running at 4700 RPM

Bibliography

[1] CARAC Unmanned Air Vehicle System Program Design Working Group, "Small Unmanned Air Vehicle (UAV) Definitions and Best Practices," Unmanned Systems Canada, 2013.

[2] Barnard Microsystems, "UAV Design Guidelines," 18 August 2014. [Online]. Available: http://www.barnardmicrosystems.com/UAV/uav_design/guidelines.html.

[3] D. J. M. Roughley, "Canadian Market Opportunities for UAS: Non-Military Applicatiosn," Strategic Technology Consulting, North Vancouver, BC, 2008.

[4] Sanders Geophysics, "SGL Aircraft," 8 August 2014. [Online]. Available: http://www.sgl.com/Aircraft.html.

[5] Airbus Helicopter, "Fugro Airborne Surveys Canada Selects the AS350 B3e as First Rotary Wing Purchase," 9 February 2012. [Online]. Available: http://www.airbushelicopters.ca/fugro-airborne-surveys-canada-selects-the-as350-b3e-as-first-rotary-wing-purchase/.

[6] Brican Flight Systems, "UAV Configuration," 18 August 2014. [Online]. Available: http://bricanflightsystems.com/services/uav-configuration/.

[7] Diamond Aircraft, "DA42 Specs & Options," 18 August 2014. [Online]. Available: http://www.diamondaircraft.com/aircraft/da42/specs.php.

[8] T. L. V. Michael J. Logan, "Technology Challenges in Small UAV Development," NASA, 2007.

[9] J. B. Brandt and M. S. Selig, "Propeller Performance Data at Low Reynolds Numbers," in *49th AIAA Aerospace Sciences Meeting*, Orlando, FL, 2011.

[10] APC Propellers, "APC Propeller Performance Data," [Online]. Available: http://www.apcprop.com/v/downloads/PERFILES_WEB/datalist.asp. [Accessed 19 August 2014].

[11] NASA, "NASA CR-168045 Small Transport Aircraft Technology," NASA Scientific and Technical Information Facility , 1983.

[12] Daher-Socata, "Unrivaled Performance," 19 August 2014. [Online]. Available: http://www.tbm.aero/index.php/tbm-900/tbm-aircraft/overview/performance.

[13] J. M. McClellian, "TBM 900: The science of airflow managemetn," *SportAviation,* pp. 74-78, June 2014.

[14] Daher-Socata, "Model Comparisons," 19 August 2014. [Online]. Available: http://www.tbm850.com/2014/index.php/tbm-900/tbm-aircraft/tools/comparisons.

[15] B. W. McCormick, Aerodynamics, Aeronautics, and Flight Mechanics, Second Edition ed., Daryaganj, New Delhi: Wiley India (P.) Ltd, 1995.

[16] F. E. Weick, Aircraft Propeller Design, New York: McGraw-Hill Book Company, Inc, 1930.

[17] H. V. Borst, Summary of Propeller Design Procedures and Data Volume I - Aerodynamic Design and Installation, Fort Eustis, Virginia: U.S. Army Air Mobility Research and Development Laboratory, 1973.

[18] ANC-9, Aircraft Propeller Handbook, Washington, 1956.

[19] Federal Aviation Administration, Airman Testing Standards Branch, Pilot's Handbook of Aeronautical Knowledge, Oklahoma City: United States Department of Transportation, Federal Aviation Administration, Airman Testing Standards Branch, 2008.

[20] Curtiss-Wright Corporation, Propeller Theory, Cadwell, New Jersey, USA: Curtiss-Wright Corporation, Propeller Division, 1944.

[21] NWUAV, "Variable Pitch | Constant Speed Propeller Systems," NWUAV, 19 May 2014. [Online]. Available: http://www.nwuav.com/uav-products/variable-pitch-propellers.html. [Accessed 18 August 2014].

[22] F. E. Weick, "TN 212 - Simplified Propeller Design for Low-Powered Airplane," National Advisory Committee on Aeronautics, 1925.

[23] E. P. Hartman and D. Biermann, "TR-640 The aerodynamic characteristics of full-scale propellers having 2, 3, and 4 blades of Clark y and R.A.F. 6 airfoil sections," National Advisory Committee on Aeronatics, 1938.

[24] D. H. E. P. Biermann, "TR 642 - Tests of five full-scale propellers in the presence of a radial and a liquid-cooled engine nacelle, including tests of two spinners," National Advisory Committee on Aeronautics, 1938.

[25] enginehistory.org, "Hamilton Standard Hydromatic Propeller," [Online]. Available: http://www.enginehistory.org/Propellers/HamStd/hamstd.shtml. [Accessed 19 August 2014].

[26] "Spitfire Mk. I versus Me 109 E," WW2 Aircraft Performance.com, [Online]. Available: http://www.spitfireperformance.com/spit1vrs109e.html#propellers. [Accessed 19 August 2014].

[27] J. L. Crigler, "TR 924 - Application of Theodorsen's Theory to Propeller Design," National Advisory Committee on Aeronautics, Langley Field VA, 1949.

[28] C. N. Adkins and R. H. Liebeck, "Design of Optimum Propellers," *Journal of Propulsion and Power,* vol. 10, no. 4, pp. 676-682, 1994.

[29] E. Larrabee, "Practical Design of Minimum Induced Loss Propellers," in *Business Aircraft Meeting and Exposition*, Wichita, KS, 1979.

[30] H. V. Borst, W. Ammat and W. E. Bates, Summary of Propeller Design Procedures and Data Volume II - Structural Analysis and Blade Design, Springfield, VA: National Technical Information Service, U.S. Department of Commerce, 1973.

[31] A. J. Colozza, "APEX 3D PRopeller Test Preliminary Design," National Aeronautics and Space Administration, Brook Park, Ohio, 2002.

[32] O. Gur and A. Rosen, "Optimization of Propeller Based Propulsion System," *Journal of Aircraft,* vol. 46, no. 1, pp. 95-106, 2009.

[33] Borst, Henry V. & Associates, "USAAMRDL-TR-77-45A Aerodynamic Design and Analysis of Propellers for Mini-Remotely Piloted Air Vehicles, Volume 1 - Open Propellers," U.S. Army Aviation Research and Development Command, St. Louis, MO, January 1978.

[34] R. H. Lorenz, "An Experimental Investigation of Single- and Dual-Rotating Propellers," University of Toronto, Toronto, 1988.

[35] D. L. Wall, "Optimum Propeller Design for Electric UAVs," Auburn University, Auburn, Alabama, 2012.

[36] A. C. Piccirillo, "The Clark Y Airfoil - A historical retrospective," in *World Aviation Conference*, San Diego, CA, 2000.

[37] M. Hollman, Modern Propeller and Duct Design, Montery, California: Martin Hollmann, 2006.

[38] D. Velupillai, "Dowty's better propeller," *Flight,* pp. 367-369, unk. 1981.

[39] Dowty Propellers, "Bombardier Q400 Dash 8 Advanced Propeller System".

[40] APC Propellers, "APC Propellers Engineering Design," [Online]. Available: http://www.apcprop.com/v/Engineering/engineering_design.html. [Accessed 20 August 2014].

[41] E. N. Jacobs, K. E. Ward and R. M. Pinkerton, "TR 460 - The Characteristics of 78 Related Airfoil Sections from Tests in the Variable-Density Wind Tunnel," 1933.

[42] J. T. Lowry, "Performance of Light Aircraft," AIAA Education Series, Reston, VA, 1999.

[43] W. F. Lindsey, D. B. Stevenson and B. N. Daley, "TN 1546 - Aerodynamics characteristics of 24 NACA 16-series airfoils at Mach numbers between 0.3 and 0.8," National Advisory Committee on Aeronautics, Langley Field, VA, 1948.

[44] I. H. Abbot, A. E. Von Doenhoff and L. J. Stivers, "TR 824 - Summary of Airfoil Data," National Advisory Committee on Aeronautics, Langley Field, VA, 1945.

[45] H. V. Borst, "Summary of Propeller Design Procedures and Data, Volume 3 - Hub, Actuator and Control Design," Army Air Mobility Research and Development Laboratory, Fort Eustis, VA, 1973.

[46] E. N. Jacobs and A. Sherman, "TR 586 - Airfoil Section Characteristics as Affected by Variations of the Reynolds Number," National Advisory Committee on Aeronautics, Langley Field, VA, 1937.

[47] Magazine, MIT AeroAstro, "Faculty profile: Mark Drela's research — and his teaching — offer beauty and functionality," 2006. [Online]. Available: http://web.mit.edu/aeroastro/news/magazine/aeroastro-no3/2006drela.html. [Accessed 20 August 2014].

[48] M. Drela, "XFOIL Subsonic Airfoil Development System," MIT, [Online]. Available: http://web.mit.edu/drela/Public/web/xfoil/. [Accessed 20 August 2014].

[49] X. Mauclere, "Automatic 2D Airfoil Generation, Evaluation and Optimisation Using MATLAB and XFOIL," Technical University of Denmark, Lyngby, 2009.

[50] W. Chen and L. P. Bernal, "Design and Performance of Low Reynolds Number Airfoils for Solar-Powered Flight," in *AIAA Aerospace Sciences Meeting and Exhibit*, Reno, Nevada, 2008.

[51] Transport Canada, "Part V Airworthiness Manual Chapter 535 - Aircraft Propellers 2012-1 Ammdt," 2012. [Online]. Available: http://tc.gc.ca/eng/civilaviation/regserv/cars/part5-standards-chapter535-1929.htm. [Accessed 20 August 2014].

[52] Federal Aviation Administration, "PART 35—AIRWORTHINESS STANDARDS: PROPELLERS," 20 August 2014. [Online]. Available: http://www.ecfr.gov/cgi-bin/text-idx?c=ecfr&rgn=div5&view=text&node=14:1.0.1.3.18&idno=14. [Accessed 20 August 2014].

[53] Office of the Secretary of Defense, "UAV Reliability Study," Office of the Secretary of Defense, Washington, 2003.

[54] US Department of Transportation, Federal Aviation Administration, "AC No. 35.37-1B Propeller Fatigue Limits and Evaluation," US DOT FAA, 2011.

[55] T. J. Gornet and T. L. Starr, "Mechanical and Fatigue Properties of Polymers for Direct Digital Manufacturing," University of Louisville, Louisville, KY.

[56] ASTM, "F2506-13 Standard Specification for Design and Testing of a Light Sport Aircraft," ASTM, West Conshohocken PA, 2013.

[57] ASTM, "Standard Specification for Design and Performance of a Light Sport Airplane," ASTM, West Conshohocken, PA, 2013.

[58] RC Airplane Propellers, [Online]. Available: http://www.rc-airplanes-simplified.com/rc-airplane-propellers.html. [Accessed 28 April 2013].

[59] XOAR, "About XOAR," [Online]. Available: http://www.xoarintl.com/about-xoar/. [Accessed 20 August 2014].

[60] F. W. Caldwell and N. S. Clay, "TN 198 - TN 201 Micarta Propellers Vol 1 - 4," National Advisory Committee on Aeronautics, Langley Field, VA, 1924.

[61] J. M. McClellan, "High Tech Props," *Sport Aviation,* pp. 68-72, April 2014.

[62] A. Baker, S. Dutton and D. Kelly, Composite Materials for Aircraft Structures, Reston, VA: AIAA, 2004.

[63] APC Propellers, "APC Propeller Manufacturing Process used by Landing Products," 2008. [Online]. Available: http://www.apcprop.com/v/Research/research.html#materials. [Accessed 24 August 2014].

[64] K. G. Budinski and M. K. Budinski, Engineering Materials Properties and Selection, Upper Saddle River, NJ: Prentice Hall, 2010.

[65] NASA Tech Briefs, "Relatively Inexpensive Rapid Prototyping of Small Parts," NASA, 22 January 2007. [Online]. Available:

http://www.techbriefs.com/component/content/article/7-ntb/tech-briefs/manufacturing-and-prototyping/983. [Accessed 24 August 2014].

[66] S. Kalpakjian and S. R. Schmid, Manufacturing Engineering and Technolgy, 5th ed., Upper Saddle River, NJ: Pearson - Prentice Hall, 2006.

[67] J. Excell and S. Nathan, "The rise of additive manufacturing," 24 May 2010. [Online]. Available: http://www.theengineer.co.uk/in-depth/the-big-story/the-rise-of-additive-manufacturing/1002560.article. [Accessed 20 August 2014].

[68] C. McEndree, "Review, Selection and Installation of a Rapid Prototype Machine," NASA Center for Aerospace Information, Houston, 2008.

[69] M. Prigg, "The secret behind James Bond's Aston Martin DB5: How Skyfall producers used 3D Printed cars to spare the priceless original," Daily Mail, 13 November 2012. [Online]. Available: http://www.dailymail.co.uk/sciencetech/article-2232252/The-secret-James-Bonds-priceless-Aston-Martin-DB-5-stunts-3D-printed-models-used-Skyfalls-dangerous-scenes.html. [Accessed 20 August 2014].

[70] NASA, "NASA Tests Limits of 3-D Printing with Powerful Rocket Engine Check," 27 August 2013. [Online]. Available: http://www.nasa.gov/exploration/systems/sls/3d-printed-rocket-injector.html#.U_V2OPlT6P8. [Accessed 20 August 2014].

[71] Stratasys, "Additive Manufacturing Trends in Aerospace:," 2013. [Online]. Available: http://web.stratasys.com/rs/objet/images/SSYS-WP-AeroTrends-03-13-FINAL.pdf. [Accessed 20 August 2014].

[72] W. Zhu, X. Zhao, W. Zhang, K. Ren, Z. Zhang and D. Li, "Design and Evaluation of Fully Configured Models Built by Additive Manufacturing," *AIAA Journal Early Edition,* pp. 1-11, 2014.

[73] Advanced Manufacturing Resource Centre, University of Sheffield, "FDM-printed fixed wing UAV," 14 March 2014. [Online]. Available: http://www.amrc.co.uk/featuredstudy/printed-uav/. [Accessed 21 August 2014].

[74] Solid Concepts, "UAV Component Manufacturing," [Online]. Available: http://www.solidconcepts.com/industries/uav-component-manufacturing/. [Accessed 21 August 2014].

[75] Stratasys, "Dimension 1200es Specifications," [Online]. Available: http://www.stratasys.com/3d-printers/design-series/dimension-1200es. [Accessed 21 August 2014].

[76] RepRap, "RepRap," [Online]. Available: http://reprap.org/wiki/Main_Page. [Accessed 21 August 2014].

[77] I. A. Technologies, "ABS and PLA Materials in a 3D Fused Deposition Modeling World," 30 November 2013. [Online]. Available: http://inside.at.utep.edu/?p=1523. [Accessed 20 August 2014].

[78] Wikipedia, "Direct Metal Laser Sintering," [Online]. Available: http://en.wikipedia.org/wiki/Direct_metal_laser_sintering. [Accessed 21 August 2014].

[79] S. Brewster, "Why you won't see a laser sintering 3D printer on your desk anytime soon," 25 April 2014. [Online]. Available: http://gigaom.com/2014/04/25/why-you-wont-see-a-laser-sintering-3d-printer-on-your-desk-anytime-soon/. [Accessed 2014 August 21].

[80] Stoll and Alex, "Design of Quiet Propellers," Stanford University, Stanford, CA, 2012.

[81] B. Epps, M. J. Stanway and R. W. Kimball, "OpenProp: An Open-source Design Tool for Propellers and Turbines," Massachusetts Institute of Technology, Cambridge, MA, 2009.

[82] M. Drela, "QProp," 4 November 2007. [Online]. Available: http://web.mit.edu/drela/Public/web/qprop/. [Accessed 24 August 2014].

[83] M. Drela, "QMIL User Guide," [Online]. Available: http://web.mit.edu/drela/Public/web/qprop/qmil_doc.txt. [Accessed 4 October 2005].

[84] I. P. Tracy, "Propeller Design and Analysis for a Small, Autonomous UAV," Massachusetts Institute of Technology, 2011.

[85] OpenProp, "About OpenProp," [Online]. Available: http://engineering.dartmouth.edu/epps/openprop/. [Accessed 24 August 2014].

[86] J. E. Kervin, "13.04 Lecture Notes: Hydrofoils and Propellers," January 2001. [Online]. Available: http://ocw.mit.edu/courses/mechanical-engineering/2-23-hydrofoils-and-propellers-spring-2007/course-notes/kerwin_notes.pdf. [Accessed 24 August 2014].

[87] Army Material Command, "Engineering Design Handbook Helicopter Engineering, Part One, Preliminary Design," Army Material Command, Alexandria, Virginia, 1974.

[88] APC Propellers, "17x12 Performance Data," 2013.

[89] UIUC - Gavin Ananda, "UIUC Propeller Database," [Online]. Available: http://aerospace.illinois.edu/m-selig/props/propDB.html. [Accessed 21 August 2014].

[90] P. Benham, R. Crawford and C. Armstrong, Mechanics of Engineering Materials, Essex, England: Pearson Education Limited, 1996.

[91] J. Lee and A. Huang, "Fatigue analysis of FDM materials," University of Arkansas, Fayetteville, AR, 2014?.

[92] J. P. Moore and C. B. Williams, "Fatigue Characterization of 3D Printed Elastomer Materia," Viginia Polytechnic Institute and State University, 2012.

[93] D. Franchino, "A real world glimpse at 3D printing hype," Plastics Today, 18 March 2014. [Online]. Available: http://www.plasticstoday.com/articles/real-world-glimpse-3d-printing-hype. [Accessed 21 August 2014].

[94] Stratasys, "ABS P400 Specification Sheet," Eden Prairie, MN, 2011.

[95] 3DSystems Corporation, "Duraform HST Composite," 3DSystmes, Rock Hill, SC, 2008.

[96] A. Cates, "What Ingredients Are in a Sharpie Marker?," eHow, [Online]. Available: http://www.ehow.com/about_5211769_ingredients-sharpie-marker_.html. [Accessed 21 August 2014].

[97] J. B. Brandt and M. S. Selig, "Propeller Performance Data at Low Reynolds Numbers," in *49th AIAA Aerospace Sciences Meeting* , Orlando, FL, 2011.

[98] N. R. Phelps, "Wind Tunnel Modeling of Small Electric UAV Power System Performance," California Polytechnical Institute, San Luis Obispo, 2011.

[99] R. R. Glassock, "Design, Modelling and Measurment of Hybrid Powerplant for Unmanned Aerial Vehicles," Queensland University of Technology, Queensland, 2012.

[100] D. P. Raymer, Aircraft Design: A Conceptual Approach Fourth Edition, Reston, Virginia: American Institute of Aeronautics and Astronautics, Inc., 2006.

[101] R. M. B. Bass and J. van Hengst, "Aerodynamic and Structural Aspects of Propeller and Drive for a 1/5 Scale Wind Tunnel Programme," *AGARD Conference Proceedings No. 366,* 1985.

[102] T. G. Beckwith, R. D. Marangoni and J. H. Leinhard, Mechanical Measurements, 5th ed ed., Reading, Massachusetts: Addison-Wesley Publishing Company, 1993.

[103] Linear Technology, "LTC2400 Datasheet," 1998. [Online]. Available: http://cds.linear.com/docs/en/datasheet/2400fa.pdf. [Accessed 8 August 2014].

[104] A. Devices, Op Amp Applications Handbook, W. Jung, Ed., Analog Devices, 2005.

[105] APC Propeller, "Performance Data, APC 20x13," 8 June 2013. [Online]. Available:

http://www.apcprop.com/v/downloads/PERFILES_WEB/PER3_20x13E.dat. [Accessed 24 August 2014].

[106] H. Glauert, The Elements of Aerofoil and Airscrew Theory, London: The Syndics of the Cambridge University Press, 19959.

[107] H. E. I. Payne, "Study of V/Stol Aerodynamic Static Test Facilities," US Army Transport Research and Engineering Command, Fort Eustis, Virginia, 1961.

[108] B. N. Lock, "Wind Tunnel Tests of High Pitch Airscrews, R&M 919," ARC , London, England, October 1934.

[109] Federal Premium, "V-SHOK 17 HMR," [Online]. Available: http://www.federalpremium.com/products/details/rimfire.aspx?id=367. [Accessed 30 August 2014].

[110] Winchester Ammo, [Online]. Available: http://www.winchester.com/PRODUCTS/SHOTSHELL-AMMUNITION/Advanced/AA-Shotshell/Pages/AAHLA127.aspx. [Accessed September 2014].

[111] K.-H. Denzin and A. Engel, "Stability calculations with Plane Geometry - Senior Telemaster," 19 August 2007. [Online]. Available: http://time.fh-augsburg.de/~erd/Modellflug/textDownloads.shtml#Telemaster. [Accessed 24 August 2014].

[112] AXI Model Motors, "AXI 5325/18 GOLD LIN," 2006. [Online]. Available: http://www.modelmotors.cz/index.php?page=61&product=5325&serie=18&line=GOLD. [Accessed 24 August 2014].

[113] A. Paganelli, "A Simple Arduino-Based Tachometer," 6 September 2012. [Online]. Available: http://blog.arduino.cc/2012/09/06/a-simple-arduino-based-tachometer/. [Accessed 24 August 2014].

[114] Castle Creations, "Phoenix ESC User Guide," Castle Creations, 2012.

[115] K. Myers, "The Ampeer ON-LINE! July 2012 - "Can the Data From the Castle Creations' Phoenix ICE 50 (8S) Be Used to Collect Inputs for Drive Calculator? "," Electric Flyers Only, Inc., July 2012. [Online]. Available: http://www.theampeer.org/ampeer/ampjul12/ampjul12.htm#ICE50. [Accessed 24 August 2014].

[116] UAV-Props, "Software LmPTR," [Online]. Available: http://www.uav-props.fr/LmPTR.php. [Accessed 2014 23 August].

[117] J. Sodja, R. Drazumerie and T. Kosel, "Design of Flexible Propellers with Optimized Load-Distribution Characteristics," *Journal of Aircraft,* vol. 51, no. 1, pp. 117-128, 2014.

[118] B. Boucher, "The Physics of Low Energy Flight," Astro Flight Inc., 2003.

[119] Eflite, "Power 60 Brushless Outrunner Instructions," Horizon Hobby Inc., Champaign, IL, 2006.

[120] M. J. Logan, J. Chu, M. A. Motter, D. L. Carter, M. Ol and C. Zeune, "Small UAV Research and Evolution in Long Endurance Electric Powered Vehicles," American Institute of Aeronautics and Astronautics.

[121] A. A. Regier, "Effect of the Lift Coefficient on Propeller Flutter," National Advisory Committee for Aeronautics, Washington, 1945.

[122] "Connect a LTC2400 High Precision 24 Bit Analog to Digital Converter," Academy of Media Arts Cologne, [Online]. Available: http://interface.khm.de/index.php/lab/experiments/connect-a-ltc2400-high-precision-24-bit-analog-to-digital-converter/. [Accessed 8 August 2014].

[123] W. Kester, "Strain, Force, Pressure, and Flow Measurements".

[124] U.S. Department of Transportation, Federal Aviation Administration, "Certification of Propellers (AC 35-1)," U.S. Department of Transportation, Federal Aviation Administration, 2008.

[125] N. K. Borer, "Design and Analysis of Low Reynolds Number Airfoils," 2002.

[126] J. Sodja, R. Draumeric, T. Kosel and P. Marzocca, "Design of Flexible Propellers with Optimized Load Distribution Characteristics," *Journal of Aircraft,* vol. 51 , no. 1, pp. 117-128, 2014.

[127] "Spektrum DX8 Transmitter Only MD2 (SPMR8810)," Autonomous Avionics, [Online]. Available: http://autonomousavionics.com/products/spektrum-dx8-transmitter-only. [Accessed 24 August 2014].

[128] M. Drela, "DC Motor/Propeller Matching," 3 March 2005. [Online]. Available: http://web.mit.edu/drela/Public/web/qprop/motorprop.pdf. [Accessed 24 August 2014].

Appendix A Aircraft Performance Methods

It is impossible to design an aircraft- or mission- specific propeller without knowing the thrust needed in each phase of flight or that required for a given manoeuver. This section details the methods used to determine the normal and maximum required thrust for each phase of flight and/or manoeuver and provides validation using results obtained from flight tests.

A.1 Required and Maximum Thrust

The primary purpose of analyzing the aircraft's performance is determining the thrust needed for the desired performance in typical steady atmospheric conditions, or the normal required thrust (NRT). However more thrust is needed for maneuvering or flying in unsteady atmospheric conditions (i.e. in wind gusts or through thermal currents). The maximum required thrust (MRT) is the NRT and the most thrust additionally required for sustained level flight while turning, climbing or operating with the maximum allowable head wind.

A.2 Operating Assumptions

The initial use of small UAVs for civil applications will typically be surveying missions in remote areas that require the aircraft to maintain a low and constant altitude to obtain good sensing data. Therefore, it is assumed that the UAV is being operated from a short runway and flown no higher than 1000ft above the ground in constant atmospheric conditions.

A.3 Take-Off

The maximum thrust required from a propeller typically will be when the aircraft is taking off [deHavilland, 1976]. During take-off most small UAVs are typically controlled by a pilot and "handed-over" to the autopilot once the aircraft is in level-flight. For UAVs a short take-off and landing distance is preferable for two major reasons:

- UAVs may need to be launched improvised runways on rough terrain such as farm land, the prairie or tundra. Based on the author's experience, finding or preparing a suitable stretch of unprepared ground to use as a runway is not a trivial task.
- Most UAVs lack steerable landing gear making them difficult to control until the aircraft achieves sufficient speed that the rudder becomes effective. Typically the rudder becomes effective near the take-off speed of the aircraft, and so is desirable to achieve this speed as quickly as possible.

The thrust needed to take-off and clear an obstacle within a user-defined distance is calculated. One of the most accurate methods of analyzing the take-off performance of an aircraft is the time-step method presented in [Boeing, 2009]. The time-step method considers the instantaneous change in the lift and drag coefficient as the aircraft accelerates and analyzes each phase of the take-off (the ground roll, rotation, and transition & flare) separately. This method, however, is too complicated for quickly determining the necessary thrust for a preliminary estimate. A simplified method of calculating the distance needed for the aircraft to lift-off is suggested in [Anderson, 2011]:

$$S_{LO} = \frac{(V_{LO})^2\left(W/g\right)}{2\{T - [D + \mu_r(W - L)]_{avg}\}}$$ **A. Eq. 1**

Where $V_{LO} = 1.2V_{Stall}$

This simplified method essentially uses a single time step and assumes that the thrust, drag and rolling resistance force are constant. The average of all three of these forces are assumed to occur when the aircraft is at $V_{avg} = 0.7V_{LO}$.

Most aircraft do not take-off by accelerating to the lift off speed and becoming instantaneously airborne. When the aircraft reaches a rotation speed the pilot lifts the nose landing gear off the runway and the aircraft will lift-off a few seconds later (figure 1a). However UAVs and in particular tail-dragger designs, typically take-off nearly instantaneously when they reach lift-off speed (figure 1b), as do short take-off and landing type (STOL) aircraft [deHavilland,1976][8]. Due to the similarities in their behaviour on take-off and their short take-off lengths it may be best to analyze an UAV aircraft using the same assumptions as for a STOL aircraft[9].

[8] The standard take-off detailed in the pilot operating handbook for the DHC-2 requires the pilot to keep the tail of the aircraft down until the aircraft becomes airborne. For short field take-off, the POH instead suggests that the pilot lift the tail off the ground once the aircraft reaches 40 MPH and then rotate when the aircraft is over the stall speed.

[9] After this appendix was completed a paper on RC aircraft design by Dr. Leland M. Nicolai [Nicolai,2002] was found, which suggests a similar approach to estimate the ground roll distance. The only difference is that Dr. Nicolai uses 80% of the maximum lift coefficient while the STOL approach in [McCormick, 1995] uses 70% of the maximum lift coefficient.

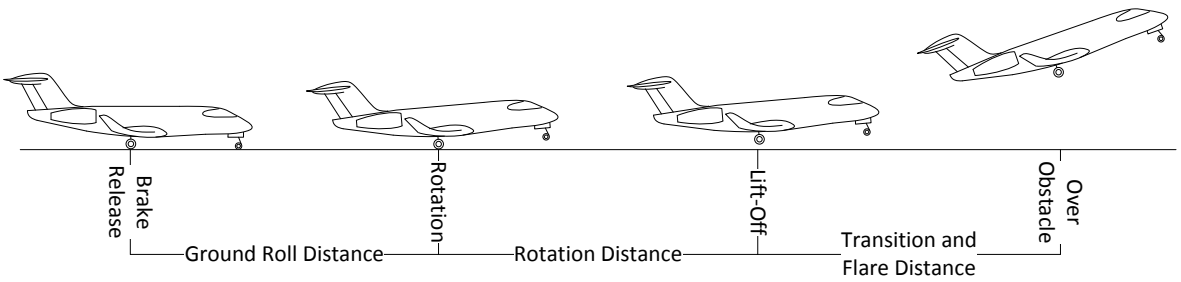

Figure A1a: Take-off stages for a conventional aircraft

(based on Anderson, 2009 & McCormick, 1995)

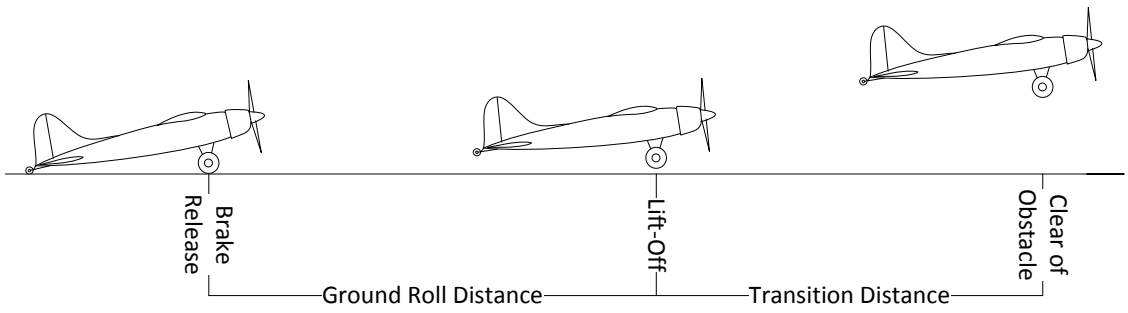

Figure A1b: Take-off of a UAV or STOL aircraft

The unique performance characteristics of STOL aircraft are obtained by having a high thrust-to-weight and high lift-coefficient [McCormick, 1995]. Assuming that the largest and only force acting on the aircraft during the take-off ground roll is the aircraft's thrust [McCormick, 1995] we have the ground roll as:

$$S_{GR} = \frac{{V_{LO}}^2}{2g\left(\frac{T}{W}\right)} \qquad \textbf{A. Eq. 2}$$

As with the simplified take-off method the aircraft's thrust is calculated at 70% of the aircraft's lift-off speed, which is assumed to be 10% above the aircraft's stall speed. As it is assumed the aircraft lifts off without needing to rotate, the transition between the ground roll and climb is neglected [McCormick, 1995]. Once airborne, the aircraft climbs at a speed 20% over stall and at a climb angle equal to [McCormick, 1995]:

$$\theta_c = \frac{T}{W} - \frac{D}{W}$$ **A. Eq. 3**

Where:

$$\frac{D}{W} = \frac{C_{Do} + \frac{{C_L}^2}{\pi A e}}{C_L}$$ **A. Eq. 4**

$$C_L = \frac{C_{L\,max}}{1.44}$$ **A. Eq. 5**

Knowing the obstacle height and assuming a constant climb angle, the airborne distance can be determined [McCormick,1995]

$$s_{ab} = \frac{h}{\frac{T}{W} - \frac{D}{W}}$$ **A. Eq. 6**

The total distance needed for take-off is:

$$S_{TO} = \frac{{V_{LO}}^2}{2g\left(\frac{T}{W}\right)} + \frac{h}{\frac{T}{W} - \frac{D}{W}}$$ **A. Eq. 7**

The effects of a head or tail wind on the take-off distance can included by changing the ground roll of the aircraft to become [McCormick,1995]:

$$S_{TO} = \frac{(V_{LO} - V_w)^2}{2gk\left(\frac{T}{W}\right)} + \frac{h}{\frac{T}{W} - \frac{D}{W}}$$ **A. Eq. 8**

Where:

$$k = \left[\frac{1}{2}\left(1 + \frac{2x + x^2}{3}\right)\right]^{1/2}$$ **A. Eq. 9**

$$x = \frac{V_w}{V_{LO} + V_w}$$ **A. Eq. 10**

If V_w is positive it is a headwind that will reduce takeoff distance while a negative V_w is a tailwind that will have the opposite effect.

If the takeoff distance equation is rearranged to find the thrust needed to obtain a given distance, the resulting expression is very long and unnecessarily difficult to use. For simplicity:

$$T = \left[\frac{A + \sqrt{A^2 - B}}{C}\right] W$$ **A. Eq. 11**

Where:

$$A = 2gk\left(S_{TO}\left(\frac{D}{W}\right) - h\right) + (V_{LO} - V_w)^2$$ **A. Eq. 12**

$$B = 8S_{TO}gk(V_{LO} - V_w)^2\left(\frac{D}{W}\right)$$ **A. Eq. 13**

$$C = 4S_{TO}gk$$ **A. Eq. 14**

The NRT is determined with the normal head/tail wind and the MRT is calculated with the maximum allowable tail wind.

The accuracy of the STOL take-off analysis was to be checked by comparing the estimated distance or thrust to flight test data for a small UAV, however, no reliable or useable data was obtained. Instead the take-off performance of a STOL aircraft, the deHavilland Canada DHC-2 Beaver was estimated and compared to published data in the flight manual. While the validity of the estimated take-off distance could have been

checked using any STOL aircraft, using a ~2300kg aircraft to validate methods for analyzing a 20-35kg UAV still may seem questionable. If the scaling rules developed by [Boucher] for RC modellers are used in reverse, the Beaver may be viewed as an "enlarged" version of a small UAV. Scaling rules were developed to allow RC modellers to build scaled models of full-sized aircraft and maintain the full-sized aircraft's flight characteristics. By applying the scale factor to the aircraft's weight, wing area, and power plant the scaled aircraft will achieve a "scaled" take-off speed in "scale" time. Using the scaling rules, the Beaver could be seen as a 400% enlarged version of a small UAV, the Corvus Demonstrator (there are many physical differences however between the two aircraft so the Beaver is not an exact scaled version of the Corvus Demostrator).

Parameter	deHavilland Canada DHC-2		Corvus Demonstrator		Scaled to Full Size Relationship	1/Scale Factor
Wing Span	14.63	[m]	3.667	[m]	1/SF	4.00
	48	*[ft]*	*12*	*[ft]*		
Gross Weight	2314	[kg]	35	[kg]	1/SF^3	4.04
	5100	*[lb]*	*77*	*[lb]*		
Wing Loading	976.8	[N/m^2]	202.5	[N/m^2]	1/SF	4.82
(at gross W)	*20.4*	*[lb/ft^2]*	*4.22*	*[lb/ft^2]*		
Installed Power	298.3	[kW]	6.15	[kW]	1/(SF^3.5)	3.03
	400	*[hp]*	*8.3*	*[hp]*		

Table A1: Scale Factors between a DHC-2 Beaver and Corvus UAV

It should also be noted that the Beaver's gross-weight-to-power ratio (7.63 kg/kW or 12.75 lb/hp) is the same as that for a 20-35kg UAV based on the historical trend presented by [Barnard].

Leading particulars of the Beaver were obtained from [deHavilland, 1976],[Johnson, 1956], and [A-806] are summarized in the table below. It was assumed that the aircraft is at its maximum take-off weight, is configured for land operations and is operating at sea level, from a hard runway, and with no wind.

	Imp.	*S.I.*
Geometry & Weight		
Wing Area	250 [ft^2]	23.2 [m^2]
Aspect Ratio	9.2	
Max. Take-off Weight	5100 [lb]	22686 [N]
CDo (T/O Config.)	0.048	
Engine		
Type	Pratt-Whitney R-985 Junior Wasp	
Max. Power	400 [BHP]	298.3 [kW]
RPM @ Max. Power	2200 RPM	
Propeller		
Make and Type	Hamilton Standard Constant Speed 2D30	
Blades	2 (6101 design)	
Diameter	8.5 [ft]	2.59 [m]

Table A2: Leading Particulars of DHC-2 Beaver

Based on the procedure for a standard takeoff detailed in the pilot's operating handbook (POH), the pilot should keep the tail of the aircraft down, allow the aircraft to become airborne at between 55-65 MPH, and climb at 65 MPH before reducing the engine from take-off power and retracting the flaps to their climb position [deHavilland, 1976]. The Beaver's POH also describes a method for a short-field takeoff, which would result in a shorter take-off distance, however specific takeoff distances were not available. The standard takeoff procedure does involve the aircraft becoming instantaneously airborne at lift off speed so it is still acceptable to use for this check. The take-off distances of the Beaver were calculated based on an International Civilian Aviation Organization (ICAO) standard where the aircraft lifts off at 120% of the stall speed in the take-off configuration [deHavilland, 1976]. Assuming that the 65 MPH take-off speed (29.06 m/s) is for a take-off weight of 5100lb, the maximum lift coefficient is:

$$C_{L\,max} = \frac{2W}{\rho S \left(\frac{V_{LOF}}{1.2}\right)^2} = \frac{2(22686)}{(1.225)(23.23)\left(\frac{29.06}{1.2}\right)^2} = 2.66 \qquad \textbf{A. Eq. 15}$$

The thrust-to-weight ratio of the Beaver on takeoff was determined by evaluating the performance of the propeller when the engine is set for takeoff power. The Beaver is powered by a single Pratt-Whitney Wasp Junior radial-engine which drives a 2-bladed Hamilton Standard constant-speed propeller [deHavilland, 1976]. From [A-806] one certified propeller-hub combination uses Hamilton Standard a 2D30 hub and 6101 propeller blades. 6101 propeller blades were tested by NACA in 1938 [TR642], but were installed in a 3-bladed hub not used on the Beaver. The 6101 is very similar in to the Navy Bureau of Aeronautics 5868-9 propeller blade which was tested and compared to the 6101 in [TR642] and tested installed in a 2-blade propeller hub in [TR640]. The major difference

between the 6101 and 5868-9 is that the 6101 has a lower thickness-chord ratio [TR642], but aside from that both blades use the same airfoil (Clark-Y) and have a very similar pitch and chord distribution. Due to its lower thickness-chord ratio, the 6101 produces approximately 8% less thrust at the low advance ratios and blade angles seen on take-off. In lieu of better data the performance of the 5868-9 was used with an 8% reduction in the thrust coefficient.

If all of the engine's power is transmitted to the propeller (none is used for electrical power), the propeller power coefficient is 0.0424, and when the aircraft is at 70% of its lift-off speed (45.5 MPH or 20.34m/s) the advance ratio is 0.214. From figure 6 in [tr640], a 2-bladed 5868-9 propeller will have a thrust coefficient of 0.09. Reducing the thrust coefficient by 8%, the propeller will produce 6136 N of thrust. The thrust-to-weight ratio is then 0.270.

All parameters necessary to calculate the drag-to-weight ratio are known with the exception of e, the Oswald efficiency factor. While this parameter could be assumed based on suggested values in literature [McCormick,1995], sufficient information exists in the POH to estimate it for when the aircraft is in the take-off configuration.

After take-off, the aircraft in take-off configuration and at maximum climbs at a speed of 730fpm (3.7 m/s) when flying at 65 MPH. From [Raymer, 2006], the rate of climb of an aircraft is:

$$V_v = \frac{P_{engine}\eta_{prop}}{W} - \frac{DV}{W} \qquad \textbf{A. Eq. 16}$$

Rearranging for drag,

$$D = \frac{P_{engine}\eta_{prop} - V_v W}{V} \qquad \textbf{A. Eq. 17}$$

When the aircraft is in climb the propeller's advance ratio is 0.306. Following the same procedure to find the thrust on take-off the propeller's thrust coefficient was estimated to be 0.0736 resulting in a propeller efficiency of 53.1%.

The drag acting on the aircraft is then:

$$D = \frac{(298.3\ kW)(0.531) - (3.7\ m/s)(22686N)}{29.06\ m/s} = 2562\ N \qquad \textbf{A. Eq. 18}$$

The drag of an aircraft is:

$$D = SqC_D = Sq\left(C_{Do} + \frac{C_L^2}{\pi Ae}\right) \qquad \textbf{A. Eq. 19}$$

When the Beaver is at 65 MPH (29.1 m/s) and gross weight its lift co-efficient is 1.89 and dynamic pressure is 517.2 Pa.

Rearranging and solving for Oswald's efficiency,

$$e = \frac{C_L^2}{\pi A}\left(\frac{D}{Sq} - C_{Do}\right)^{-1} = \frac{1.89^2}{\pi(9.2)}\left(\frac{2562}{(23.23)(517.2)} - 0.048\right)^{-1} \qquad \textbf{A. Eq. 20}$$

$$= 0.7479 \cong 0.75$$

This value agrees well with the efficiency of 0.8 suggested in [McCormick,1995] for high-wing aircraft.

The drag to weight ratio is:

$$\frac{D}{W} = \frac{C_{Do} + \frac{{C_L}^2}{\pi Ae}}{C_L} = \frac{C_{Do}}{C_L} + \frac{C_L}{\pi ARe} = \frac{0.048}{1.85} + \frac{1.85}{\pi(9.2)(0.75)} = 0.11$$ **A. Eq. 21**

Note that, as per A. Eq. 5, $C_L = \frac{C_{L\,max}}{1.44} = \frac{2.66}{1.44} = 1.85$

With all required parameters known, the take-off the DHC-2 is then estimated for a 50ft. (15.24m) obstacle as:

$$S_{TO} = \frac{V^2}{2g\left(\frac{T}{W}\right)} + \frac{h}{\frac{T}{W} - \frac{D}{W}}$$ **A. Eq. 22**

$$= \frac{\left(29.06\frac{m}{s}\right)^2}{2\left(9.80665\frac{m}{s^2}\right)(0.270)} + \frac{15.24m}{(0.270) - (0.111)}$$

$$= 159.5m + 95.85m = 255m \quad (837ft)$$

The estimated ground-roll take-off distance is close to the values stated in the aircraft's flight manual (687ft or 209m) but the STOL analysis method underestimates the distance needed to clear an obstacle (563ft or 171m) [deHavilland, 1976]. A "correction" factor may be necessary to ensure sufficient thrust is available to clear obstacles.

A.4 Best Rate of Climb

The rate of climb of an aircraft is dictated by its weight and the excess power. Excess power is difference between the power produced by the propeller (the available power) and power needed to overcome the drag acting on the aircraft (the required power). From [Raymer,2006],

$$V_v = \frac{P_{available} - P_{required}}{W} = \frac{P_{engine}\eta_{prop}}{W} - \frac{DV}{W}$$ **A. Eq. 23**

The available power can also be expressed as the product of the propeller's thrust and the speed of the aircraft. Expressing the available power as such is typically done for jet aircraft where the thrust remains nearly constant with speed. The thrust produced by the propeller will decrease with an increase in flight speed; however the variation in the propeller's efficiency – especially for a constant-speed propeller – is much less. Expressing the available power as such and rearranging for thrust:

$$V_v = \frac{P_{available} - P_{required}}{W} = \frac{TV - DV}{W} \rightarrow T = \frac{WV_v}{V} + D$$ **A. Eq. 24**

From this, the thrust needed to achieve a user-defined rate of climb can be found. The speed of the aircraft can be user-defined or may be calculated based on minimizing the required power. The minimum power required for a propeller aircraft occurs when the ${C_L}^{3/2}/C_D$ ratio is maximized [Anderson, 2011], which occurs when the induced drag coefficient is equal to three times the parasitic drag coefficient [Anderson,2011]. Based on this condition the lift coefficient of the aircraft is:

$$C_{Di} = 3C_{Do} = \frac{{C_L}^2}{\pi Ae} \rightarrow C_L = \sqrt{3C_{Do}\pi Ae}$$ **A. Eq. 25**

This lift coefficient when its speed is:

$$V_{min.req.power} = V_{climb} = \sqrt{\frac{2W}{\rho S C_L}} = \sqrt{\frac{2W}{\rho S\sqrt{3C_{Do}\pi Ae}}}$$ **A. Eq. 26**

Depending on the aircraft's drag polar this speed may be less than or very closed to the aircraft's stall speed [Raymer, 2006]. In such a case, the suggested climb speed is 20% greater than stall.

If the aircraft does not need to achieve a specific rate of climb the user may wish to design the propeller to maximize the rate of climb based on the power required for take-off. On take-off the engine/motor is set for maximum power and it is assumed the required power for take-off is close to the maximum available power of the engine. If the propeller is designed for maximum efficiency when the aircraft is in cruise, on take-off its efficiency will be poor due to the difference in rotational and forward speeds at both operating conditions. As the forward speed of the aircraft increases the propeller's efficiency will improve as it is becoming closer to operating at its design point. The difference between the average take-off and climb speed is likely sufficient for a notable increase in propeller efficiency.

The efficiency of a propeller operating in a forward flight is defined as:

$$\eta = \frac{C_T J}{C_p} \qquad \textbf{A. Eq. 27}$$

With:

$$J = \frac{V}{nD} \qquad \textbf{A. Eq. 28}$$

When the aircraft is static (V=0) both the advance ratio and efficiency are 0. If it is assumed that the efficiency of the propeller increases linearly and the efficiency at a pre-

peak advance ratio is known, the efficiency of the propeller at a pre-peak advance ratio can be estimated as:

$$\eta_{pre\ max} = \left(\frac{C_{T\ known}}{C_{p\ known}}\right) J \qquad \textbf{A. Eq. 29}$$

The increase in efficiency between the average take-off speed and climb speed is:

$$\Delta\eta = \left(\frac{C_{T\ avg\ T/O}}{C_{p\ avg\ T/O}}\right)\left(J_{climb} - J_{avg\ T/O}\right) \qquad \textbf{A. Eq. 30}$$

As:

$$C_{P\ avg\ T/O} = \frac{P_{max}}{\rho n^3 D^5} \qquad \textbf{A. Eq. 31}$$

$$J_{avg\ T/O} = \frac{V_{avg\ T/O}}{nD} \qquad \textbf{A. Eq. 32}$$

$$J_{climb} = \frac{V_{climb}}{nD} \qquad \textbf{A. Eq. 33}$$

$$C_{T\ avg\ T/O} = \frac{T_{avg\ T/O}}{\rho n^2 D^4} \qquad \textbf{A. Eq. 34}$$

Assuming no change in propeller RPM, the change in propeller efficiency is:

$$\Delta\eta = \left(\frac{T_{avg_{\frac{T}{O}}}}{P_{max}}\right)\left(V_{climb} - V_{avg_{\frac{T}{O}}}\right) \qquad \textbf{A. Eq. 35}$$

Therefore, the available power in climb will be:

$$P_{avail,climb} = (1+\Delta\eta)P_{avail,_{\frac{T}{O}}} = (1+\Delta\eta)T_{avg_{\frac{T}{O}}}V_{avg_{\frac{T}{O}}} \qquad \textbf{A. Eq. 36}$$

The maximum rate of climb and the trust needed to achieve it is:

$$V_v = \frac{P_{avail,climb} - D_{climb}V_{climb}}{W} \quad \textbf{A. Eq. 37}$$

$$T_{climb} = \frac{W\left(P_{avail,climb} - D_{climb}V_{climb}\right)}{V_{climb}W} + D_{climb} = \frac{P_{avail,climb}}{V_{climb}} \quad \textbf{A. Eq. 38}$$

To check the validity of using the available power on take-off to predict the maximum rate of climb, the climb performance of the Beaver in take-off configuration was estimated. While the Beaver uses an adjustable pitch propeller, it is assumed that the blade pitch does not change significantly from the take-off position. It is assumed the engine is set for maximum power, the aircraft is at its gross weight, and the Beaver is climbing in standard-day, sea level and no-wind atmospheric conditions.

$$C_L = \sqrt{3C_{Do}\pi Ae} = \sqrt{3(0.048)\pi(9.2)(0.75)} = 1.77 \quad \textbf{A. Eq. 39}$$

$$V_{climb} = \sqrt{\frac{2W}{\rho S C_L}} = \sqrt{\frac{2(22686\ N)}{\left(1.225\frac{kg}{m^3}\right)(23.23m^2)(1.77)}} = 30.04\frac{m}{s} \quad \textbf{A. Eq. 40}$$

On takeoff the propeller develops an estimated 6136 N when the aircraft is at 20.34 m/s. At V_{climb} the increase in efficiency is estimated to be:

$$\Delta\eta = \left(\frac{T_{avg_{\frac{T}{O}}}}{P_{max}}\right)\left(V_{climb} - V_{avg_{\frac{T}{O}}}\right) = \left(\frac{22686\ N}{298.3\ kW}\right)\left(30.04\frac{m}{s} - 20.34\frac{m}{s}\right)$$ **A. Eq. 41**

$$= 0.1995$$

The power available for climb, including the increase in efficiency is:

$$P_{avail,climb} = (1 + \Delta\eta)T_{avg_{\frac{T}{O}}}V_{avg_{\frac{T}{O}}}$$ **A. Eq. 42**

$$= (1 + 0.1995)(6136\ N)\left(20.34\frac{m}{s}\right) = 149.7\ kW$$

The maximum rate of climb and the trust needed to achieve it is:

$$P_{climb} = D_{climb}V_{climb} = \frac{1}{2}\rho S C_D (V_{climb})^3 = \frac{1}{2}\rho S(4C_{Do})(V_{climb})^3$$ **A. Eq. 43**

$$= \frac{1}{2}(1.225)(23.23)(4 \times 0.048)(30.04\ m/s)^3$$

$$= 74.06\ kW$$

$$V_v = \frac{P_{avail,climb} - D_{climb}V_{climb}}{W} = \frac{149.7\ kW - 74.06\ kW}{22686\ N} = 3.3\frac{m}{s}$$ **A. Eq. 44**

$$T_{climb} = \frac{P_{avail,climb}}{V_{climb}} = \frac{149.7\ kW}{30.04\frac{m}{s}} = 4983\ N$$ **A. Eq. 45**

The estimated climb speed (67 MPH) and maximum rate of climb (656 fpm) compare reasonably well with the figures published in the Beaver's POH (65 MPH @ 730 fpm). The actual thrust produced on takeoff, based on the analysis in the take-off performance example, is 5454 N or ~9% more than estimated, which is the reason for the difference in the maximum rate of climb. Based on the performance information published in [tr640],

there is no significant change in the propeller's blade angle when operating at the advances ratio corresponding to the take-off and climb speeds.

As the propeller is not being designed so the aircraft achieves a specific rate of climb but rather the best possible with the estimated power available the results are close enough that this method can be used without incorporating any additional factor of safety.

The NRT and MRT for when the aircraft is in climb are calculated the same way but are based on the NRT and MRT for take-off.

A.5 UAV Performance in Cruise

The propeller will likely be designed for maximum efficiency when the UAV is in cruise. Depending on the mission, the propeller may be designed for when the UAV is flying at the speed it will achieve its maximum endurance, maximum range, or at a user-specified cruise speed.

The optimum speed for the aircraft to achieve its maximum range and/or endurance may be near or below the stall speed. Small UAVs will typically operate close to the ground and the decrease altitude before the autopilot or operator can recover the UAV from the stall (typically by adding power and lowering the nose of the aircraft, which would further decrease the aircraft's altitude) may lead to aircraft crashing. To reduce the likelihood of the aircraft entering an unintentional stall (which could be caused by wind-gusts or thermals) a minimum margin of 20% over the stall speed is suggested.

A.5.1 Maximum Endurance, Range, and Design Cruise Speed

A.5.1.1 Maximum Endurance

The aircraft will achieve its maximum endurance when the power required for flight is minimized. The conditions to minimize the power required are discussed in the section on climb performance. Therefore;

$$V_{min.req.power} = V_{endurance} = \sqrt{\frac{2W}{\rho S\sqrt{3C_{Do}\pi Ae}}} \qquad \textbf{A. Eq. 46}$$

If the airplane is flying in the wind does the endurance airspeed will not change but the wind may change its ground speed. If the aircraft is to maintain the same ground speed is in a no-wind condition $V_{endurance}$ should be increased by the headwind component or decreased by the tailwind.

A.5.1.2 Maximum Range

The range of a propeller aircraft is maximized when the thrust required for flight (or drag acting on the aircraft) is minimized [Anderson,2011]. This occurs when the C_L/C_D ratio is maximized [Anderson,2011] or the induced drag coefficient is equal to the parasitic drag coefficient [Anderson,2011]. Based on this condition the lift coefficient of the aircraft is:

$$C_{Di} = C_{Do} = \frac{{C_L}^2}{\pi Ae} \rightarrow C_L = \sqrt{C_{Do}\pi Ae} \qquad \textbf{A. Eq. 47}$$

The aircraft will be flying with this lift coefficient when its speed is:

$$V_{max.range} = \sqrt{\frac{2W}{\rho S C_L}} = \sqrt{\frac{2W}{\rho S \sqrt{C_{Do}\pi A e}}}$$ **A. Eq. 48**

If the aircraft encounters a headwind the speed for maximum range increases to reduce the flight time. [McCormick,1995] states that the increase in speed needed for flight into a headwind is:

$$2\left(1+\frac{\Delta V}{V_{opt}}\right)^5 - 3\left(\frac{V_w}{V_{opt}}\right)\left(1+\frac{\Delta V}{V_{opt}}\right)^4 - 2\left(1+\frac{\Delta V}{V_{opt}}\right) + \left(\frac{V_w}{V_{opt}}\right) = 0$$ **A. Eq. 49**

As this equation is difficult to work with it is expressed as plot of $\frac{\Delta V}{V_{opt}}$ to $\frac{V_w}{V_{opt}}$ in [McCormick,1995]. This plot can be approximated as:

$$\frac{\Delta V}{V_{opt}} = -0.165555\left(\frac{V_w}{V_{opt}}\right)^4 + 0.453877\left(\frac{V_w}{V_{opt}}\right)^3 + 0.102166\left(\frac{V_w}{V_{opt}}\right) + 0.264075\left(\frac{V_w}{V_{opt}}\right)\frac{\Delta V}{V_{opt}}$$ **A. Eq. 50**

Therefore, the speed maximum range will be achieved at if the aircraft is being flown with a head wind is:

$$V_{max.range} = \sqrt{\frac{2W}{\rho S \sqrt{C_{Do}\pi A e}}}\left(1+\frac{\Delta V}{V_{opt}}\right)$$ **A. Eq. 51**

A.5.1.3 Design Cruise Speed

The speed that the aircraft will cruise at if achieving maximum range or endurance is not an issue is the design cruise speed. This speed is set by the user based on mission requirements, or can be set to the aircraft's Carson speed.

The Carson speed was developed by Prof. B.H. Carson of the U.S. Naval Academy in 1981 as an efficient way of using the available excess power when the aircraft is in cruise [Carson,1981]. When the aircraft is flown at its best-range speed the fuel consumption per unit of distance will be minimized [Carson, 1981]. However aircraft are rarely flown at this speed as pilots use the extra engine power available for good climb performance instead of faster cruise speeds [Carson,1981]. Carson found that the best rate of return on the use of excess fuel consumption for speed was obtained when the aircraft was operated at [Carson,1981]:

$$V_{Carson} = 3^{3/4}\left(V_{max.Range}\right) \quad \textbf{A. Eq. 52}$$

$$V_{Carson} = 3^{3/4}\left(\frac{2W}{\rho S\sqrt{C_{Do}\pi Ae}}\right)^{0.5}\left(1+\frac{\Delta V}{V_{opt}}\right) \quad \textbf{A. Eq. 53}$$

A.5.2 Thrust Required in Cruise

A.5.2.1 Normal Required Thrust

In steady level flight an aircraft will fly at the speed that the thrust and drag forces reach equilibrium. Given:

$$C_D = C_{Do} + \frac{{C_L}^2}{\pi A e}$$ **A. Eq. 54**

$$C_L = \frac{2W}{\rho S V^2}$$ **A. Eq. 55**

The required thrust for steady level flight at any speed is:

$$T_{R,level} = \frac{1}{2} C_{Do} S \rho V^2 + \frac{2W^2}{\rho V^2 \pi b^2 e}$$ **A. Eq. 56**

A.5.2.2 Maximum Required Thrust

The maximum required thrust (MRT) at a given speed is the NRT and the greater of either the additional thrust needed for the aircraft to climb or to complete a steady level turn.

A.5.2.2.1 Additional Thrust – Climb in Cruise

Climb performance was explained in detail in the previous section. When the aircraft is in cruise for practical operation it should have enough excess power to be capable of achieving a rate of climb of at least 400 feet per minute [Boucher,2003]. The user may wish to specify a greater climb rate if desired.

The amount of additional thrust needed to achieve a given rate of climb is:

$$\Delta \boldsymbol{T_{climb}} = \frac{\boldsymbol{W V_v}}{\boldsymbol{V}}$$ **A. Eq. 57**

A.5.2.2.2 Additional Thrust – Turning Flight

UAVs performing low-altitude surveying flights may need to turn with little-to-no loss of altitude. To accomplish this some autopilots, such as the widely-used Piccolo autopilot made by Cloud Cap (UTC Aerospace), have a turn compensation mode that will add power to maintain the commanded true airspeed and a nose-up attitude [Cloud Cap, 2005]. It is assumed that if the turn compensation mode is used, sufficient thrust to maintain the aircraft's speed and altitude is required.

In a banked turn only the vertical component of the lift generated by the wing is supporting the weight of the aircraft. To maintain level flight more lift is required, increasing the induced drag and consequently the required thrust. The additional thrust needed for a steady level banked turn is:

$$T_{R,level} = \frac{1}{2} C_{D_o} S \rho V^2 + \left(\frac{2W^2}{\rho V^2 \pi b^2 e}\right)\left(\frac{1}{cos^2(\phi)}\right) \qquad \text{A. Eq. 58}$$

Where ϕ is the bank angle of the aircraft

The Piccolo autopilot requires the user to specify limits on the allowable bank angle, and it is assumed that similar limits would be maintained when the aircraft is being flown by an operator. However, as in a banked turn less lift is available to support the weight of the aircraft (making it appear that the weight of the aircraft has increased), the stall speed increases. The stall speed an aircraft in a banked turn is:

$$V_{stall,bank} = \sqrt{\frac{2W}{\rho S C_{L\,max}}}\sqrt{\frac{1}{\cos(\phi)}} = \frac{V_{stall,level}}{\sqrt{\cos(\phi)}}$$ **A. Eq. 59**

If both the speed entering the turn and a 20% margin over stall is to be maintained, the maximum allowable bank angle is:

$$V_{entry} = 1.2V_{V_{stall,bank}} = \frac{1.2V_{stall,level}}{\sqrt{\cos(\phi_{max})}} \rightarrow \phi_{max}$$ **A. Eq. 60**

$$= cos^{-1}\left[\left(\frac{1.2V_{stall,level}}{V_{entry}}\right)^2\right]$$

The limiting bank angle is the lower of either the user-defined or the stall-defined bank angle and is used for determining the extra thrust required for a steady level turn.

A. Eq. 61

A.5.3 Comparison of Predicted Cruise Performance to Flight Test Data

To check the validity of the methods detailed above, the cruise performance of a small UAV was analyzed and compared to flight test data. [Oster,2006] examines using flight test data to determine the drag polar of the Unicorn, a small foam flying-wing -type UAV made by Procerus Technologies (a division of Lockheed Martin). The Unicorn is significantly smaller than the 20-35kg UAVs that are the focus of this work, however this was not considered to be an issue as the Reynolds numbers and operating speeds of the Procerus are closer to the intended size of UAVs than a full size aircraft.

Weight	9.34	[N]
Mass	*0.952*	*[kg]*
Span	1.06	[m]
Area	0.321	[m^2]

Table A3: Procerus Technologies Unicorn Dimensions[Ostler,2006]

[Ostler, 2006] found from flight test data two drag polars to represent the aerodynamic performance of the Unicorn:

$$C_D = 0.015 + 0.13{C_L}^2 \quad \textbf{A. Eq. 62}$$

$$C_D = 0.020 - 0.06C_L + 0.22{C_L}^2 \quad \textbf{A. Eq. 63}$$

The drag polar for an aircraft can be expressed as $C_D = C_{Do} + K_2 C_L + K_1 {C_L}^2$. If it is assumed that the least drag occurs when the aircraft has a lift coefficient of zero it can be simplified to become $C_D = C_{Do} + K{C_L}^2$. [Ostler,2006] found the complex form closely reflected the performance of the aircraft and so it will be used for comparison.

If the actual drag polar is not known it would need to be estimated by the user. As the Unicorn is essentially a swept wing this is fairly simple for this aircraft. Flying wing aircraft typically use a reflexed airfoil [Raymer,2006] and it is assumed that one is used the N60R, a reflexed 12% thick airfoil is used for the Unicorn. The no-lift drag coefficient of this airfoil at a Reynold's number of 168,000 is found in [McCormick, 1995] to be 0.020. The aspect ratio was calculated to be 3.5, and its Oswald efficiency was assumed to be 0.9 (this assumption was based on that the swept wings of jet aircraft

have Oswald efficiencies of between 0.85 and 0.95 [Boeing, 2009]) . The estimated drag polar for the aircraft is:

$$C_D = 0.020 + \frac{{C_L}^2}{\pi(3.5)(0.9)} \cong 0.020 + 0.10{C_L}^2 \qquad \textbf{A. Eq. 64}$$

The required thrust predicted by both the estimated and experimentally determined drag polars and the actual thrust required for flight between the aircraft's stall and maximum speeds (10.5 m/s and 24 m/s) is shown below. The maximum required thrust was calculated based the estimated drag polar and on a climb rate of at 400 fpm at all speeds, and is also shown. The estimated drag polar over-predicts the thrust required but is still reasonably close to the actual thrust required for flight. The estimated drag polar was by no means carefully crafted (as evidenced by the assumptions made) and could have easily under-predicted the thrust required. However, given the large additional margin of thrust available to achieve at least a 400 fpm climb rate, if the drag polar did under-predict the thrust required sufficient thrust likely still would have been available for flight.

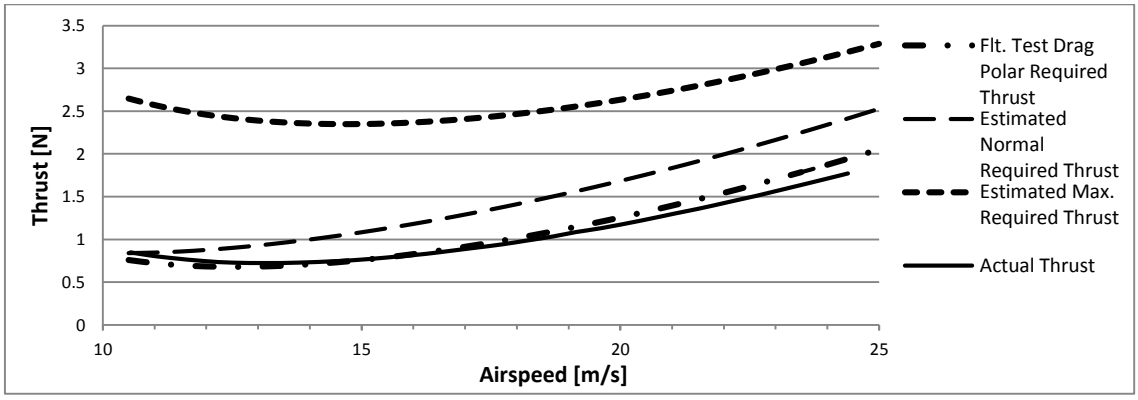

Figure A3: Comparison of Estimated and Actual Thrust Required for Procerus Technologies Unicorn UAV

From the estimated and experimentally determined drag polar the optimum speeds for maximum endurance and range and the normal required thrust at both were calculated and compared to flight test data. The estimated drag polar underestimates both the speeds needed for maximum range and endurance, however as both occur near or below stall the propeller would have to been designed for a 20% over-stall speed (12.6 m/s). While the propeller performed well at the true best endurance and range speeds, accurate flight test data will help to avoid having to later redesign the propeller to reflect the aircraft's actual performance characteristics.

	Estimated		**Flt. Test. Determined Polar**		**Flt. Test. Data**	
	Speed [m/s]	**Thrust [N]**	**Speed [m/s]**	**Thrust [N]**	**Speed [m/s]**	**Thrust [N]**
Maximum Endurance	7.85 (*12.6)	0.84 (*0.91)	10.85	0.73	11.25	0.78
Maximum Range	10.33 (*12.6)	0.97 (*0.91)	12.55	0.68	13.19	0.73

Table A7: Estimated and Actual Optimum Flight Speeds,

References:

Boeing Commercial Aircraft, D6-1420 - Jet Transport Performance Methods , 3ed., Boeing, 2009

Anderson, John D. , Introduction to Flight, 7 ed., McGraw-Hill, 2011

deHavilland Aircraft of Canada Ltd, PSM 1-2-1 DHC-2 Beaver Flight Manual, 1976

B. W. McCormick, Aerodynamics, Aeronautics, and Flight Mechanics, 2 ed., Wiley Ltd, 1995

Nicolai, Dr. Leland M, Estimating RC Model Aerodynamics and Performance, 2002

Boucher, Bob, Understanding Scale Speed, 2005 AstroFlight. Inc.

Barnard Microsystems, UAV Design Guidelines, 18 August 2014. [Online]. Available: http://www.barnardmicrosystems.com/UAV/uav_design/guidelines.html.

Johnson, GW, AGARD-R-81 Factors Affecting the Field Length of STOL Aircraft, NATO, 1956

Department of Transportation Federal Aviation Administration, Aircraft Specification No. A-806, Rev. 24, June 2, 2010

E. P. Hartman and D. Biermann, "TR-640 The aerodynamic characteristics of full-scale propellers having 2, 3, and 4 blades of Clark y and R.A.F. 6 airfoil sections," National Advisory Committee on Aeronatics, 1938

D. H. E. P. Biermann, "TR 642 - Tests of five full-scale propellers in the presence of a radial and a liquid-cooled engine nacelle, including tests of two spinners," National Advisory Committee on Aeronautics, 1938

D. P. Raymer, Aircraft Design: A Conceptual Approach Fourth Edition, Reston, Virginia: American Institute of Aeronautics and Astronautics, Inc., 2006.

Carson, B.H. Fuel Efficiency of Small Aircraft, AIAA 80-1847, 1980

B. Boucher, The Physics of Low Energy Flight, Astro Flight Inc., 2003.

Cloud Cap Technology, Piccolo System User Guide, V 3.0, April 2005

Ostler, Jon Neal, Flight Testing of Small, Electric Powered Unmanned Aerial Vehicles, Brigham Young University, 2006

Appendix B Brushless Direct-Current Motor Analysis & Optimization

A large number of small UAVs and RC aircraft use brushless direct-current (BLDC) motors to drive their propellers. While propellers can be designed for optimal efficiency at any rotational or forward speed if the motor is unable to efficiently provide power it can may negate any benefit offered by an optimized propeller and cause the overall efficiency of the aircraft's propulsion system to suffer. BLDC motors are a variant of brushed DC electric motors that use electrical commutation controlled by an electronic speed controller (ESC) rather than mechanical brushes [Padmaraja,2003]. Electrical commutation is allows for a BLDC motor to provide its rated power at any rotational speed, higher efficiency, less noise, and a longer operating life [Padmaraja,2003]. For this reason BLDC motors are increasingly being used in automotive, aerospace, industrial automation and consumer appliances [Padmaraja,2003]. A detailed examination of the design and operation of a BLDC motor is not within the scope of this work and the reader is referred to [Kirtley et al, 1998] or [Padmaraja,2003] for a full description of the topic.

B.1 Basic BLDC Motor Analysis

The purpose of any electric motor is to convert electrical energy into mechanical power [Maxon,2011]. Some electrical energy is lost in the conversion process due to electrical loses (from the resistance in the motor's windings), and mechanical losses (from the friction in the motor's bearings). Heat is generated due to the resistance in the motor's windings that will also increase the electrical resistance of the motor and reduce the effectiveness of the magnets increasing electrical losses producing less torque. Predicting the decrease in magnetism is difficult without detailed information about the motor's construction and for this research this

effect is neglected. While detailed methods for the analysis of BLDC motors are available in [motor handbook] a simplified analysis based on [Ehsani et al, 2010] and [Maxon] is used.

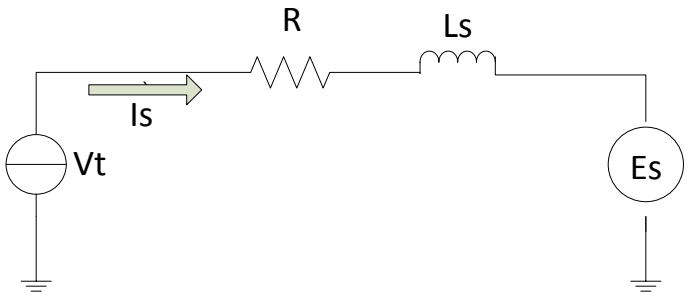

Figure B1: The electrical equivalent circuit of a BLDC motor [Ehsani et al, 2010]

From figure B1, the governing equations of the equivalent electrical circuit of a BLDC motor are [Ehsani et al, 2010]:

$$V_t = I_s R + L_s \frac{dI_s}{dt} + E_s \qquad \textbf{A. Eq. 65}$$

$$E_s = k_E \omega_r \qquad \textbf{A. Eq. 66}$$

$$T_e = k_T I_S \qquad \textbf{A. Eq. 67}$$

$$T_e = T_L + J\frac{d\omega_r}{dt} + B\omega_r \qquad \textbf{A. Eq. 68}$$

For steady state motor operation (shaft speed is constant), T_e and V_t can be simplified to become:

$$V_t = I_s R + E_s \qquad \textbf{A. Eq. 69}$$

$$T_e = T_L + B\omega_r \qquad \textbf{A. Eq. 70}$$

B.1.1 Shaft Speed

The rotational speed of the motor's shaft is based on the voltage and current supplied to the motor and can be calculated by combining equations 66 and 69:

$$V_t = I_s R + k_E \omega_r \quad \textbf{A. Eq. 71}$$

$$\omega_r = \frac{(V_t - I_s R)}{k_E} \quad \textbf{A. Eq. 72}$$

Note that ω_r is in radians per second and so k_E is in volt per radian-per-second. Typically, the voltage-to-rotational speed relationship for a motor is provided as RPM per volt, (represented as K_V) and k_E can be calculated as:

$$k_E = \frac{30}{K_V \pi} \quad \textbf{A. Eq. 73}$$

To avoid having to find k_E, the rotational speed of a motor in RPM using K_V is:

$$N = K_V (V_t - I_s R) \quad \textbf{A. Eq. 74}$$

B.1.2 Mechanical Torque

The torque delivered by the motor to the load can be calculated by re-arranging equation (1b-s) and combining it with equations 67 and 72:

$$T_L = T_e - B\omega_r \quad \textbf{A. Eq. 75}$$

$$T_L = k_T I_S - B\omega_r = k_T I_S - B\frac{(V_t - I_s R)}{k_E} \quad \textbf{A. Eq. 76}$$

The second term in 76 is the torque needed to overcome the mechanical resistance in the motor. Typically the manufacturer does not provide the resisting torque of the motor, B, but the no-load

current (I_{o0}) at a given terminal voltage (V_0) is usually given. Rearranging 76, setting T_L=0, and letting $I_S = I_o$ and $V_t = V_o$,

$$0 = k_T I_o - B\frac{(V_o - I_{o0}R)}{k_E} \quad \textbf{A. Eq. 77}$$

$$B = \frac{k_E k_T I_{o0}}{V_o - I_o R} \quad \textbf{A. Eq. 78}$$

Once B has been calculated, the no-load current for any terminal voltage is:

$$I_o = \frac{BV_t}{k_E k_T + BR} \quad \textbf{A. Eq. 79}$$

Note that as $\frac{k_T}{k_E} = 1$, $k_T = k_E$.

If the no-load current is known the torque delivered to the motor can be expressed as:

$$T_L = k_T(I_S - I_o) \quad \textbf{A. Eq. 80}$$

B.1.3 Shaft Power

The shaft power is the product of the torque delivered to the load and the rotational speed of the shaft.

A. Eq. 81

As $k_T = k_E$

$$P_L = I_s V_t - {I_s}^2 R - B\left(\frac{(V_t - I_s R)}{k_E}\right)^2 \quad \textbf{A. Eq. 82}$$

B.1.4 Thermal Effects

The heat produced when the motor is operating changes the internal resistance of the windings and the operating efficiency of the motor. The resistance of the windings including thermal effects is [Drela, 2006]:

$$R = R_o(1 + \alpha\Delta T) \qquad \textbf{A. Eq. 83}$$

R_o is the resistance at a reference temperature, α is the fractional increase in resistance with respect to temperature (for copper, α = 0.0042/C^o), ΔT is the increase in temperature over the reference temperature [Drela, 2006]. The resistance of the motor's winding can also be expressed as [Drela, 2006]:

$$R = R_o + R_t {I_s}^2 \qquad \textbf{A. Eq. 84}$$

where

$$R_t = \frac{R_o \alpha \Delta T_{max}}{{I_{max}}^2} \qquad \textbf{A. Eq. 85}$$

For determining R_t the maximum continuous allowable current and the lower of either the maximum rated temperature of the magnets is used. For most motors the maximum rated temperature for the magnets is between 80-100 ^{o}C but for some motors can reach up to 180-200 ^{o}C [Scorpion Power]. The reference temperature was the temperature of the windings when their resistance was measured and can be assumed to be 25 ^{o}C.

Thermal effects become significant when large currents are being passed through the motor, however including them may complicate the analysis. For a quick estimate or if the motor's maximum rated temperature is unknown they may be neglected.

B.2 Simplified BLDC Motor Optimization

For any given rotational speed the motor will achieve its maximum efficiency when producing a certain amount of shaft power. Ideally, a propeller can be designed for its maximum efficiency when absorbing this optimum shaft power. A method for determining the optimal torque –speed curve of a BLDC motor is provided in [Kirtley et al, 1998], but as it requires details about the motor's construction not often provided by the motor's manufacturer a simpler method is instead used.

B.2.1 Optimum Shaft Power with Thermal Effects Neglected

The efficiency of a motor is the ratio of the mechanical power produced by the motor to the electrical power provided to the motor. From equation 82

$$\eta = \frac{P_l}{P_{elec}} = \frac{I_s V_t - {I_s}^2 R - B\left(\frac{(V_t - I_s R)}{k_E}\right)^2}{I_s V_t} = 1 - \frac{I_s R}{V_t} - \frac{B}{I_s V_t}\omega^2$$ **A. Eq. 86**

As defined in (10), the efficiency of the motor can change with respect to the terminal voltage and the current supplied to the motor. If the motor is to be run at a fixed speed however, the terminal voltage becomes a function of the supply current, from equation 69

$$V_t = I_s R + k_E \omega_r$$ **A. Eq. 87**

Substituting equation 87in to 86 and simplifying,

$$\eta = 1 - \frac{I_s R}{I_s R + k_E \omega_r} - \frac{B}{I_s (I_s R + k_E \omega_r)} \left(\frac{I_s R + k_E \omega_r - I_s R)}{k_E} \right)^2 \quad \textbf{A. Eq. 88}$$

$$\eta = 1 - \frac{I_s R}{I_s R + k_E \omega_r} - \frac{B {\omega_r}^2}{I_s (I_s R + k_E \omega_r)} \quad \textbf{A. Eq. 89}$$

To determine the supply current needed for peak efficiency the derivative of equation 89 with respect to the supply current is taken to find $\frac{\partial \eta}{\partial I_s}$. The peak efficiency occurs when $\frac{\partial \eta}{\partial I_s} = 0$, and so from the derivative of 89,

$$I_s = \frac{\omega_r \left(BR + \sqrt{B^2 R^2 + BR {k_e}^2} \right)}{R k_e} \quad \textbf{A. Eq. 90}$$

Substituting equation 90 into 87, the terminal voltage necessary for peak efficiency at a given rotational speed is:

$$V_t = \frac{\omega_r \left(BR + k_e^2 + \sqrt{B^2 R^2 + BR {k_e}^2} \right)}{k_e} \quad \textbf{A. Eq. 91}$$

The optimum power output can be determined by substituting equations 90 and 91 into Eq 82. At a given rotation speed, the optimum power output is:

$$P_{Lopt} = \frac{{\omega_r}^2 \sqrt{B} \sqrt{BR + {k_e}^2}}{\sqrt{R}} \quad \textbf{A. Eq. 92}$$

The maximum efficiency of the motor, substituting Eq 90 and Eq 91 into Eq 82,

$$\eta = \frac{\sqrt{B}\sqrt{R}\sqrt{BR + {k_e}^2} \left({k_e}^2 \right)}{\left(BR + \sqrt{B}\sqrt{R}\sqrt{BR + {k_e}^2} \right) \left(BR + \left({k_e}^2 \right) + \sqrt{B}\sqrt{R}\sqrt{BR + {k_e}^2} \right)} \quad \textbf{A. Eq. 93}$$

As indicated by Eq 153, the peak efficiency of the motor is a function of the mechanical and electrical losses in the motor and is constant for all rotational speed. This however neglects the thermal losses that have not yet been included.

B.2.2 Optimum Shaft Power with Thermal Effects Included

Thermal effects can be included by substituting the increase in resistance with respect to current draw Eq 146 into Eq 149. Then, as with the constant-resistance case, the optimum shaft power can be found by taking the derivative of (149), setting it to zero, and finding the current needed.

Substituting (146) into (149):

$$\eta = 1 - \frac{I_s\left(R_o + R_t {I_s}^2\right)}{I_s\left(R_o + R_t {I_s}^2\right) + k_E\omega_r} - \frac{B{\omega_r}^2}{I_s\left(I_s\left(R_o + R_t {I_s}^2\right) + k_E\omega_r\right)} \qquad \textbf{A. Eq. 94}$$

$$\eta = 1 - \frac{I_s R_o + R_t {I_s}^3}{I_s R_o + R_t {I_s}^3 + k_E\omega_r} - \frac{B{\omega_r}^2}{{I_s}^2 R_o + R_t {I_s}^4 + I_s k_E\omega_r} \qquad \textbf{A. Eq. 95}$$

$$= \frac{\omega_r(I_s k_E - B\omega_r)}{I_s\left(I_s R_o + R_t {I_s}^3 + k_E\omega_r\right)}$$

Taking the derivative of equation 95 and setting it to 0,

$$\frac{\partial\eta}{\partial I_s} = \frac{\omega_r\left(2B\omega_r I_s R_o + 4B\omega_r R_t {I_s}^3 + B{\omega_r}^2 k_E - 3{I_s}^4 R_t k_E - {I_s}^2 R_o k_E\right)}{{I_s}^2\left(I_s R_o + R_t {I_s}^3 + k_E\omega_r\right)^2} = 0 \qquad \textbf{A. Eq. 96}$$

As this equation is difficult to solve explicitly it is best solved iteratively where I_s is varied until equation 95 is suitably close to zero. Equation 90 can be used for an initial value of I_S. After the supply current is found the motor's resistance is determined using equation 86 and the terminal voltage, shaft torque, and output power can be found with the equations 69, 80, 82 and respectively.

B.3 Comparing Predicted and Actual Motor Performance

To check the accuracy of the analysis methods presented for two BLDC motors the actual and estimated performance of was compared. The S-4035-460KV and the S-5535-190KV (table 1) were made by Scorpion Power Systems and are no longer in production, having been replaced by newer versions (the HKIII-4035-450KV and the SII-5535-190KV). These motors were selected for analysis as they are suitable for a 20-35kg UAV – the S-4035 is suitable for a ~20kg UAV and the S-5535 would be appropriate for a ~28kg UAV based on the historical installed power trend provided in [Banard].

		S-4035-460KV	S-5535-190KV
Manufacturer		Scorpion Power Systems	
Kv	[RPM/V]	460	190
Max. Voltage	[V]	40.7	44.4
Max. Continuous Current	[A]	75	90
Max. Continuous Power	[W]	2800	3800
No-Load Current	[A]	1.7	1.56
No-Load Voltage	[V]	10	10
Resistance	[R]	0.02	0.024
Max. Rated Temperature	[OC]	180	180
Calculated motor constants			
B	[Nm/(rad/s)]	7.3511E-05	3.9554E-04
Rt	[ohms/A2]	2.3147E-06	1.9289E-06
Ke	[V/(rad/s)]	2.0759E-02	5.0259E-02

Table 1: Properties of motors selected for evaluation

Data from Scorpion Power included the voltage and current supplied to the motor, shaft speed, the make and model of the propeller, and the thrust generated. As the torque generated by the motor was not provided it was estimated using propeller performance data available from APC, the manufacturer of the propellers used by Scorpion for testing both motors. The performance of a motor or engine is usually determined experimentally with a dynamometer, which measures the shaft speed when the motor or engine is producing a known torque. In the absence of

dynamometer data the torque needed to spin the propeller at a given speed was instead used to estimate the output power. However, the propeller performance data was likely estimated using an analysis program rather than obtained through testing as the performance of several propellers in static conditions (when the propeller is not moving forward) was listed as “nan” (Not A Number). As it was assumed that both motors and propellers were tested under static conditions for a “nan” entry the propeller’s power, torque, and thrust was linearly extrapolated from the data for the two lowest advance ratios.

As for both motors the thrust generated by the propeller during the testing was reasonably close to APC’s predictions (typically within 10%) it was assumed the propeller torque and power during testing were also close to APC’s predictions and could be used for checking the motor’s performance. This assumption was further supported as for the S-4035 motor a plot of the APC-predicted torque with respect to the input current at all three terminal voltages showed the strong near-linear trend which is what would be expected based on equation 76. However for the S-5535 the estimated power needed to spin the propeller was often greater or very close to the power supplied to the motor, the estimated propeller torque is likely different than the actual torque produced by the motor.

For both motors, thermal effects were considered when predicting the motor’s performance.

B.3.1 Predicted and Actual Performance of the S-4035-460KV Motor

Scorpion Power tested the S-4035 motor with 8”-15” diameter propellers at three constant terminal voltages (22, 28, and 35 volts) (Table 2A&2B). Data at a fourth terminal voltage (42V) was available, however it was not used as the behavior of the motor and propeller did not seem

reasonable[10]. As the voltage provided to the motor will vary when the aircraft is in flight (to control the speed of the propeller), examining the motor's performance at a several voltages allowed for a better examination of the analysis methods under realistic operating conditions. At all three voltages the shaft speed was over-predicted by ~3-6%, with a greater over-prediction as the current increased. As the current draw increases the magnets may start to become demagnetized from the heat, causing a reduction in the speed constant. The predicted torque for most operating cases at all voltages was within 5-10% of the torque suggested by APC, however as the operating efficiency of the motor in some operating points was 95-97% - which is exceptionally high - it is likely that the actual propeller torque was less than suggested by APC. The ratio between the predicted and actual torque varied by +/- 5-10% and with a scattered distribution (there was typically a 5-10% difference between ratios at any two operating points). Despite the scatter, the torque generally became slightly more over-predicted as the current increased. As a result of the over-prediction of the motor's speed and the scattered over/under-prediction of the torque, the predicted motor power was typically within +/- 10-15% of the actual motor power. Both the actual and predicted operating efficiency of the motor decreased as the terminal voltage (and consequently, shaft speed) increased as would be expected due to greater electrical and frictional loses, but the decrease in actual efficiency was greater than was predicted. For all three terminal voltages the actual optimum power output was different than predicted, usually occurring at a current much lower than predicted.

[10] At 42 V the motor's shaft speeds were very close to what was seen when the terminal voltage was 28V, despite a nearly-identical current draw (meaning no change in electrical losses). The Scorpion-provided test data also showed most propellers generated nearly twice the thrust than they did at 30-40% faster speeds.

B.3.2 Predicted and Actual Performance of the S-5535-190KV Motor

The performance of the S-5535-190 motor was examined to assess the influence of the motor torque/speed constant (Table 3A&3B). Test data was collected by Scorpion using 14"-24" APC propellers at 35 and 42 volts. However APC's propeller performance data indicated that the propeller often required more power than was supplied to the motor. This could be due to the current or voltage supplied to the motor being erroneous or the required propeller torque being much less than estimated by APC. The shaft speed was over-predicted by 1%-14% and with the same behavior as with the S-4035 (it was over-predicted more as the current increased), so the true voltage and power supplied to the motor are likely close to the values provided by Scorpion Power. Despite that the thrust measured in testing was generally within 5% of what was predicted by APC, the torque estimated by APC is likely greater than what is necessary for the propeller, and in the absence of reasonable data a comparison between the predicted and actual shaft power and torque is not possible.

B.3.3 Conclusions

The methods provided are sufficient to allow for a reasonably accurate approximation of the motor's performance, however if actual motor performance data is available the user is recommended to use it. If possible, [Drela (2)] provides methods to determine the constants needed to analyze the motor's performance which would allowing for a better analysis by using properties of a specific motor rather than standard ones given by the manufacturer.

The difference between the expected and actual shaft speed and the uncertainty about the actual shaft torque produced by the motor strongly suggests that when testing a propeller and/or motor

the shaft speed and propeller torque should be measured using some independent means (i.e. not using the data from the electronic speed controller (ESC)) if possible. This will allow the validity of the ESC to be checked and for the actual torque produced by the motor to be measured for a better assessment of the motor analysis methods.

References

Yedamale, Padmaraja, AN 885 Brushless DC (BLDC) Motor Fundamentals, Microchip, 2003, Available at http://www.mouser.com/pdfdocs/BrushlessDCBLDCMotorFundamentals.PDF

James L. Kirtley, Jr., H. Wayne Beaty, Nirmal K Ghai, Steven B Leeb, Richard H. Lyon, Electric Motor Handbook, McGraw Hill, 1998

Maxon Motor, maxon DC and maxon EC motor Key information , May 2011. Available at http://www.maxonmotor.com/medias/sys_master/8804419338270/DC-Das-wichtigste-ueber-maxonmotoren-11-DE-EN-ES-036-1.pdf?attachment=true

Mehrdad Ehsani, Yimin Gao, Ali Emadi, Modern Electric, Hybrid Electric, and Fuel Cell Vehicles, 2 ed. CRC Press, 2010

Mark Drela, Second-Order DC Electric Motor Model, MIT Aero & Astro, March 2006

Mark Dreal DC Motor Measurement, available at http://web.mit.edu/drela/Public/web/qprop/motor_measure.pdf

Scorpion Power Systems, Brushless Outrunner Motors , August 24, 2014 , http://www.scorpionsystem.com/info/brushless_outrunner_motors/

Barnard Microsystems, UAV Design Guidelines, 18 August 2014. [Online]. Available: http://www.barnardmicrosystems.com/UAV/uav_design/guidelines.html

All test data related to the two motors is the work of Scorpion Power Systems and was made available on their website www.scorpionsystem.com . This data is no longer available but was accessed on February 26, 2014

All the performance characteristics of the APC propellers is the work of APC propellers and is available at http://www.apcprop.com/v/downloads/PERFILES_WEB/datalist.asp

	Scorpion Test Data					Predicted Motor Performance				APC Predicted Prop Performance			Efficiency	
Propeller	**Voltage**	**Current**	**Power Supply**	**Shaft Speed**	**Thrust**	**Resistance**	**Shaft Speed**	**Torque**	**Shaft Power**	**Shaft Power**	**Torque**	**Thrust**	**Estimated**	**Actual**
(APC)	*[V]*	*[A]*	*[W]*	*[RPM]*	*[gram force]*	*[ohm]*	*[RPM]*	*[Nm]*	*[W]*	*[W]*	*[Nm]*	*[gram force]*	*[%]*	*[%]*
11 x 5.5E	22	18.3	402.6	9592	1600	0.0208	9945	0.303	315.9	389.2	0.385	1661	78.47%	96.67%
12 x 6E		25.8	567.6	9405	2400	0.0215	9864	0.460	474.8	553.8	0.559	2232	83.65%	97.57%
13 x 6.5E		38.4	844.8	9112	3000	0.0234	9706	0.722	734.3	731.1	0.764	2825	86.92%	86.54%
13 x 8E		47.4	1042.8	8911	3200	0.0252	9571	0.910	912.3	876.8	0.937	3036	87.49%	84.08%
14 x 7E		80.9	1779.8	8203	3300	0.0351	8812	1.612	1487.2	*758.3*	*0.878*	*3041*	*83.56%*	*42.60%*
15 x 10E		84.8	1865.6	8147	5100	0.0366	8691	1.693	1541.2	1576.8	1.839	4661	82.61%	84.52%
9 x 5E	28	17.8	498.4	12348	1700	0.0207	12710	0.272	361.6	416.0	0.323	1495	72.55%	83.47%
10 x 5E		19.8	554.4	12280	2400	0.0209	12690	0.313	416.4	527.1	0.409	1911	75.11%	95.07%
11 x 5.5E		28.6	800.8	12051	3100	0.0219	12592	0.497	655.1	781.7	0.620	2563	81.80%	97.61%
12 x 6E		43.3	1212.4	11667	4000	0.0243	12395	0.803	1042.9	1087.1	0.887	3513	86.02%	89.66%
13 x 6.5E		65.4	1831.2	11204	4700	0.0299	11980	1.265	1587.6	1411.3	1.200	4419	86.70%	77.07%
13 x 8E		82.9	2321.2	10826	5000	0.0359	11511	1.632	1967.6	1697.4	1.493	4611	84.77%	73.13%
8 x 6E	35	25.9	906.5	15277	1400	0.0216	15843	0.416	689.7	566.8	0.354	1577	76.08%	62.53%
9 x 6E		31.5	1102.5	15138	2600	0.0223	15777	0.532	879.7	904.0	0.570	2492	79.79%	82.00%
10 x 5E		35.1	1228.5	15072	3300	0.0229	15731	0.608	1000.9	997.5	0.632	2935	81.47%	81.20%
11 x 5.5E		52.3	1830.5	14603	4300	0.0263	15467	0.967	1565.6	1448.0	0.944	3989	85.53%	79.11%
12 x 6E		76.2	2667.0	13986	5300	0.0334	14928	1.467	2293.2	1944.9	1.326	5196	85.98%	72.92%
12 x 8E		96.7	3384.5	13515	5400	0.0416	14248	1.898	2831.4	2748.5	1.935	5753	83.66%	81.21%

Table 2A: Predicted and Actual Performance of the S-4035-460KV Motor

		Predicted/Actual		
Propeller	**Voltage** *[V]*	**Shaft Speed**	**Torque**	**Shaft Power**
11 x 5.5E	22	1.037	0.787	0.812
12 x 6E		1.049	0.822	0.857
13 x 6.5E		1.065	0.946	1.004
13 x 8E		1.074	0.971	1.041
14 x 7E		1.074	*1.835*	*1.961*
15 x 10E		1.067	0.921	0.977
9 x 5E	28	1.029	0.840	0.869
10 x 5E		1.033	0.766	0.790
11 x 5.5E		1.045	0.801	0.838
12 x 6E		1.062	0.906	0.959
13 x 6.5E		1.069	1.055	1.125
13 x 8E		1.063	1.093	1.159
8 x 6E	35	1.037	1.176	1.217
9 x 6E		1.042	0.934	0.973
10 x 5E		1.044	0.962	1.003
11 x 5.5E		1.059	1.024	1.081
12 x 6E		1.067	1.106	1.179
12 x 8E		1.054	0.981	1.030

Table 2B: Predicted and Actual Performance of the S-4035-460KV Motor

	Scorpion Test Data					Predicted Motor Performance				APC Predicted			Efficiency	
Propeller	**Voltage**	**Current**	**Power Supply**	**Shaft Speed**	**Thrust**	**Resistance**	**Shaft Speed**	**Torque**	**Shaft Power**	**Shaft Power**	**Torque**	**Thrust**	**Estimated**	**Actual**
(APC)	*[V]*	*[A]*	*[W]*	*[RPM]*	*[gram force]*	*[ohm]*	*[RPM]*	*[Nm]*	*[W]*	*[W]*	*[Nm]*	*[gram force]*	*[%]*	*[%]*
15 x 10E		22.6	791.0	6468	2800	0.0212	6559	0.864	593.6	723.9	1.041	2857	75.04%	91.52%
16 x 12E		33.6	1176.0	6232	3000	0.0226	6506	1.419	966.9	1068.0	1.615	3510	82.22%	90.81%
17 x 12E		36.7	1284.5	6165	4000	0.0231	6489	1.576	1070.7	1326.6	2.034	4301	83.36%	103.28%
18 x 12E		46.1	1613.5	6003	5100	0.0249	6432	2.051	1381.1	1549.0	2.463	5159	85.60%	96.00%
19 x 12E	35	48.3	1690.5	5962	6700	0.0254	6417	2.162	1452.6	1908.6	3.050	6272	85.93%	112.90%
20 x 12E		58.2	2037.0	5798	7200	0.0278	6342	2.662	1768.2	2045.2	3.341	7256	86.81%	100.40%
21 x 12E		61.7	2159.5	5716	8700	0.0288	6312	2.840	1877.0	2302.1	3.804	8314	86.92%	106.60%
22 x 12E		72.6	2541.0	5506	9200	0.0322	6206	3.392	2204.2	2384.9	4.075	8779	86.75%	93.86%
24 x 12E		85.2	2982.0	5310	11900	0.0368	6054	4.031	2555.9	2940.5	5.206	10992	85.71%	98.61%
14 x 10E		27.1	1138.2	7666	2700	0.0217	7868	1.036	853.7	929.6	1.147	3099	75.01%	81.67%
15 x 10E		32.3	1356.6	7563	3800	0.0224	7842	1.299	1066.4	1226.4	1.532	3983	78.61%	90.41%
16 x 12E		46.6	1957.2	7233	4400	0.0250	7758	2.021	1641.8	1862.0	2.434	4842	83.88%	95.14%
17 x 12E		50.3	2112.6	7185	5500	0.0259	7733	2.208	1787.8	2260.7	2.984	5960	84.63%	107.01%
18 x 12E	42	65.7	2759.4	6889	6500	0.0300	7606	2.987	2379.0	2478.6	3.420	6925	86.22%	89.82%
19 x 12E		67.3	2826.6	6864	8800	0.0305	7590	3.068	2438.6	2823.3	3.911	8340	86.27%	99.88%
20 x 12E		78.9	3313.8	6661	9700	0.0344	7464	3.656	2857.9	3014.3	4.284	9610	86.24%	90.96%
21 x 12E		83.2	3494.4	6552	11500	0.0360	7411	3.875	3006.8	3419.0	4.929	10990	86.05%	97.84%
22 x 12E		99.1	4162.2	6262	11600	0.0427	7175	4.684	3519.2	3430.7	5.180	11387	84.55%	82.43%

Table 3A: Predicted and Actual Performance of the S-5535-190KV Motor

		Predicted/Actual		
Propeller *(APC)*	**Voltage** *[V]*	**Shaft Speed**	**Torque**	**Shaft Power**
15 x 10E	35	1.014	0.830	0.820
16 x 12E		1.044	0.879	0.905
17 x 12E		1.053	0.775	0.807
18 x 12E		1.071	0.833	0.892
19 x 12E		1.076	0.709	0.761
20 x 12E		1.094	0.797	0.865
21 x 12E		1.104	0.746	0.815
22 x 12E		1.127	0.832	0.924
24 x 12E		1.140	0.774	0.869
14 x 10E	42	1.026	0.903	0.918
15 x 10E		1.037	0.847	0.870
16 x 12E		1.073	0.830	0.882
17 x 12E		1.076	0.740	0.791
18 x 12E		1.104	0.873	0.960
19 x 12E		1.106	0.784	0.864
20 x 12E		1.121	0.854	0.948
21 x 12E		1.131	0.786	0.879
22 x 12E		1.146	0.904	1.026

Table 3B: Predicted and Actual Performance of the S-5535-190KV Motor

2

Appendix C Calculations for Blade Sizing and Design

The purpose of this appendix is to provide the equations needed for sizing and the aerodynamic design of a propeller.

Most equations were taken, as noted, from either Volume 1 of the oft-mentioned work by Borst, Aerodynamics, Aeronautics and Flight Mechanics by Barnes W. McCormick, or NACA TR 924 by L. Criegler. Derivations and full citations are found in chapter 2 or 3 of the thesis.

C.1 Propeller Sizing

As explained in chapter 2, the propeller is "sized" using a single point performance estimate method to determine the best combination of rotational speed, number of blades and diameter. The single point method allows for quick estimates of the propeller's performance to be made by assuming that the aerodynamic and geometric properties of a single blade station (typically at 70-75% of the blade's radius) are representative of those of the entire blade. At the average blade station the aerodynamic properties (the lift and drag coefficients) are based on the lift coefficient condition selected by the user, and the geometric properties (chord length and blade angle) is based the lift coefficient and the induced velocity, *w*. The induced velocity is set through an iterative process to achieve the desired propeller performance. The iterative process uses a bisectional search that requires an initial high and low value. Two methods – the normal and maximum pitch – are available to be used for determining the initial values.

C.2 Determining the Initial Maximum and Minimum Induced Velocity

Normal Sizing Method

Minimum Induced Velocity, w_{low} (McCormick):

$$w_{low} = w_o = \sqrt{\frac{T}{2\rho A}} = \sqrt{\frac{4T}{2\rho\pi D^2}} = \sqrt{\frac{2T}{\rho\pi D^2}} \qquad \textbf{A. Eq. 97}$$

Where:

T = normal design thrust [N]

ρ = air density [kg/m^3]

A = disc area [m^2]

D = propeller diameter [m]

Maximum Induced Velocity, w_{high}:

$$\boldsymbol{w_{high} = \frac{1}{2}\left[\sqrt{V_{max}{}^2 + \frac{2T}{\rho A}} - V_{max}\right]} \qquad \textbf{A. Eq. 98}$$

Where:

V_{max} = maximum level flight speed of the aircraft [m/s]

Maximum Pitch

$$w = 2(\tan(\beta - \alpha)\, xR\omega_R - V) \qquad \textbf{A. Eq. 99}$$

2

(Based on McCormick & own derivation)

Where:

β = blade angle [radians]

α = angle of attack of the blade [radians]

p = propeller pitch [m]

x = radial blade station (percent radius) [non-dimensional]

R = propeller radius [m]

ω_R = rotational speed [radians/second]

V = forward flight speed of the aircraft [m/s]

For w_{high}, V=0, and for w_{low} V is set to the maximum level flight speed of the aircraft

C.3 Single Point Method of Estimating Thrust and Power Coefficient

At the reference blade station and for any given induced velocity:

Determine φ, $\bar{w}$, and κ

φ, the relative wind angle [radians] (Borst):

$$\phi = atan\left(\frac{V + {}^{1}/_{2}\, w}{\pi x n D}\right) \qquad \textbf{A. Eq. 100}$$

Where:

φ = relative wind angle [radian]

V = forward speed of the aircraft [m/s]

2

n = rotational speed [rev/s]

$\bar{w}$, the non-dimensional inducted velocity

$$\bar{w} = \frac{w}{V} \qquad \textbf{A. Eq. 101}$$

κ, the circulation at the blade station [non-dimensional] is an experimentally-determined property and is presented in plots as a function of:

B = number of blades

x = radial blade station (percent radius) [non-dimensional]

J_w = the advance ratio of the blade including the induced velocity, which is:

$$J_w = \frac{V + w}{nD} \qquad \textbf{A. Eq. 102}$$

1. Calculate the lift and drag coefficient

The lift and drag coefficient are obtained from the low Reynold's number correction function based on:

- the user-specified lift coefficient condition
- an assumed airfoil thickness-to-chord ratio (t/c)
- the Mach number at the station, which is calculated as (Borst):

$$M = \frac{\sqrt{(nDx\pi)^2 + V^2}}{a} \qquad \textbf{A. Eq. 103}$$

Where *a* is the speed of sound [m/s]. *a* is considered to be constant 340.3 m/s, which is the speed of sound in air at ICAO sea-level standard-day conditions

2

- the Reynold's number at the station, RN, is estimated as (based on Borst):

$$RN = c\left(\frac{\rho}{\mu}\right)aM = \left(\frac{2t_{min}}{t/c}\right)\left(\frac{\rho}{\mu}\right)aM \quad \textbf{A. Eq. 104}$$

Where

c = blade chord length [m]
ρ = air density [kg/m^3]
μ = dynamic viscosity of air [assumed constant at 1.7894 x 10^{-5} kg/ms]
t_{min} = minimum allowable cross-sectional thickness of a blade station [m]

As Reynold's number is based on the chord length of the blade, which is still unknown, the chord length is estimated to be:

$$c = \left(\frac{2t_{min}}{t/c}\right) \quad \textbf{A. Eq. 105}$$

Once the chord length is found in step 3, the lift and drag coefficient at the appropriate Reynold's number are found again.

The effect of the compressibility on the lift coefficient is considered by using the Prandtl-Gault correction when the Mach number is between 0.3 and 0.8 (McCormick)

$$C_{l\,M} = \frac{C_{l\,o}}{\sqrt{1 - M^2}} \quad \textbf{A. Eq. 106}$$

Where:

$C_{l\,M}$ = Lift coefficient, corrected for compressibility effects

$C_{l\,O}$ = Lift coefficient without considering compressibility effects

If the Mach number is greater than 0.8, M 0.8 is used. The program does not consider effects of compressibility above M 0.8 as they are unlikely to be encountered in the design of propellers for small UAVs.

2. Calculate the chord length of the blade

The product of the solidity of the blade and the lift coefficient, σC_l, is calculated as (Borst & NACA TR 924):

$$\sigma C_l = \frac{1+\bar{w}}{(1+{}^1\!/_2\,\bar{w})(1+{}^1\!/_2\,\bar{w}cos^2\phi)} 2\bar{w}\kappa \frac{sin^2\phi}{cos\phi} \qquad \textbf{A. Eq. 107}$$

Blade solidity, σ, is found by dividing σC_l by $C_{l\,M}$. c/R is determined from the solidity of the blade:

$$c/R = \frac{\sigma C_l}{C_{l\,M}} \frac{2\pi x}{B} \qquad \textbf{A. Eq. 108}$$

3. Estimate the thrust and power coefficient of the propeller:

The thrust coefficient, C_T, is (McCormick):

$$C_T = \frac{\pi^3 x}{12} \sigma C_l \left[(\lambda^2+1)^{3/2} - (\lambda^2+x_h)^{3/2}\right] \qquad \textbf{A. Eq. 109}$$

Where

$$\boldsymbol{\lambda = \frac{V}{\omega R}} \qquad \textbf{A. Eq. 110}$$

$$\boldsymbol{x_h = \frac{D_{hub}}{D_{propeller}}} \qquad \textbf{A. Eq. 111}$$

The power coefficient, C_P, is (McCormick):

$$C_P = C_T J + 1.12\frac{C_T}{2}\left[-J + \left(J^2 + \frac{\pi C_T}{8}\right)^{1/2}\right] \qquad \textbf{A. Eq. 112}$$
$$+ C_d \frac{c}{R}\frac{\pi^3 B}{64}\left[\left(\sqrt{\lambda^2+1}(\lambda^2+2) - \lambda^4 \ln\left(\sqrt{\lambda^2+1}+1\right)\right)\right.$$
$$\left. - \left(x_h\sqrt{\lambda^2+x_h}(\lambda^2+2x_h) - \lambda^4 \ln\left(\sqrt{\lambda^2+{x_h}^2}+x_h\right)\right)\right]$$

C.4 Detailed Blade Shaping Process

A complete description of the detailed blade design process is described in Chapter 2. Determining the shape of the propeller is an iterative process where the geometry of the propeller is changed until the desired thrust or power coefficient is obtained. It should be noted that, unlike with the propeller sizing process, the induced velocity may be either held constant for the entire blade (if the Betz method of propeller optimization is used) or can vary if (the calculus of variations optimization method is used). With the calculus of variation method the induced velocity each blade station is related by ζ , a non-dimensional constant, which is changed instead of the induced velocity until the desired thrust or power coefficient is obtained. The induced velocity at any blade station can be calculated from ζ using the equation:

2

A. Eq. 113

Where:

$$\gamma = tan^{-1}\left(\frac{C_D}{C_L}\right)$$ **A. Eq. 114**

$$J = \frac{V}{nD}$$ **A. Eq. 115**

For every iteration (a new of *w* or ζ), steps 1-3 from the propeller sizing section are used to determine the chord length and lift and drag coefficients at each station of the blade with each airfoil in the airfoil family. The lift coefficient is decreased until a suitable blade station (one with acceptable structural, aerodynamic and manufacturing properties) has been designed or until the program determines an acceptable blade station with that specific airfoil is impossible. Once the best airfoil for the station is determined, the elemental thrust (ΔC_T) and power coefficient (ΔC_P) are determined. From (Borst):

$$\Delta C_T = \sigma C_l \frac{2Z}{x}(\cot(\phi) - \tan(\gamma))(\Delta x)$$ **A. Eq. 116**

$$\Delta C_P = 2\pi\sigma C_l Z\left(1 + \frac{\tan(\gamma)}{\tan(\phi)}\right)(\Delta x)$$ **A. Eq. 117**

Where

$$Z = \frac{x\pi J^2}{8}\left[\frac{1 + \frac{\overline{w}}{2}(1 - \sin^2(\phi))}{\sin(\phi)}\right]^2 \sin(\phi)^2$$ **A. Eq. 118**

2

The elemental thrust and power coefficients for the strip bordering each blade station are added together to obtain the thrust and power coefficient of the entire blade.

C.5 Estimating Propeller Performance Using Both Single-Point and Full-Blade Methods

The performance of the propeller is using either method uses a process that is well described in Borst, where the induced velocity is varied until σC_L as calculated using equation 107 matches the solidity of the blade and lift coefficient based on the angle of attack, which is difference between β and ϕ. The user is referred to Borst for more details. One change from the method suggested by Borst is that the initial induced velocity was estimated from an approximate induced angle of attack, which was determined using the equation (McCormick):

$$\alpha_i = \frac{1}{2}\left\{-\left(\frac{\lambda}{x}+\frac{\sigma a V_R}{8x^2 V_T}\right)+\left[\left(\frac{\lambda}{x}+\frac{\sigma a V_R}{8x^2 V_T}\right)^2+\frac{\sigma a V_R}{2x^2 V_T}(\beta-\phi)\right]^{1/2}\right\} \qquad \textbf{A. Eq. 119}$$

2